Comprehensive Study of the Electrochemical Behavior of Polycrystalline Platinum Electrodes in Aqueous Solutions of Trifluoromethanesulfonic Acid

by

Yoshihisa Furuya

A thesis submitted to the Department of Chemistry

In conformity with the requirements for

the degree of Doctor of Philosophy

Queen's University

Kingston, Ontario, Canada

(December, 2014)

Abstract

Trifluoromethanesulfonic acid (CF_3SO_3H) is the smallest fluorinated sulfonic acid and serves as a model imitating the Nafion® ionomer of catalyst layers of polymer electrolyte membrane fuel cells (PEMFCs). The difference in the electrochemical behavior of Pt in CF_3SO_3H, as compared to H_2SO_4 or $HClO_4$, originates from the different anion nature. Because PEMFCs operate in the potential range in which electrochemical reactions involving O and H occur, the thesis focuses on: (i) Pt electro-oxidation; (ii) H electro-adsorption; and (iii) electrochemical and chemical Pt dissolution.

Platinum electro-oxidation in 0.1 M CF_3SO_3H is studied at various polarization potentials (E_p), polarization times (t_p) and temperatures (T). The reaction mechanism is revised and expanded by taking into account possible interactions of cations, anions and water molecules with Pt. A modified kinetic equation for the interfacial place exchange is proposed. The application of the interfacial place exchange and the metal cation escape mechanisms results in the determination of the $Pt^{\delta+}$–$O^{\delta-}$ surface dipole moment (μ_{PtO}), as well as the potential drop (V_{ox}) and electric field (E_{ox}) within the oxide. The platinum-anion interactions indirectly affect the surface electro-oxidation kinetics.

The under-potential deposition of H (UPD H) on Pt in CF_3SO_3H is investigated over a broad T range using cyclic voltammetry. The general electrochemical adsorption isotherm is used to determine standard Gibbs energy ($\Delta_{ec-ads}G°(H_{UPD})$), entropy ($\Delta_{ec-ads}S°(H_{UPD})$), and enthalpy ($\Delta_{ec-ads}H°(H_{UPD})$) of electro-adsorption, and energy of the Pt–H_{UPD} surface bond ($E_{Pt-H_{UPD}}$). The lateral interactions between H_{UPD} adatoms are repulsive.

Platinum electro-dissolution in 0.1 and 0.5 M CF_3SO_3H, H_2SO_4, and $HClO_4$ solutions is studied using potential cycling and inductively coupled plasma mass spectrometry. The results demonstrate that the anion nature has no or negligible impact on Pt electro-dissolution; however, pH significantly affects the process and the higher the pH value the greater the electro-dissolution of Pt. An analysis of potential versus pH diagrams (Pourbaix diagrams) for acid solutions of different concentrations demonstrates that

dissolved Pt (present as Pt^{2+} and Pt^{4+}) can form through anodic dissolution of metallic Pt, as well as through anodic electrochemical and chemical dissolution of PtO.

Co-Authorship

All work reported in this thesis was carried out by the author under the supervision of Professor Gregory Jerkiewicz in the Department of Chemistry at Queen's University. Some of the research objectives were determined jointly by Professor Jerkiewicz and the Electric Vehicle System Laboratory of Nissan Motor Company. Portions of this thesis contain experimental work that was carried out in collaboration with the group of Professor Diane Beauchemin in the Department of Chemistry at Queen's University. Portions of this thesis are submitted as manuscripts for publication in peer-reviewed scientific journals:

1. Yoshihisa Furuya, Tetsuya Mashio, Atsushi Ohma, Nilesh Dale, Kenzo Oshihara, Gregory Jerkiewicz, "Surface Oxide Growth on Platinum Electrode in Aqueous Trifluoromethanesulfonic Acid", on-line *Journal of Chemical Physics* (2014)

2. Yoshihisa Furuya, Tetsuya Mashio, Atsushi Ohma, Gregory Jerkiewicz, "Thermodynamics of the Under-Potential Deposition of Hydrogen on Polycrystalline Platinum in Aqueous Trifluoromethanesulfonic Acid Solution", on-line *Electrocatalysis* (2014)

3. Yoshihisa Furuya, Tetsuya Mashio, Atsushi Ohma, Min Tian, Farhad Kaveh, Diane Beauchemin, Gregory Jerkiewicz, "Influence of Electrolyte on Platinum Electro-dissolution in Acidic Media", submitted to *ACS Catalysis* (2014)

Acknowledgements

I would like to express my sincere gratitude towards my supervisor, Prof. Gregory Jerkiewicz, for all his support, patience and guidance over the course of my graduate studies. I would also like to express my appreciation to Prof. Diane Beauchemin for all of the valuable support and advice through the long-term collaboration. I would like to thank my committee member, Prof. Nick Mosey, for his advice and suggestions.

I would like to thank the laboratory members at Queen's University, past and present, for their friendship and enthusiastic discussion: Dr. Liyan Xing, Dr. M. Akhtar Hossain, Dr. Min Tian, Dr. Julia van Drunen, Dr. Koichi Matsuzawa, Mr. Jutae Kim, Mr. Nakkiran Arulmozhi, Ms. Sadaf Tahmasebi, Ms. Ashley McMath, Mr. Derek Esau, and Mr. Farhad Kaveh.

I would also like to thank my colleagues at Nissan Motor Company for their support and stimulating discussions on various aspects of automotive fuel cell research and development: Dr. Atsushi Ohma, Dr. Kev Adjemian, Dr. Kenzo Oshihara, Dr. Nilesh Dale, and Mr. Tetsuya Mashio. I also would like to acknowledge the financial support towards this PhD project and my stay in Kingston, Canada, from Nissan Motor Company.

Most importantly, I would like to thank my family for their support, love, and patience through my research project.

Statement of Originality

This work presents the first comprehensive electrochemical study of polycrystalline Pt electrodes in aqueous trifluoromethanesulfonic acid (CF_3SO_3H, abbreviated as TFMSA) solutions, which serves as a suitable molecular model mimicking the Nafion® ionomer: electro-oxidation, under-potential deposition of hydrogen, and electrochemical and chemical dissolution. The results reveal new findings and create new knowledge on the behavior of platinum electrodes in aqueous CF_3SO_3H solutions. These new results will contribute to the improvement of durability and lifetime of Pt-containing catalyst layers of polymer electrolyte membrane fuel cells.

Yoshihisa Furuya

August, 2014

Table of Contents

List of Figures

List of Tables

List of Abbreviations

A_{ecsa}: electrochemically active surface area

A_{geom}: geometric surface area

A_r: real sutface area

AFC: alkaline fuel cell

a': distance between the metal cation and the top of the activation energy barrier

$a_{H_3O^+}$: activity of H_3O^+

a_{H^+} : activity of proton

$a_{Pt^{2+}}$: activity of Pt^{2+}

$a_{Pt^{4+}}$: activity of Pt^{4+}

*C*dl: double layer capacitance

CE: counter electrode

CL: catalyst layer

CV: cyclic voltammetry

c: electrolyte concentration

D_{H_2} : dissociation energy of $H_2(g)$

D_{Pt}: diameter of Pt atom

d_L: oxide limiting thickness regarding Mott-Cabrera mechanism

d_{ox}: thickness of surface oxide

E: potential

E_L: lower potential limit

E_{ox}: electric field across oxide

E_p: polarization potential

$E_{\text{pl-exch}}$: onset potential of interfacial place exchange

$E_{\text{Pt/PtO}}$: onset potential of PtO formation on Pt surface

$E_{\text{PtO/PtO2}}$: onset potential of PtO_2 formation on the surface of PtO

$E_{\text{Pt}-\text{H}_{\text{UPD}}}$: Pt–H_{UPD} surface bond energy

E_{pzc}: potential of zero charge

E_{RHE}: electrode potential measured versus the reversible hydrogen electrode

E_{SHE}: electrode potential measured versus the standard hydrogen electrode

E_{U}: upper potential limit

F: faraday's constant

f_{H_2} : fugacity of H_2(g)

FCEV: fuel cell electric vehicle

GDL: gas diffusion layer

GHG: greenhouse gas

H_{chem}: chemsorbed hydrogen atom

H_{i}: enthalpy of solution of the cation in the oxide

H_{UPD}: under-potential deposited hydrogen

HER: hydrogen evolution reaction

HOR: hydrogen oxidation reaction

H_2O_{phys}: physisorbed water molecule

$I_{\text{M-C}}$: intercept of Equation 2.18

$I_{\text{pl-exch}}$: intercept of Equation 2.11

ICP-MS: inductively coupled plasma mass spectrometry

IEC-ICP-MS: ion-exchange chromatography coupled to inductively coupled plasma mass spectrometry

j: current density

k: rete constant

k_B: Boltzmann constant

LPG: liquefied petroleum gas

MCFC: molten carbonate fuel cell

MEA: membrane electrode assembly

ML: monolayer

m_{ox}: oxide mass

m_{Pt}: amount of electro-dissolved Pt

N: surface density of atoms

N_A: Avogadro number

n: potential cycle number

n_{ox}: number of oxide monolayer

O_{chem}: chemisorbed oxygen

OER: oxygen evolution reaction

ORR: oxygen reduction reaction

PAFC: phosphoric acid fuel cell

PEMFC: proton exchange membrane fuel cell

PTFE: polytetrafluoroethylene

Pt-NPs: Pt nanoparticles

Pt(poly): polycrystalline platinum

Pt_{surf}: Pt surface atom

$(Pt^{2+}–O^{2–})_{quasi\text{-}3D}$: place-exchanged PtO

p_{H2}: partial pressure of hydrogen

Q: charge

Q_{ox}: oxide charge

$Q_{UPD\ H}$: charge associated with UPD H

q: charge density

q_{Pt}: Pt surface charge

$q_{crit,\ 1}$: critical oxide charge density converted from X_1

q_{ox}: charge density of oxide

$q_{ox,1}$: charge density of un-exchanged PtO

$q_{ox,2}$: charge density of place-exchanged PtO

$q_{ox,\ form}$: charge density of oxide formation

$q_{ox,\ form}$: charge density of oxide reduction

$q_{1\text{ML H}_{UPD}}$: charge density required to form a monolayer of H_{UPD}

R: ideal gas constant

R': roughness factor

RE: reference electrode

RHE reversible hydrogen electrode

S_{chem}: chemisorbed sulfur

$S_{M\text{-}C}$: slope of Equation 2.18

$S_{pl\text{-}exch}$: slope of Equation 2.11

SHE: standard hydrogen electrode

SOFC: solid oxide fuel cell

s: scan rate

T: temperature

TFMSA: Trifluoromethanesulfonic acid

t_p: polarization time

U: activation energy barrier for the metal cation diffusion in the oxide

UPD H: under-potential deposition of hydrogen

V_{ox}: potential drop across oxide

$V_{p(d\text{-}d)}$: potential energy of two identical and parallel dipoles

WE: working electrode

X_0: critical thickness defined as Equation 2.3

X_1: critical thickness defined as Equation 2.4

ZEV: zero emission vehicle

β: symmetry factor

$\gamma_{\pm}$: mean activity coefficient

$\Delta_{ec-ads}G°(H_{UPD})$: standard Gibbs energy of elector-adsorption

$\Delta_{ec-ads}H°(H_{UPD})$: standard enthalpy of elector-adsorption

$\Delta_{ec-ads}S°(H_{UPD})$: standard entropy of elector-adsorption

$\Delta\phi$: surface potential prior to the formation of O-containing surface species

$\Delta\chi_t$: $\chi_o - \chi_t$ is the time-dependent surface potential due to the co-existence of the $Pt^{\delta+}$–$O^{\delta-}$ surface dipole and the place-exchanged Pt^{2+}–O^{2-} quasi-3D lattice

ε_o:vacuum dielectric constant

ε_r:relative dielectric constant

$\theta_{H_{UPD}}$: surface coverage of H_{UPD} on the Pt surface

θo: chemisorbed oxygen coverage

μ_{PtO}: dipole moment of surface PtO

μ_{oxide}: dipole moment of oxide

ν: vibration frequency of the surface

ρ: resistivity

χ_o: surface potential due to development of $Pt^{\delta+}$–$O^{\delta-}$ dipole

χ_t: time-dependent surface potential due to the place-exchanged Pt^{2+}–O^{2-}

Ω: volume of oxide per metal atom

$\omega_{H_{UPD}}$: energy of later interactions of H_{UPD}

Chapter 1

Introduction

1.1 General introduction: demand of hydrogen technology

Over the past several decades, global warming has taken place due to the emission of greenhouse gasses (GHG, e.g. carbon dioxide (CO_2), methane, nitrogen oxides and fluorinated gases), which causes severe irreversible climate changes and might bring unprecedented natural disasters (e.g. flooding, heat waves) in the world [1]. CO_2 is one of the major sources of emissions of GHG due to the combustion of fossil fuels and its emissions account for 76% of total GHG emissions (Figure 1.1).

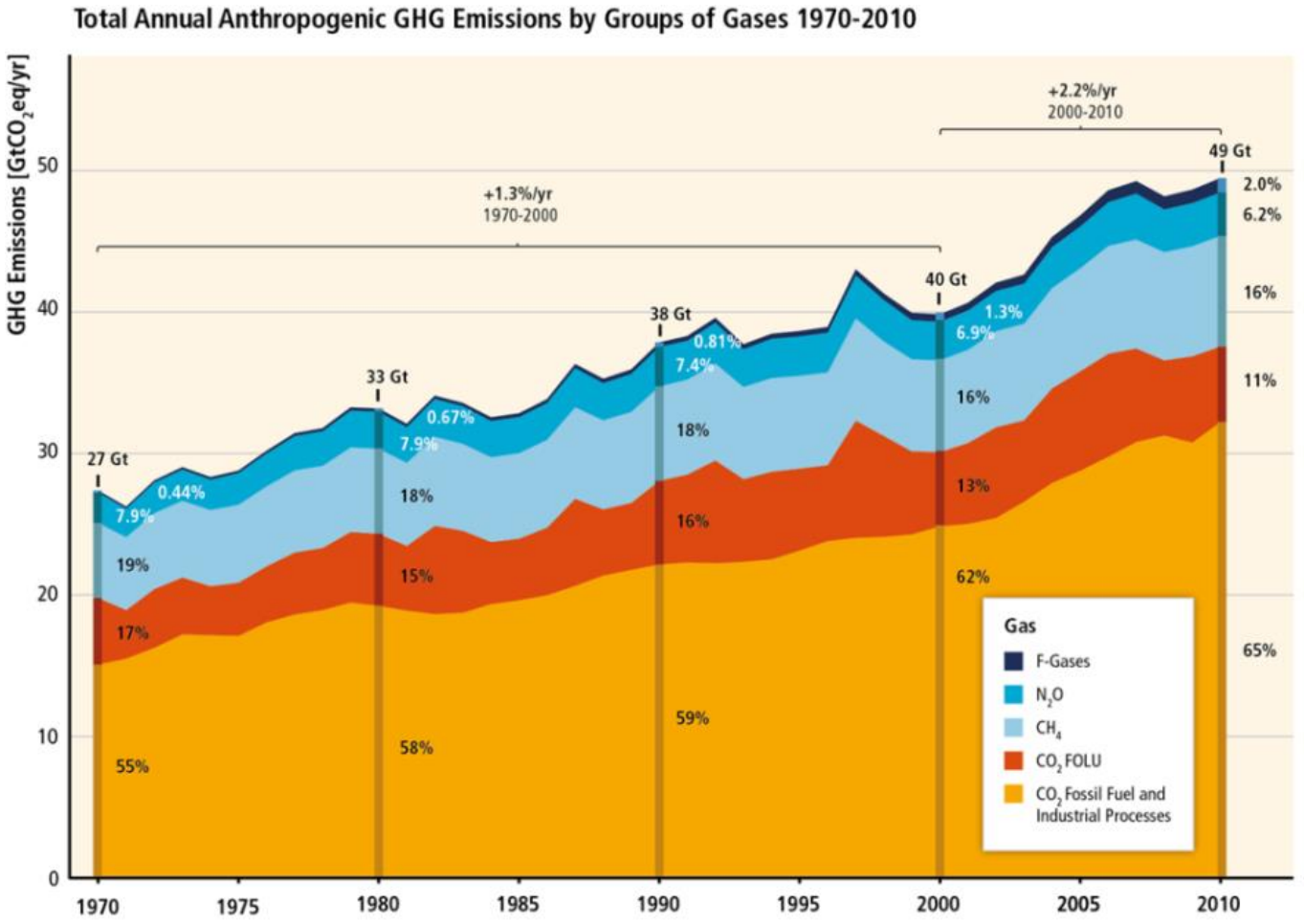

Figure 1.1. Annual anthropogenic GHG emissions by groups of gases 1970-2010 [1].

As the global population and world economy steadily increase, the emission level of CO_2 will continue to rise as well. In addition, without explicit additional efforts to reduce CO_2 emissions, CO_2 concentration levels will rise to between 750 and more than 1300 ppm by 2100, resulting in a global mean surface temperature increase of 3.7 °C to 4.8 °C compared to pre-industrial levels [1,2]. Therefore, in order to mitigate global warming, it is critical to reduce fossil fuel consumption.

Figure 1.2 presents direct and indirect GHG emission shares (in % of total anthropogenic GHG emissions) in each economic sector in 2010 [1]. GHGs are primarily emitted in the energy supply (production of electricity and heat), industry, and transportation sectors. Although fossil fuels (coal, natural gas, and petroleum) have been the most cost-effective energy source, it is necessary to take appropriate measures in each sector to decrease these emissions.

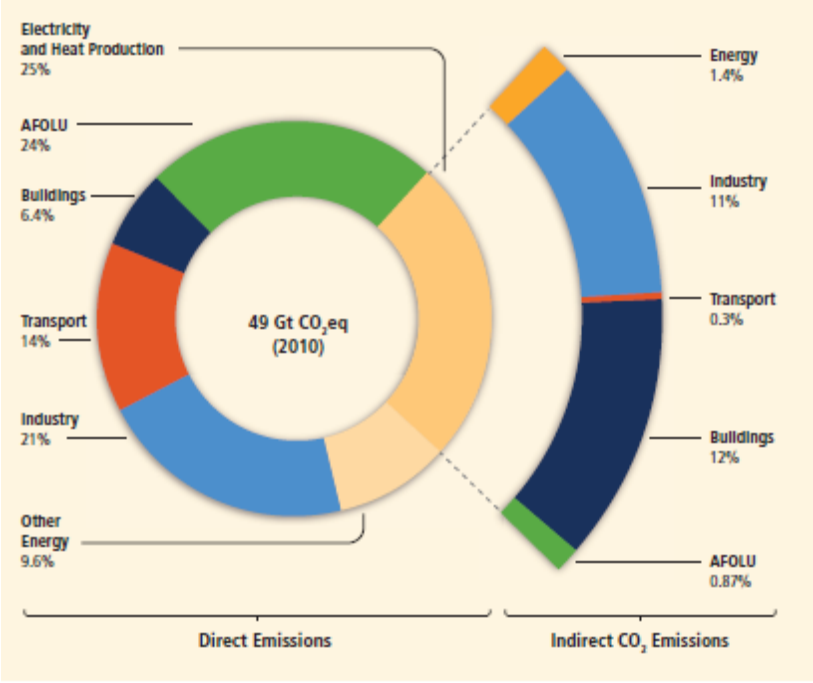

Figure 1.2. Direct and indirect GHG emission shares (in % of total anthropogenic GHG emissions) of economic sectors in 2010 [1].

The approach of multiple-energy sources is one of the measures to help solve the problem. Figure 1.3 demonstrates an example of the employment of multiple primary energy sources into the transport sector, regarding a possible transport pathway from primary energy sources to powertrains of automotive vehicles [3]. The energy sources are classified into three categories: fossil fuels (coal, crude oil and natural gas), renewable energies (biomass, wind, hydro, geothermal), and nuclear energy. The primary energy sources are transformed into diverse energy carriers (e.g. gasoline, liquefied petroleum gas (LPG), electricity and hydrogen), distributed through suitable infrastructure, and finally used in powertrains for automotive vehicles. Renewable energy and nuclear power can provide electric power with low GHG emissions. However, some problems and limitations still remain: nuclear energy generates radioactive byproducts and is prone to rare but catastrophic accidents (e.g. crisis at Fukushima Dai-Ichi plant after devastating earthquake in Japan; the meltdown of the Chernobyl plant in former Soviet Union); renewable energy is cost-ineffective due to the low-energy density.

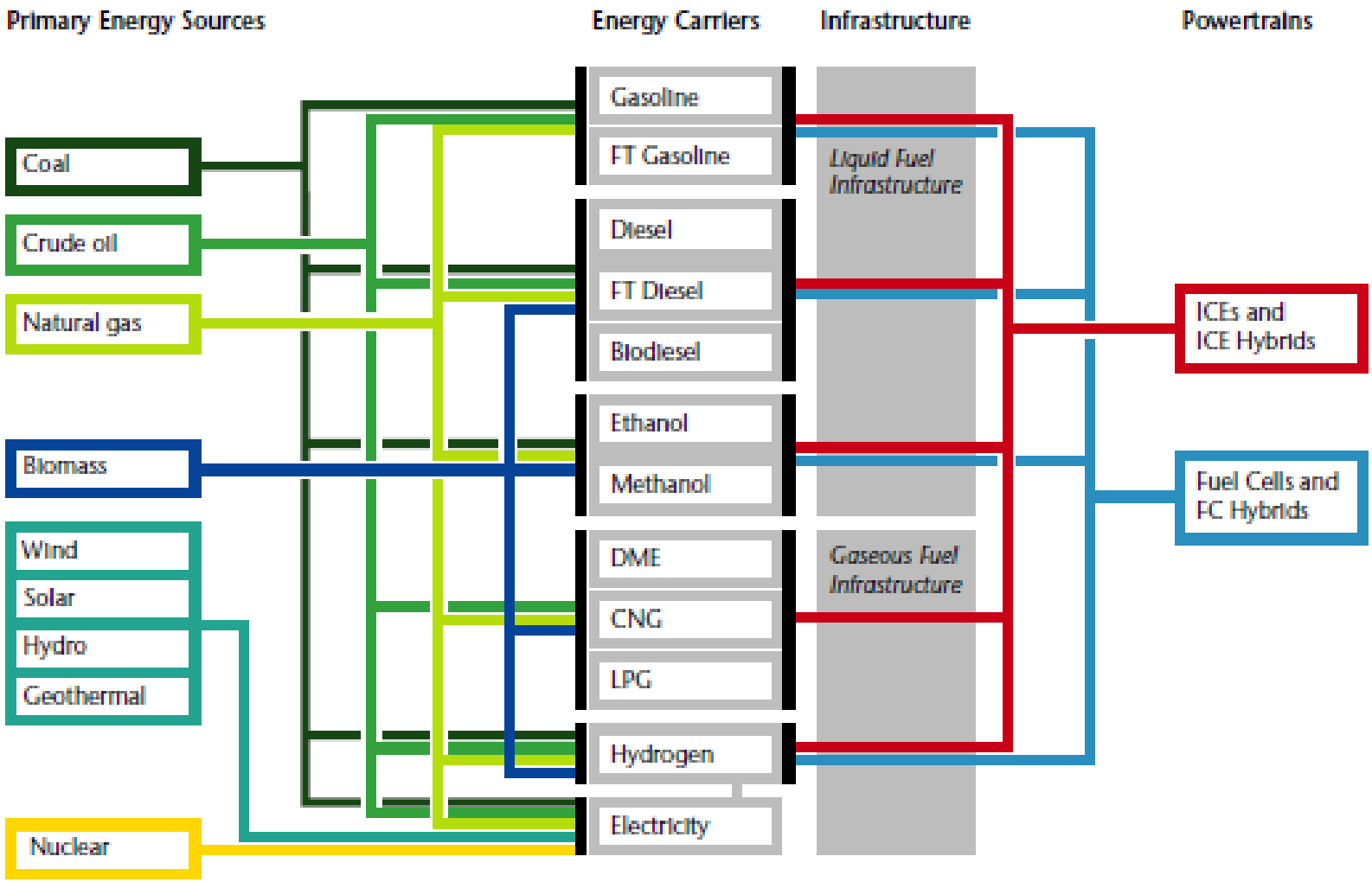

Figure 1.3. Possible transport fuel pathways from primary energy sources to powertrains [3]

It should be noted that the strategy of using multiple energy sources contributes not only to the reduction of GHG emissions, but also improves air quality, resource productivity, and energy security. Although the impact of multiple energy sources on the cost of achieving many of the aforementioned objectives is not well understood, it is essential, however, for countries to take on the policy of using multiple-energy sources to achieve economic growth and reduce the effects of global warming [1].

Hydrogen is one of the more promising energy carriers for the next generation mobility and sustainable development, because it can be produced by diverse methods, such as water electrolysis using electric power, steam-reforming of natural gases, or coal gasification. Water electrolysis using renewable energy is the best process for reduction of CO_2 emission. Fuel cells can convert the hydrogen into electric power using electrochemical reactions without combustion: no pollutants are formed during the operation. The use of hydrogen and fuel cells provide a wide range of benefits, as described by the U.S. Department of Energy [4]: (i) reducing GHG emissions; (ii) reducing oil consumption; (iii) advancing renewable power using hydrogen for energy storage; (iv) fuel flexibility using domestic and diverse fuel; (v) high efficiency energy conversion; (vi) reducing air pollution; (vii) high reliability and grid support capability; (viii) sustainability for diverse applications; (ix) quiet operation; (x) low maintenance needs; and (xi) opportunities for economic growth and leadership in an emerging high-technology sector. Figure 1.4 presents a well-to-wheels analysis of GHG emissions for vehicles with various fuel and propulsion systems [4]. The well-to-wheel analysis of GHG emissions accounts for all the emissions that are produced by processing the oil or gas to the fuel that is consumed by the automotive vehicles in various ways. Fuel cell electric vehicles (FCEVs) using hydrogen from renewable energy sources produce one of the lowest quantities of GHG among conventional and alternative vehicles and fuel pathways. Even in the case of FCEVs using hydrogen, which is

produced from natural gas, GHG emissions will be ca. 40% less than those from advanced internal combustion engine vehicles. In addition, it will be 15% less than those from advanced hybrid electric vehicles, and ca. 25% less than those from gasoline-powered plug-in hybrids [4]. Thus, the hydrogen fuel cell is one of the ideal measures for sustainable development. It should be noted that battery electric vehicle using renewable energy shows lowest quantities of GHG (zero). However, battery vehicle has technical problem: short cruising range and long charging time. Thus, use of battery vehicle is limited to smaller car such as city commuter. Thus, it is necessary to develop multiple powertrains for next generation vehicles.

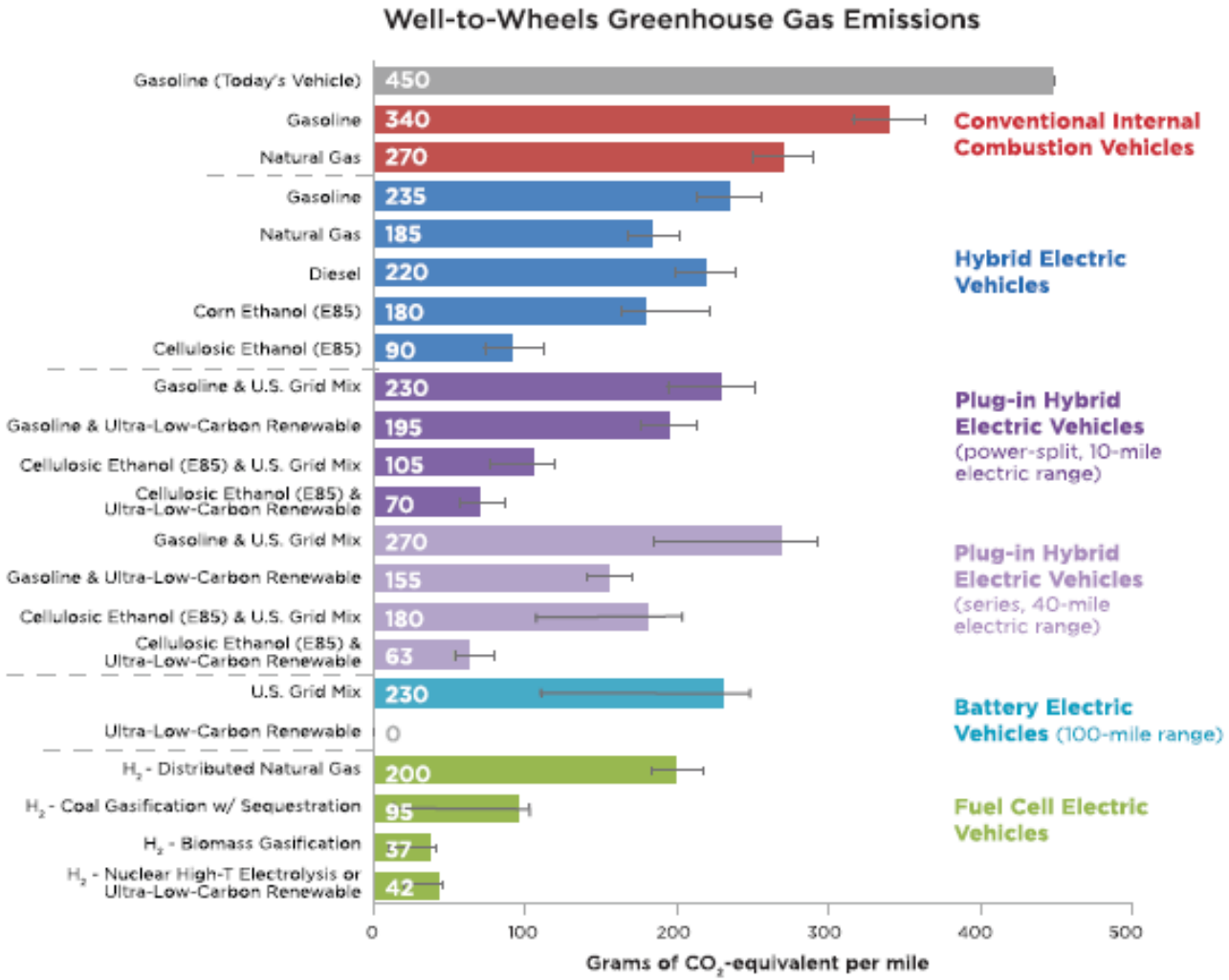

Figure 1.4. Well to wheels analysis of GHG emissions for various fuel and propulsion system combinations [4]

Because hydrogen as an energy carrier poses a wide range of advantages, it is necessary now to introduce 'hydrogen technology' into the human society for sustainable development. Various issues still remain and need to be overcome: (i) technology of hydrogen production (e.g. electrolysis from renewable electric power); (ii) infrastructure of hydrogen transportation (e.g. pipeline); (iii) technology of hydrogen storage (e.g. high-pressured tank, storage material); and (iv) technology of utilization of hydrogen (e.g. fuel cell), just to mention a few. The fuel cell is one key technology, which is regarded in the subject of electrochemistry as a middle and long term sustainable development option.

1.2 Proton Exchange Membrane Fuel Cell

A fuel cell is a device that can convert chemical energy from fuel to electric energy through an electrochemical reaction without high-temperature combustion. Five major types of fuel cells can be identified by the type of electrolyte: alkaline fuel cells (AFCs), proton-exchange membrane fuel cells (PEMFCs), solid oxide fuel cells (SOFCs), phosphoric acid fuel cells (PACFs), and molten carbonate fuel cells (MCFCs). They are further classified on the basis of operating temperature. The low operating temperature is in the range of 50–250 °C for PEMFCs, AFCs and PAFCs; high operating temperature in the range of 650–1000 °C like MCFCs and SOFCs [5]. Table.1.1 presents a comparison of different types of fuel cells. The AFC (using aqueous potassium hydroxide (KOH (aq)) as electrolyte) was the first type of fuel cell to be put into practical service in the 1960s and 1970s for use in space exploration. However, the alkaline electrolyte is sensitive to impurities in the air or in fuels (e.g. CO_2, CO); it needs a separate system to remove the CO_2 from the air; and the system is large and expensive. Thus, it is not well

suited for commercial applications. MCFCs and SOFCs can operate at higher temperatures with higher efficiency, namely 50–60%. A separate reformer is not required to extract hydrogen from the fuels, due to its internal reforming capability. Precious metals are also not required due to the high catalytic activity at high operating temperatures. However, the MCFCs and SOFCs are not suitable for larger fluctuations in load demand (such as, automotive vehicles); thus, they are mainly used for medium and large power applications. PEMFCs are recognized as being the most important alternative to the internal combustion engine. PEMFCs generate electric power without producing CO_2(g) or other air pollutants, which affect the environment and human health. As PEMFCs can operate at low temperatures (T < 80 °C) with higher power density, the characteristic of PEMFCs can satisfy well-packed application for the automotive requirement.

Table 1.2-1. Comparison of different types of fuel cells [6]

Parameters	Fuel cell types					
	PEMFC	AFC	PAFC	MCFC	SOFC	DMFC
Electrolyte	Solid polymer membrane (Nafion)	Liquid solution of KOH	Phosphoric acid (H_3PO_4)	Lithium and potassium carbonate (LiAlO2)	Stabilized solid oxide electrolyte (Y_2O_3, ZrO_2)	Solid polymer membrane
Operating temperature (°C)	50–100	50–200	~200	~650	800–1000	60–200
Anode reaction	$H_2 \rightarrow 2H^+ + 2e^-$	$H_2 + 2(OH^-) \rightarrow 2H_2O + 2e^-$	$H_2 \rightarrow 2H^+ + 2e^-$	$H_2O + CO_3^{2-} \rightarrow H_2O + CO_2 + 2e^-$	$H_2 + O^{2} \rightarrow H_2O + 2e^-$	$CH_3OH + H_2O \rightarrow CO_2 + 6H^+ + 6H^-$
Cathode reaction	$1/2O_2 + 2H^+ + 2e^- \rightarrow H_2O$	$1/2O_2 + H_2O + 2e^- \rightarrow 2(OH)^-$	$1/2O_2 + 2H^+ + 2e^- \rightarrow H_2O$	$1/2O_2 + CO_2 + 2e^- \rightarrow CO_3^{2-}$	$1/2O_2 + 2e^- \rightarrow O^{2-}$	$3O_2 + 12H^+ + 12H^- \rightarrow 6H_2O$
Charge carrier	H^+	OH^-	H^+	$CO_3^{=}$	$O^{=}$	H^+
Fuel	Pure H_2	Pure H_2	Pure H_2	H_2, CO, CH_4, other hydrocarbons	H_2, CO, CH_4, other hydrocarbons	CH_3OH
Oxidant	O_2 in air	O_2 in air	O_2 in air	O_2 in air	O_2 in air	O_2 in air
Efficiency	40–50%	~50%	40%	>50%	>50%	40%
Cogeneration	–	–	Yes	Yes	Yes	No
Reformer is required	Yes	Yes	Yes	–	–	–
Cell Voltage	1.1	1.0	1.1	0.7–1.0	0.8–1.0	0.2–0.4
Power density (kW/m^3)	3.8–6.5	~1	0.8–1.9	1.5–2.6	0.1–1.5	~0.6
Installation Cost (US $/kW)	<1500	~1800	2100	~2000–3000	3000	–
Capacity	30 W, 1 kW, 2 kW, 5 kW, 7 kW, 250 kW	10–100 kW	100 kW, 200 kW, 1.3 MW	155 kW, 200 kW, 250 kW 1 MW, 2 MW	1 kW, 25 kW, 5 kW, 100 kW, 250 kW, 1.7 MW	1 W to 1 kW, 100 kW to 1 MW (Research)
Applications	Residential; UPS; emergency services such as hospitals and banking; industry; transportation; commercial	Transportation; space shuttles; portable power	Transportation; commercial cogeneration; portable power	Transportations (e.g. marine-ships; naval vessels; rail); industries; utility power plants	Residential; utility power plants; commercial cogeneration; portable power.	It is used to replace batteries in mobiles; computers and other portable devices
Advantages	High power density; quick start up; solid non-corrosive electrolyte	High power density; quick start up	Produce high grade waste heat; stable electrolyte characteristics	High efficiency; no metal catalysts needed	Solid electrolyte; high efficiency; generate high grade waste heat	Reduced cost due to absence of fuel reformer
Drawbacks	Expensive platinum catalyst; sensitive to fuel impurities (CO, H_2S)	Expensive platinum catalyst; sensitive to fuel impurities (CO, CO_2, CH_4, H_2S)	Corrosive liquid electrolyte; sensitive to fuel impurities (CO, H_2S)	High cost; corrosive liquid electrolyte; slow start up; intolerance to sulfur	High cost; slow start up; intolerance to sulfur	Lower efficiency and power density

Figure 1.5 presents the structure of PEMFC [7]. As mentioned above, the PEMFCs convert the chemical energy of fuel (cf. hydrogen is the most promising fuel for the automotive application) to electric energy by electrochemical reactions. Hydrogen gas is supplied to the anode where the hydrogen oxidation reaction (HOR) takes place; it produces protons and electrons.

$$H_2 \longrightarrow 2H^+ + 2e^- \tag{1.1}$$

The protons are transferred to the cathode through the electrolyte. Oxygen gas is supplied to the cathode, where the oxygen reduction reaction (ORR) takes place and produces water.

$$O_2 + 4e^- + 4H^+ \longrightarrow 2H_2O \tag{1.2}$$

The electrons are transferred through an electrical circuit and generate electric power for desired applications. The overall reaction of the fuel cell is as follows:

$$2H_2 + O_2 \longrightarrow 2H_2O \tag{1.3}$$

Water is the only product when pure hydrogen is used as a fuel in the system.

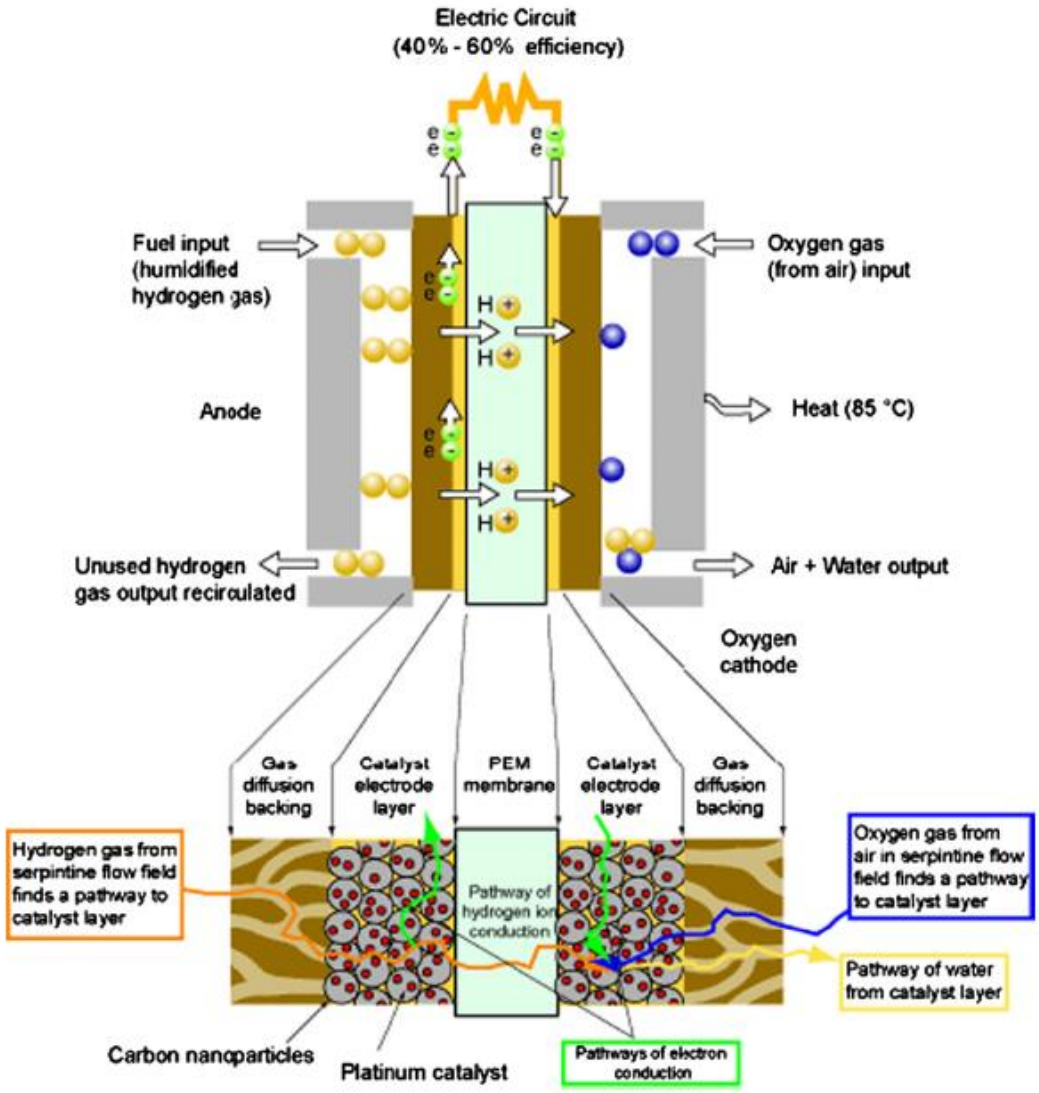

Figure 1.5. Structure of PEMFCs [7]

A PEMFC is composed of: a polymer electrolyte membrane acting as a proton conductor, catalyst layers (CLs) as electrodes (anode, cathode) for ORR and HOR, and gas diffusion layers (GDL) for gas supply as shown in Figure 1.5. The five-layer components are assembled and used as a membrane electrode assembly (MEA). The polymer electrolyte membrane has to possess the following characteristics: high chemical and mechanical durability, high gas migration blockage, and high proton conductivity irrespective of the relative humidity. The CLs need to perform many functions to achieve the desired activity towards the ORR and HOR: effective transport of reactive gases (O_2, H_2, water) and electrons, and high intrinsic activity of the metallic catalysts. Thus, catalyst layers consist of the following complex components to satisfy these requirements: (i) porous carbon support with large surface area for high transport of products and reactants, high electronic conductivity; (ii) highly dispersed platinum (Pt) nanoparticles on carbon support for increased active surface area for HOR and ORR; and (iii) ionomer as electrolyte for maintaining proton conduction in the vicinity of Pt surface. GDL functions not only as a gas transport medium but also protects both catalyst layers and membrane; typically, a mixture of both carbon fiber and polytetrafluoroethylene (PTFE) is used.

1.3 Challenge of Commercialization of FCEVs

Although there have been many intense efforts involved in the commercialization of FCEVs over the past ten years, further cost reduction and improvement of their durability, performance and sub-zero start-up are key issues that need to be addressed in order to achieve their mass production and affordability. Figure 1.6 presents the current state of FCEVs (e.g. performance, durability and cost) for commercialization compared with their target in 2013 [8]. In practice, durability and cost are the primary challenges of fuel cell commercialization and must be met concurrently.

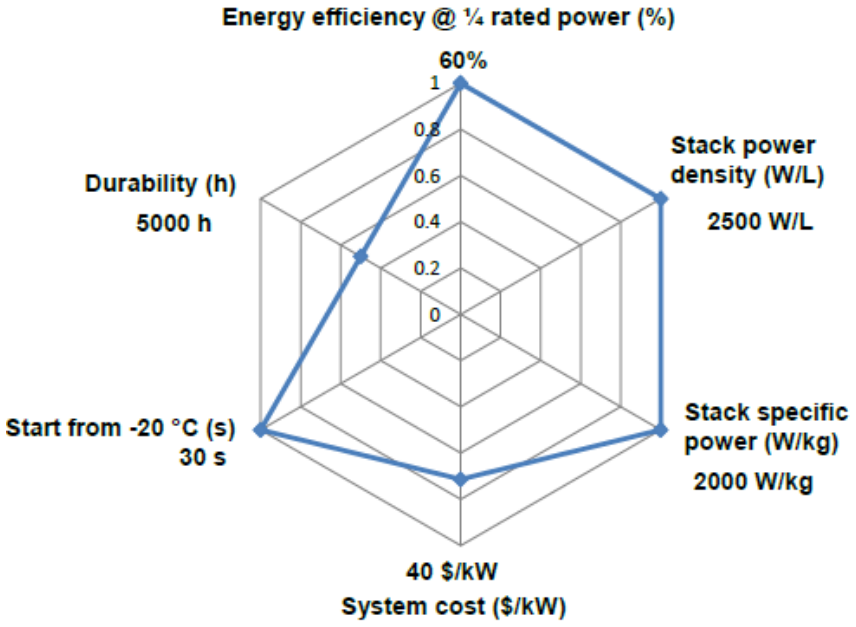

Figure 1.6. Current situation of FCEVs commercialization compared with their target in 2013 **[**8**]**

1.3.1 Cost reduction

Cost reduction of FCEVs is one of the most crucial issues for commercialization. Figure 1.7 presents FCEVs system cost breakdown for 80 kW automotive vehicles [9]. The fuel cell stack cost accounts for about 50% of all FCEVs system cost. Thus, the fuel cell stack is well-accepted to be the most important component for the cost reduction. The target cost of fuel cell system with a projected high production volume (500,000 units) is at $40/kW by 2020, while the ultimate cost target is at $30/kW (cf. cost of transportation fuel cell systems is $55/kW in 2013) according to the U.S. Department of Energy [8].

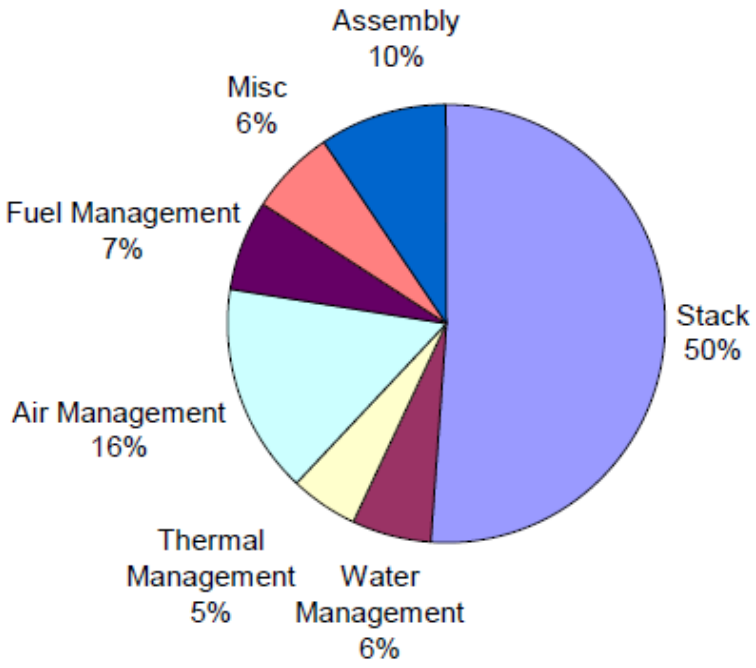

Figure 1.7 PEMFCs system cost break down for 80 kW automotive vehicles [10]

Figure 1.8 presents the breakdown of fuel cell stack cost under high production volume conditions (please, notice that Figure 1.7 refers to the entire cost of fuel cell system). Among fuel cell stack components, the catalyst layers (CLs) account for a large portion of the total cost of the fuel cell stack ('catalyst and its application' in Figure 1.8), because they contain precious Pt nanoparticles as the metallic electrocatalysts. If the mass production of FCEVs commences, material cost of Pt may increase rather than decrease due to its limited supplies and increased demand. Thus, in order to commercialize FCEVs, it is of great importance to reduce the Pt usage in fuel cells without sacrificing the performance and durability.

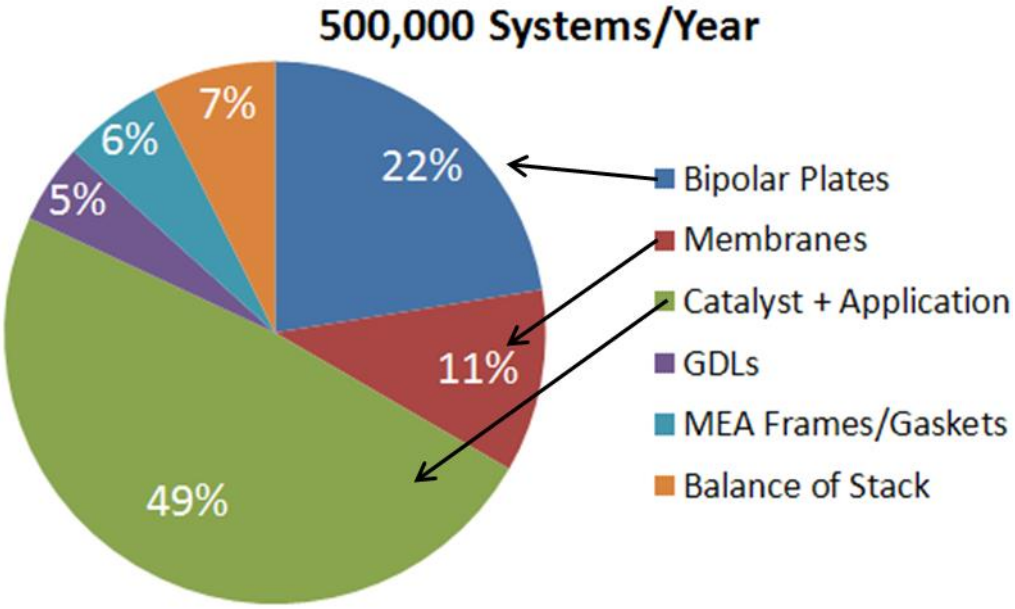

Figure 1.8. Cost break down of fuel cell stack cost in 2013 (500,000 systems per year) [8].

1.3.2 Durability

The durability of MEAs is one of the most important issues that need to be resolved in order to achieve reduction of Pt usage in PEMFCs. The degradation of MEAs using actual FCEVs has been investigated recently [10]. There are three main operational modes for the FCEVs degradation (Table 1.2): (a) start-up; (b) load cycling (repetitive accelerating, and decelerating); and (c) idling.

Table 1.2-2. Fuel cell operating modes and major types of degradation [10]

Operating mode	Degradation	Main causes
Start-up	Cathode catalyst surface area loss Cathodic reactant gas diffusion deterioration	Cathode carbon support corrosion by high potential
Load cycling	Cathode catalyst surface area loss	Cathode catalyst dissolution by potential cycling
Idling (low current)	Cathode catalyst surface area loss Membrane proton conductivity loss	Cathode catalyst dissolution by high potential Chemical decomposition by peroxide (radical) attack Cathode catalyst poisoning by membrane fragments

(a) Start-up

The start-up mode stands for the starting of FCEVs. When the FCEVs start, hydrogen is fed to the anode and replaces air atmosphere. Meanwhile, the potential of the cathode increases because electromotive force is produced [10]. The maximum potential reaches ca. 1.5 V vs the reversible hydrogen electrode (RHE) [11]. As a result of the high potential, carbon corrosion takes place and catalyst layers collapse according to the following electrochemical equation:

$$C + 2H_2O \longrightarrow CO_2 + 4H^+ + 4e^- \qquad (1.4)$$

Simultaneously, Pt particles on the carbon support aggregate or are detached from it; the aggregation and detachment lead to a decline in PEMFC performance.

(b) Load cycling

Load cycling refers to repetitive accelerating and decelerating while driving. The potential at the cathode decreases with acceleration of FCEVs and increases with the deceleration; the potential ranges from 0.6 V to 1.0 V vs RHE [12]. It should be noted that the potential decreases when current is generated, as expected on the basis of Butler-Volmer equation. As a result of the change in potential, Pt is proposed to dissolve electrochemically into the electrolyte in an ionic state until Pt surface oxide formation is completed; Pt oxide simultaneously forms and can either act as a passive layer or itself can undergo dissolution. Although different electrochemical and chemical mechanisms of Pt dissolution have been proposed by many researchers and they are not widely accepted yet because it is a very new area of research [13], a representative reaction of Pt dissolution can be expressed as follows:

$$Pt \longrightarrow Pt^{2+} + 2e^{-} \tag{1.5}$$

The electro-dissolved Pt ion can re-deposit onto Pt particles and makes the particles larger; the process reduces the surface area per unit of Pt mass. As the decrease of the Pt surface area takes place, it leads to deterioration of the performance of FCEVs [13].

(c) Idling

Idling initiates the standby mode of FCEVs. Since small current is flown at idling conditions, the potential of cathode is higher during the standby of FCEVs than during the load cycling. The exact potential during the idling depends on the system, but it can be assumed that the potential at idling is ca. 1.0 V vs RHE, which corresponds to the maximum potential of the load cycling mode [12].

During idling, two types of degradation processes take place: (i) Pt dissolution and (ii) decomposition of the membrane. The former is caused by high potential conditions based on Equation 1.5. The latter is caused by the generation of hydrogen peroxides under harsh conditions of low relative humidity (RH) and high temperature. However, the membrane degradation can be neglected since FCEVs are not operated constantly at high temperatures [10].

Figure 1.9 shows the contributions of each operating mode to the entire degradation of MEAs during real driving of FCEVs [10]. Among these degradation modes, the degradation by the start-up mode accounts for 44% of the entire degradation. The load cycling and the idling have approximately the same contributions. This is because the cumulative time of the load cycling is longer than the idling time, whereas the degradation per unit of time of the load cycling is greater than that of the idling.

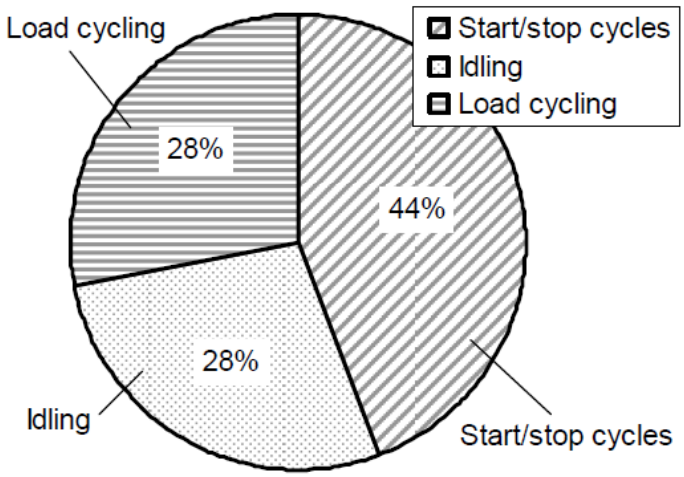

Figure 1.9. Contribution of degradation mode to entire degradation of FCEV during real-world driving [8]

In order to protect FCEVs from these degradation processes, both engineering and scientific approaches are needed. The former is related to the control technique of operating mode based on the degradation mechanism. The latter is related to the enhancement of durability of the MEA components. From the materials development point of view, the ability to control the Pt dissolution is still uncertain, whereas the carbon corrosion is prevented by the use of graphitized carbon support. In particular, the relationship between Pt dissolution and Pt oxide formation is very complicated to understand in the context of operating FCEVs. In order to understand this relationship, a fundamental scientific approach is needed and it should employ simple, well-defined experimental setups without complicated structures like those of catalyst layers.

1.4 Purpose of the PhD research project

Figure 1.10 presents schematic diagrams of a catalyst layer, catalyst and Pt-electrolyte interface. Although the thickness of CL is of the order of ca. 10 μm, the size of carbon-supported Pt is of the order of 40 nm and the individual Pt particle size is of the order of nm (~3 nm). As desired (HOR and ORR) and undesired reactions (e.g. Pt oxide formation and reduction, electrochemical and chemical Pt dissolution) take place at the nano-scale interface the interfacial structure changes and its components undergo chemical and physical changes. Therefore, it is essential to understand the Pt/electrolyte interfacial structure, the chemical and physical properties of both the electrolyte and Pt electrode in order to improve the activity and durability of Pt-based electrocatalyst.

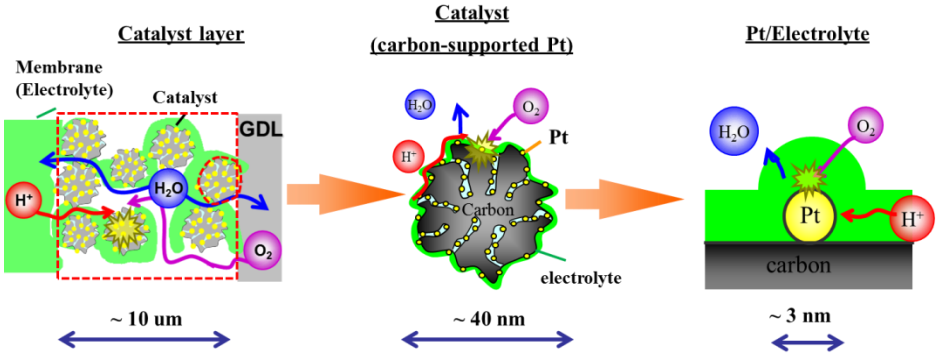

Figure 1.10. Schematics of catalyst layer, catalyst and Pt-electrolyte interface.

Although many studies have been conducted in the area of electrochemistry involving Pt electrodes (e.g. oxide formation and reduction, under-potential deposition of H, anion adsorption) in conventional acids, such as aqueous H_2SO_4 or $HClO_4$, they are not relevant to the performance of PEMFCs because Nafion® ionomer is used as electrolyte in catalyst layers of MEAs. Nafion® consists of a hydrophobic polytetrafluoroethylene (PTFE) backbone and perfluorinated side chains terminated by hydrophilic sulfonic acid group, as shown in Figure 1.11. In order to

elucidate the mechanisms of electrochemical reactions occurring in MEAs, it is essential to investigate the electrochemical behavior of Nafion® and to compare it to that of conventional inorganic acids. However, because Nafion® ionomer exists as a solid, not as a liquid, it is impractical to conduct such electrochemical experiments using a typical research-laboratory setup.

Trifluoromethanesulfonic acid (CF_3SO_3H, abbreviated as TFMSA) is the smallest fluorinated sulfonic acid and can serve as a suitable model compound mimicking the Nafion® ionomer [15-17]. Very preliminary studies suggest that the strength of anion adsorption on Pt surfaces in CF_3SO_3H is weaker than that in H_2SO_4; other anions (other sulfonic acid groups) originating from the Nafion® ionomer are also assumed to adsorb weakly on Pt surfaces [18,19]. These adsorbed anionic species can affect the mechanism and kinetics of electrochemical reactions. Interestingly, knowledge of the effect of anions, such as $CF_3SO_3^-$, HSO_4^-, SO_4^{2-}, or ClO_4^-, on the Pt surface oxide formation and reduction, under-potential deposition of H or Pt electro-dissolution is very limited. This very limited knowledge creates a research opportunity, which is pursued through this project. Consequently, research on the following three electrochemical reactions in CF_3SO_3H is the objective of my PhD research project: (i) the surface oxide formation; (ii) the under-potential deposition of H; and (iii) electrochemical and chemical dissolution of polycrystalline Pt. Some key experiments are also performed in aqueous H_2SO_4 and $HClO_4$ for a comparative analysis. It is expected that the outcome of this research will contribute to the development of guidelines for the design and manufacture of highly durable catalyst layers with low Pt usage and to the identification of operating conditions of PEMFCs which minimize Pt dissolution.

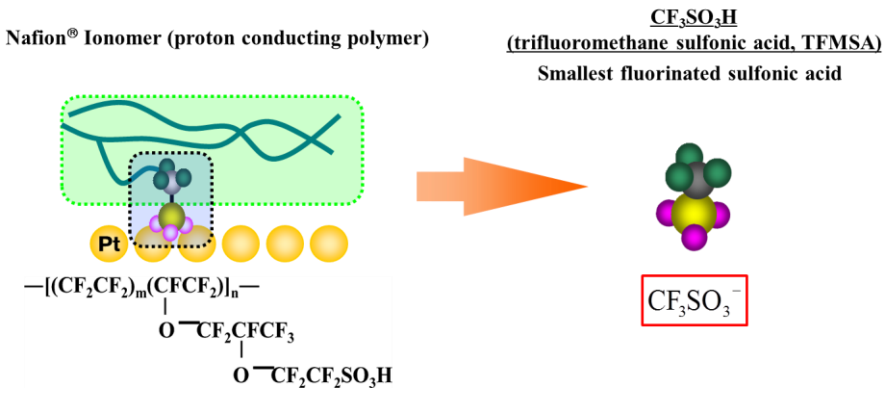

Figure 1.11. Schematic of structure of Nafion® and CF_3SO_3H

1.5 References

(1) O. Edenhofe., R. Pichs-Madruga, Y. Sokona, E. Farahani, S. Kadner, K. Seyboth, A. Adler, I. Baum, S. Brunner, P. Eickemeier, B.Kriemann, J. Savolainen, S. Schlomer, C. von Stechow, T. Zwickel, J. C. Minx (eds), International Intergovernmental Panel on Climate Change (IPCC) 2014: Summary for Policymakers, In: Climate Change 2014, Mitigation of Climate Change. Contribution of Working Group III to the Fifth Assessment Report of the Intergovernmental Panel on Climate Change, Cambridge University Press, Cambridge, United Kingdom and New York, NY, USA.

(2) T. F. Stocker, D. Qin, G.-K. Plattner, M. Tignor, S. K. Allen, J. Boschung, A. Nauels, Y. Xia, V. Bex, P. M. Midgley, International Intergovernmental Panel on Climate Change (IPCC) 2014: Summary for Policymakers. In: Climate Change 2013: The Physical Science Basis. Contribution of Working Group I to the Fifth Assessment Report of the Intergovernmental Panel on Climate Change. Cambridge University Press, Cambridge, United Kingdom and New York, NY, USA.

(3) World Business Council for Sustainable Development (WBCSD), Mobility 2030: Meeting the Challenges to Sustainability, 2004. www.wbcsd.org/web/publications/mobility/mobility-full.pdf

(4) U. S. Department of Energy, The Department of Energy Hydrogen and Fuel Cells Program Plan, www.hydrogen.energy.gov/pdfs/program_plan2011.pdf

(5) G. Merle, M. Wessling, K. Nijmeijer, J. Memb. Sci. **377** 1 (2011).

(6) A. Kirubakaran, S. Jain, R. K. Nema, Renew. Sust. Energy. Rev. **13** 2430 (2009).

(7) Y. Wang, K. S. Chen, J. Mishler, S. C. Cho, X. C. Adroher, Applied Energy, **88** 981 (2011).

(8) D. Papageorgopoulos, 2013 Fuel Cells Annual Merit Review (U.S. Department of Energy, Arlington, Virginia, 2013).

(9) J Sinha, S Lasher, Y Yang, P Kopf, 2010 Fuel Cells Annual Merit Review, (U.S. Department of Energy, Washington, DC, 2010).

(10) R. Shimoi, T. Aoyama, A. Iiyama, SAE Int. J. Engines **2**, 960 (2009).

(11) H. Tang, Z. Qi, M. Ramani, J. F. Elter, J. Power Sources **158**, 1306 (2006).

(12) A. Ohma, K. Shinohara, A. Iiyama, T. Yoshida, A. Daimaru, ECS Trans. **41**, 775 (2011)

(13) L. Xing, M.A. Hossain, M. Tian, D. Beauchemin, K.T. Adjemian, G. Jerkiewicz, Electrocatalysis **5**, 96 (2014)

(14) S. Chen, H. A. Gasteiger, K. Hayakawa, T. Tada, Y. Shao-Horn, J. Electrochem. Soc. **157**, A82 (2010)

(15) A. Ohma, K. Fushinobu, K. Okazaki, Electrochim. Acta **55**, 8829 (2010)

(16) G. Attard, A. Brew, K. Hunter, J. Sharman, E. Wright, Phys. Chem. Chem. Phys. **16**, 13689 (2014)

(17) A. Ohma, T. Ichiya, K. Fushinobu, K. Okazaki, Surf. Sci. **604**, 965 (2010)

(18) M. Teliska, V. Murthi, S. Mukerjee, D. E. Ramaker, J. Phys. Chem. C **111**, 9267 (2007)

(19) A. Berna, J. M. Feliu, L. Gancs, S. Mukerjee, Electrochem. Commun. **10**, 1695 (2008)

Chapter 2

Surface Oxide Growth on Platinum Electrode in Aqueous Trifluoromethanesulfonic Acid

2.1 Introduction

Polymer electrolyte membrane fuel cells (PEMFCs) are promising primary power sources for automotive applications. However, power density, durability, and cost reduction are some of the main challenges that hinder the commercialization of fuel cell electric vehicles (FCEVs), with the cost reduction being the most challenging issue [1,2]. A membrane electrode assembly (MEA), which is one of the main components of fuel cells, is composed of a polymer electrolyte membrane as a proton conductor, catalyst layers as electrodes for the oxygen reduction reaction (ORR) and hydrogen oxidation reaction (HOR), and gas diffusion layers. Among these components, the catalyst layers account for a large portion of the overall MEA cost [2], because they contain precious platinum (Pt) in the form of nanoparticles. In order to commercialize FCEVs, it is of great importance to reduce the Pt loading in MEAs without sacrificing their performance and durability. Thus, Pt needs to be utilized the most effectively in order to reduce the Pt loading in MEAs.

Automotive fuel cells operate in a relatively high potential range at which the Pt surface undergoes partial or complete oxidation [3-6]. The oxide on Pt cathode affects not only the mechanism and kinetics of ORR by modifying its electrocatalytic activity [7-10] but also its

durability [11-20]. A passive layer residing on Pt reduces the reactivity of the underlying metallic Pt, thus offering protection against corrosion [11-17]. However, the oxide growth proceeds with the formation of a quasi-three-dimensional lattice (quasi-3D lattice) that might facilitate Pt dissolution [18-20]; exposed Pt surface could undergo dissolution. Thus, there exists a need for good understanding of the Pt oxide growth behavior and the stability of Pt oxides under conditions that mimic operating PEMFCs.

The growth of Pt surface oxide under electrochemical conditions has been studied extensively [21-32]. At present, it is accepted that the initial stages of Pt oxide growth involve the discharge of H_2O molecules and lead to the formation of electro-adsorbed O (chemisorbed O, O_{chem}) and the departure of protons [31]. In a CV transient for Pt(poly), this process commences at 0.85 V and as the potential reaches 1.15 V about half a monolayer of O_{chem} is formed (Equation 2.1) [31,32].

$$Pt(s) + H_2O(l) \xrightarrow{\text{O electro-adsorption}} Pt^{\delta+} - O_{chem}{}^{\delta-} + 2\,H^+(aq) + 2\,e^- \qquad (2.1)$$

The formation of $Pt^{\delta+}$–$O^{\delta-}$ surface species is followed by the interfacial place exchange between O_{chem} and Pt surface atoms (Pt_{surf}); the process leads to a quasi-3D lattice comprising Pt^{2+} and O^{2-} (Equation 2.2).

$$Pt_{surf}{}^{\delta+} - O_{chem}{}^{\delta-} \xrightarrow{\text{interfacial place exchange}} \left(Pt^{2+} - O^{2-}\right)_{\text{quasi-3D lattice}} \qquad (2.2)$$

In a CV transient for Pt(poly), this process commences at ca. 1.15 V and corresponds to the O_{chem} coverage (θ_O) of ca. 0.5. It is accompanied by the completion of charge density

redistribution between $Pt^{\delta+}$ and $O^{\delta-}$, which become cation-like (Pt^{2+}) and anion-like (O^{2-}). Importantly, the Pt surface oxidation proceeds with the formation of $Pt^{\delta+}$–$O^{\delta-}$ and Pt^{2+}–O^{2-} as *stable surface compounds* and without the development of Pt–OH_{ads} (it may not be excluded that Pt–OH_{ads} exists as a short-lived species that acts as an intermediate of the process) [29-33]. The interfacial place-exchange is driven by latter repulsive interactions between alike aligned $Pt^{\delta+}$–$O^{\delta-}$ surface dipoles and gives rise to a *logarithmic kinetic law*. After completion of the place-exchange and the charge density redistribution, a strong electric field of the order of 10^8–10^9 V m^{-1} establishes across the metal/oxide interface. It drives the escape of the Pt^{2+} cation from the metal into the oxide, which becomes the rate determining step and the process gives rise to an *inverse-logarithmic kinetic law* [34,35].

Although numerous papers report on the Pt oxide growth in aqueous H_2SO_4, $HClO_4$ and NaOH solutions, there are very few systematic studies on the subject in aqueous CF_3SO_3H solutions, although CF_3SO_3H is the smallest fluorinated sulfonic acid and can serve as a molecular model mimicking the Nafion ionomer [36,37]. Since in the case of MEAs Pt surface sites can be occupied by adsorbed anions (the sulfonic acid group) originating from the Nafion ionomer, these adsorbed species can affect the ORR mechanism and kinetics as well as the durability of Pt nanoparticles [36,38-40]. In particular, the knowledge of impact of the anion nature, such as $CF_3SO_3^-$, HSO_4^-, or $HClO_4^-$, on the Pt oxide growth behavior is very limited [41,42]. Elsewhere, it was demonstrated that in the case of CF_3SO_3H the anion interaction with the Pt surface is weaker than in the case of H_2SO_4 or H_3PO_4 [43,44] Therefore, it is reasonable to assume that the Pt oxide growth in CF_3SO_3H might be more pronounced than that in H_2SO_4 due to the weaker anion adsorption.

In this chapter, we present a significantly revised and expanded mechanistic diagram of the Pt surface oxide growth that takes into account interactions of the hydronium cation and the anion with the Pt surface prior to and at different stages of its oxidation [31,32]. We report on the surface oxide growth on Pt(poly) in aqueous CF_3SO_3H solution and examine the influence of polarization potential (E_p), polarization time (t_p), and temperature (T) on the amount of oxide formed. We evaluate the critical thickness X_1 introduced by Mott and Cabrera and determine that the thickness (d_{ox}) of the surface oxides grown under the E_p, t_p and T conditions reported here is always below the X_1 value [34,35]. This observation implies that the oxides are very thin and follow either the interfacial place-exchange or the metal cation escape mechanism. We advance the interfacial place-exchange oxide growth theory by taking into account repulsive dipole-dipole interactions that through local depolarization effects modify the surface potential. We analyze our new results within the framework of these two theories and determine the dipole moment of surface PtO (μ_{PtO}), the potential drop (V_{ox}) and the electric field (E_{ox}) across the oxide. Finally, we compare the results obtained in aqueous CF_3SO_3H to those obtained in aqueous H_2SO_4 [45].

2.2 Experimental

2.2.1 Electrode Preparation

The Pt(poly) working electrode was prepared from ultra-high purity wire (99.999% in purity, and 0.5 mm in diameter). The details of the procedure employed are described elsewhere [6]. The electrode was degreased in hot acetone under reflux followed by rinsing with ultra-high purity ethanol. Then it was cleaned in concentrated H_2SO_4 for 24 hours and rinsed several times (at least ten times) with ultra-high purity water (MilliPore, Milli-Q3; resistivity $\rho \geq 18.2$ MΩ cm).

Its geometric surface area (A_{geom}) was determined by measuring the length of the Pt wire using a Vernier microscope; it was determined to be 0.27 ± 0.01 cm^2. The real surface area (A_r), also called the electrochemically active surface area (A_{ecsa}), of the Pt electrode was determined from the charge of the under-potential deposition of H (UPD H) [46]. The electrode's roughness factor ($R' = A_{ecsa} / A_{geom}$) was found to be ca. 1.6. The counter electrode was a Pt mesh (99.999% in purity) connected to Pt wire (99.999% in purity, and 0.5 mm in diameter) that was sealed in a glass tube. The reference electrode was Pt/Pt black placed in the same electrolyte but in a separate compartment through which H_2 (p_{H2} = 1 atm) was passed. It served as a reversible hydrogen electrode (RHE). The RE compartment was electrolytically connected to the WE compartment by means of a Luggin capillary. All potentials measured experimentally and referred to in this paper are expressed with respect to RHE.

2.2.2 Electrolyte and Electrochemical cell

High purity 0.1 M aqueous CF_3SO_3H solution was prepared from concentrated CF_3SO_3H (ReagentPlus, Sigma-Aldrich, >99%) and ultra-high purity water (MilliPore, Milli-Q3; $\rho \geq 18.2$ MΩ cm). The concentrated CF_3SO_3H was used as received without any further purification. Ultra-high purity N_2(g) was passed through and above the electrolyte in the WE compartment in order to expel any reactive gases and to create a neutral-gas environment. The stability and reproducibility of CV profiles over prolonged periods of time, which is a measure of the purity of the experimental setup including the electrolyte solution, was carefully verified. The glassware was cleaned according to well-established procedures [24, 47].

2.2.3 Electrochemical Procedure

A surface oxide was grown on Pt(poly) electrode under potentiostatic conditions by applying a constant polarization potential in the $1.10 \leq E_p \leq 1.50$ V range, for a controlled polarization time in the $1.0 \times 10^0 \leq t_p \leq 1.0 \times 10^4$ s range, and at a fixed temperature in the $278 \leq T \leq 333$ K range. The electrochemical cell was immersed in a water bath the temperature of which was monitored and controlled to within 1 K. The electrolyte level in the cell was maintained below the water level in the bath to ensure uniform temperature distribution. In each separate experiment, a surface oxide formed by potentiostatic polarization was subsequently reduced in a single negative-going CV transient at a potential scan rate of $s = 50$ mV s^{-1}. All CV oxide-reduction profiles show one feature, the so-called OC1 peak, which corresponds to the reduction of surface PtO to metallic Pt. The oxide reduction CV profiles were integrated and the oxide charge density (q_{ox}) values were determined. A Bio Logic Model SP-150 potentiostat controlled with proprietary software was used to conduct the oxide growth experiments, and to acquire and process data.

2.3 Results and Discussion

2.3.1 Oxide Formation in CF_3SO_3H as a Function of Polarization Potential, Time, and Temperature

Figure 2.1 shows two CV profiles for Pt(poly) electrode in 0.1 M aqueous CF_3SO_3H and 0.5 M aqueous H_2SO_4 obtained at $s = 50$ mV s^{-1} and $T = 293$ K. The measurements were performed in 0.1 M aqueous CF_3SO_3H because experimental work in 0.5 M CF_3SO_3H was

impossible due to the five-fold increase in the amount of uncontrollable impurities that adsorbed on the Pt surface making meaningful experiment practically impossible. This is the reason for conducting experiments and reporting data for 0.1 M aqueous CF_3SO_3H solution. On the other hand, 0.5 M aqueous H_2SO_4 solution was employed in order to relate new finding to our past results (and to report on their reproducibility) as well as to relate our data to those of Conway et al [6, 31, 32]. Because the 0.1 M aqueous CF_3SO_3H solution also contained impurities (although five times less than 0.5 M solution) that could adsorb on the Pt(poly) electrode, the latter needs to be cycled several times between 0.05 and 1.40 V prior to any new experiment in order to desorb impurities through oxidative desorption. This approach allowed the Pt(poly) electrode to be maintained fairly impurity-free (we accepted that the electrode was considered contaminated when at least 5% of its surface became blocked by impurities). The CV transients in Figure 2.1 reveal the usual features that correspond to the adsorption and desorption of H_{UPD}, and the formation and reduction of Pt surface oxide, the composition of which is PtO [31, 48]. In the case of the CF_3SO_3H solution, the onset potential of PtO formation is slightly lower than that in the H_2SO_4 solution. The lack of any other CV features suggests that the surface oxide growth mechanism in the CF_3SO_3H solution is the same as in the H_2SO_4 solution and does not produce PtOH as a stable surface compound [29-31].

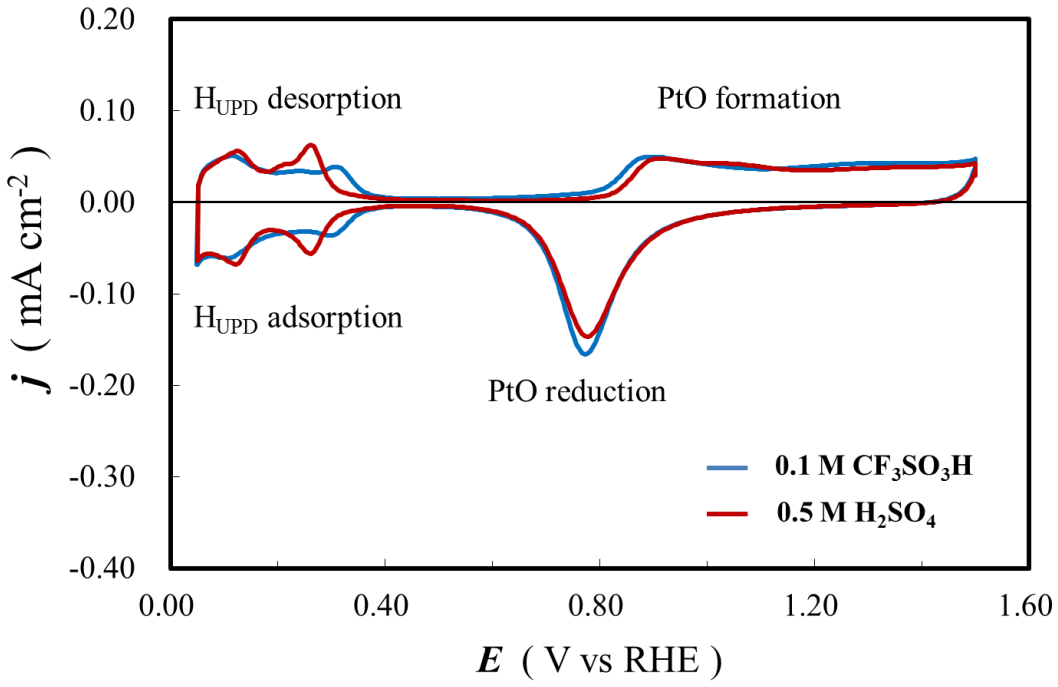

Figure 2.1. CV profiles for Pt(poly) electrode in 0.1 M aqueous CF_3SO_3H (blue line) and 0.5 M aqueous H_2SO_4 (red line) obtained at s = 50 mV s^{-1} and T = 293 K.

The formation (anodic) and reduction (cathodic) oxide charge density values in the CF_3SO_3H solution are $q_{ox,form}$ = 578 μC cm^{-2} and $q_{ox,red}$ = 494 μC cm^{-2}; in the H_2SO_4 solution they are $q_{ox,form}$ = 500 μC cm^{-2} and $q_{ox,red}$ = 463 μC cm^{-2}. The larger $q_{ox,form}$ and $q_{ox,red}$ values in the CF_3SO_3H solution compared with in the H_2SO_4 solution are interpreted in terms of weaker anion adsorption, the desorption of which has to take place prior to the commencement of the PtO formation. The difference in the $q_{ox,form}$ and $q_{ox,red}$ values ($q_{ox,form} > q_{ox,red}$) is due to three concurrently occurring processes: (i) anodic Pt electro-dissolution; (ii) the anodic oxygen evolution reaction (OER); and (iii) oxidative desorption of trace impurities that are always present in aqueous electrolytes and easily adsorb on Pt materials (even if in trace amounts). Because commercial, high-purity CF_3SO_3H is not as pure as H_2SO_4, unavoidably it contains

impurities that undergo first adsorption and then oxidative desorption generating an anodic charge. In addition, there are some differences at the onset of UPD H and in the shape of these CV features. In the CF_3SO_3H solution, the adsorption of H_{UPD} starts at a potential that is about 0.05 V higher than that in the H_2SO_4 solution. Moreover, in the CF_3SO_3H solution the CV peaks have lower current density (j) values than in the H_2SO_4 solution; this variance is attributed to different anion adsorption strengths in these two electrolytes [49,50]. The H_{UPD} adsorption (cathodic) and desorption (anodic) charge (Q) values in the CF_3SO_3H and H_2SO_4 solutions agree to within 2% and are Q_{Hupd} = 84.2 μC cm^{-2} in the CF_3SO_3H solution and Q_{Hupd} = 93.0 μC cm^{-2} in the H_2SO_4 solution

Figure 2.2 shows a series of CV oxide-reduction profiles for oxides formed on Pt(poly) in 0.1 M aqueous CF_3SO_3H at $1.10 \leq E_p \leq 1.50$ V, $t_p = 1.0 \times 10^4$ s and T = 293 K. Because all CV transients reveal only the OC1 peak, under these conditions PtO is the surface compound that develops. The OC1 peak potential shifts ca. 100 mV towards lower values with the rise in E_p and its q_{ox} values increase. This behavior suggests that the increase in E_p, while maintaining t_p and T constant, makes the surface oxide thicker and thermodynamically more stable. The inset in Figure 2.2 shows two plots of q_{ox} versus E_p; the blue diamonds refer to the CV oxide-reduction profiles presented in the main graph and the red diamonds refer to analogous measurements performed in 0.5 M aqueous H_2SO_4; in both cases the q_{ox} values are corrected for the double layer charging. In the case of $1.10 \leq E_p \leq 1.30$ V, the two plots almost overlap each other; in the case of E_p = 1.40 V, there is a slight difference in the q_{ox} values obtained in the CF_3SO_3H and H_2SO_4 solutions; and in the case of E_p = 1.50 V, the q_{ox} value obtained in the CF_3SO_3H solution is ca. 10% higher than the q_{ox} value obtained in the H_2SO_4 solution. Although Figure 2.2 presents results for only one value of t_p and T, the results are representative of the overall trend observed for other t_p and T values.

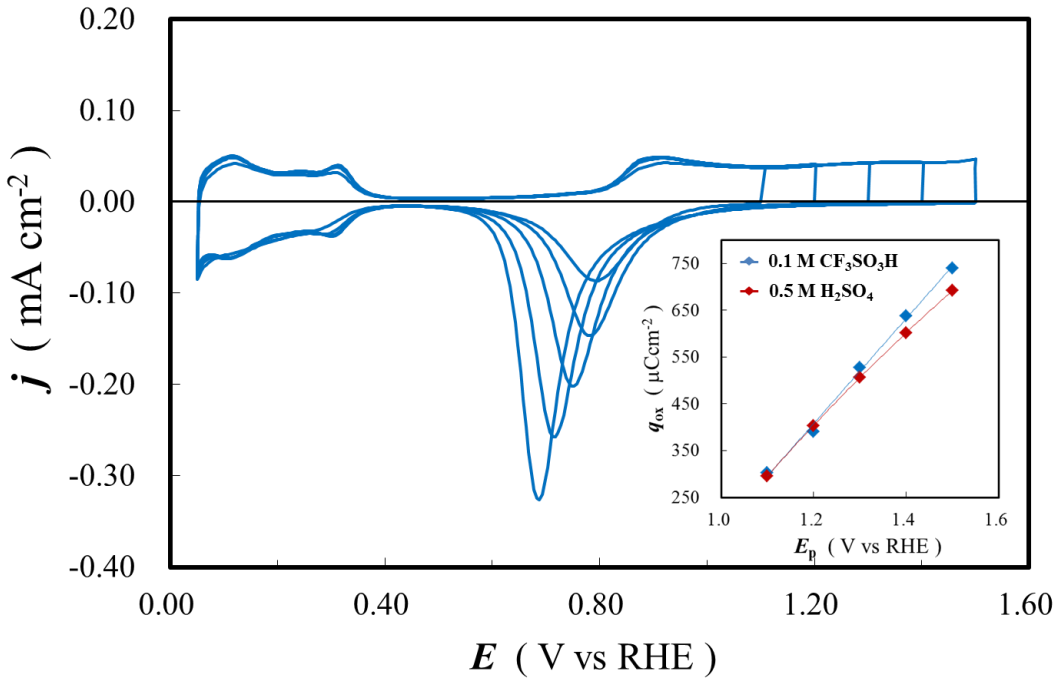

Figure 2.2. Series of CV oxide-reduction profiles for oxides formed on Pt(poly) in 0.1 M aqueous CF_3SO_3H at $1.10 \leq E_p \leq 1.50$ V, $t_p = 1.0 \times 10^4$ s and $T = 293$ K. The inset shows two plots of q_{ox} versus E_p; the blue diamonds refer to the CV oxide-reduction profiles presented in the main graph and the red diamonds refer to analogous measurements performed in 0.5 M aqueous H_2SO_4.

Figure 2.3 shows a series of CV oxide-reduction profiles for oxides formed on Pt(poly) in 0.1 M aqueous CF_3SO_3H at $E_p = 1.40$ V for $t_p = 1.0 \times 10^4$ s and in the $278 \leq T \leq 333$ K range. Because all CV transients reveal only the OC1 peak, under these conditions PtO is the stable surface compound that develops. The potential of the OC1 reduction peak shifts by ca. 10 mV towards higher values as T is raised; a similar behavior was observed in the H_2SO_4 solution [6]. A slightly different behavior was observed in the case of Au(poly) electrode in aqueous H_2SO_4 solutions in the sense that a similar T rise resulted in the OC1 peak being shifted by ca. 60 mV towards higher potentials [51]. This suggests that the impact of T variation on the

thermodynamic stability of PtO is smaller than in the case of AuO. On the other hand, the behavior observed for Pt(poly) resembles that observed for Pd(poly) electrodes in aqueous H_2SO_4 solutions [52].

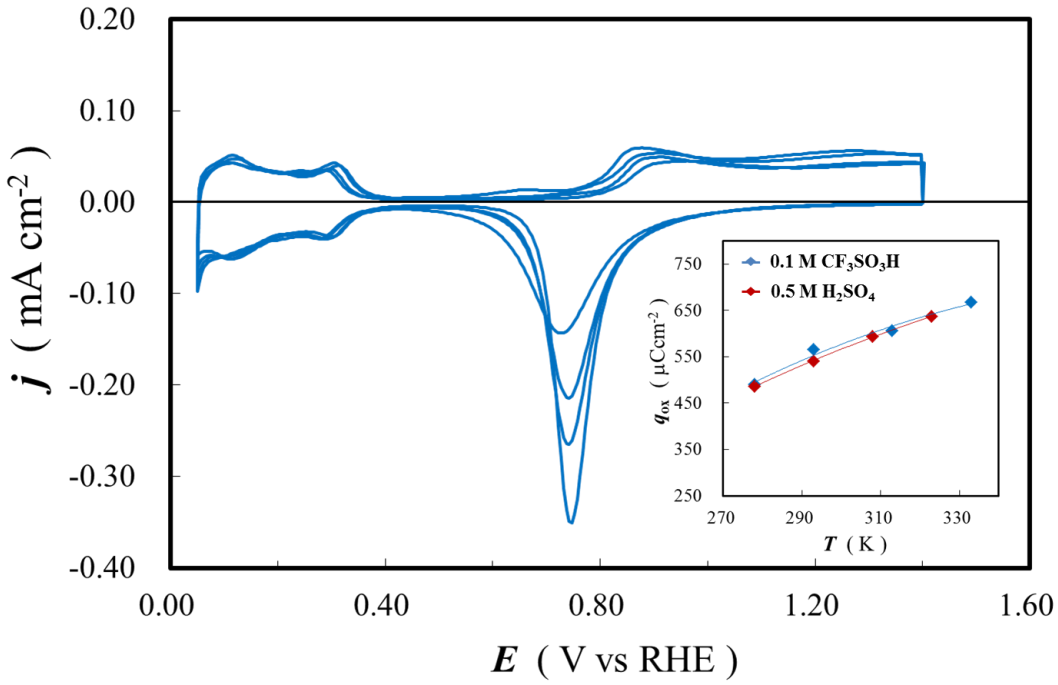

Figure 2.3. Series of CV oxide-reduction profiles for oxides formed on Pt(poly) in 0.1 M aqueous CF_3SO_3H at $278 \leq T \leq 333$ K, $E_p = 1.40$ V and $t_p = 1.0 \times 10^4$ s. The inset shows two plots of q_{ox} versus T; the blue diamonds refer to the CV oxide-reduction profiles presented in the main graph and the red diamonds refer to analogous measurements performed in 0.5 M aqueous H_2SO_4.

The inset in Figure 2.3 shows two plots of q_{ox} versus T; the blue diamonds refer to the CV oxide-reduction profiles presented in the main graph and the red diamonds refer to analogous measurements performed in 0.5 M aqueous H_2SO_4; in both cases the q_{ox} values are corrected for the double layer charging. It is interesting to observe that the two plots practically overlap. Because this graph refers to $E_p = 1.40$ V and because the results presented in the inset in Figure 2.2 reveal that the values of q_{ox} are the same or very similar for $E_p \leq 1.40$ V, this trends is expected. However, in the case of $E_p \geq 1.50$ V the values of q_{ox} obtained in the CF_3SO_3H solution

are higher than those in the H_2SO_4 solution (see the inset in Figure 2.2) regardless of the applied temperature.

Figure 2.4 shows a series of CV oxide-reduction profiles for oxides formed on Pt(poly) in 0.1 M aqueous CF_3SO_3H at E_p = 1.40 V, T = 293 K and for $1.0 \times 10^0 \leq t_p \leq 1.0 \times 10^4$ s. Because all CV transients reveal only the OC1 peak, under these conditions PtO is the surface compound that develops. The potential of the OC1 peak shifts towards lower values by ca. 70 mV as t_p is raised. The inset in Figure 2.4 shows two plots of q_{ox} versus log t_p; the blue diamonds refer to the CV oxide-reduction profiles presented in the main graph and the red diamonds refer to analogous measurements performed in 0.5 M aqueous H_2SO_4; in both cases the q_{ox} values are corrected for the double layer charging. The relationship in the q_{ox} versus log t_p plots over a certain q_{ox} range suggests that the process follows a logarithmic growth law or inverse logarithmic. The different slopes of the q_{ox} versus log t_p plots indicate that some physical parameters of the process are different in these two electrolyte solutions. The origin of this behavior is discussed in Section 2.4.4.

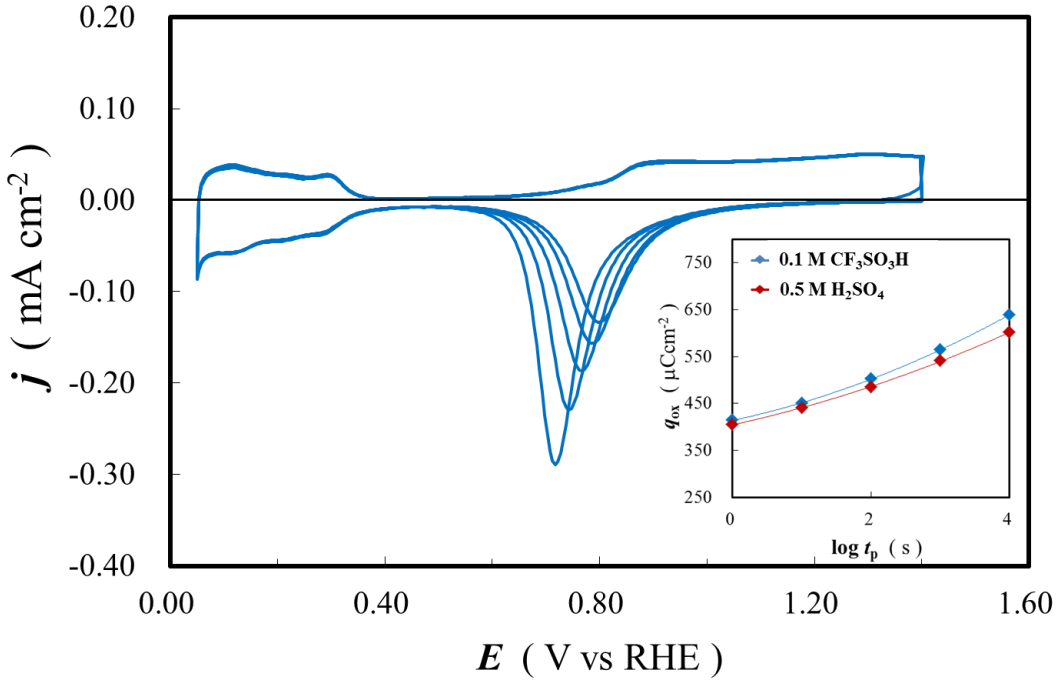

Figure 2.4. Series of CV oxide-reduction profiles for oxides formed on Pt(poly) in 0.1 M aqueous CF_3SO_3H at $1.0 \times 10^0 \leq t_p \leq 1.0 \times 10^4$ s, E_p = 1.40 V and T = 293 K. Inset shows two plots of q_{ox} versus log t_p; the blue diamonds refer to the CV oxide-reduction profiles presented in the main graph and the red diamonds refer to analogous measurements performed in 0.5 M aqueous H_2SO_4

2.3.2 Critical Thicknesses X_o and X_1

Mott and Cabrera originally proposed a theoretical treatment of oxide-growth kinetics and defined two critical thicknesses (parameters) X_o and X_1 expressed by the following equations [34, 35];

$$X_o = \sqrt{\frac{\varepsilon\, k_B\, T}{8\pi\, n\, q^2}} \tag{2.3}$$

$$X_1 = \frac{q\, a\, V_{ox}}{k_B\, T} \tag{2.4}$$

where ε is the dielectric constant of the oxide film and $\varepsilon = \varepsilon_0\, \varepsilon_r$, where ε_o is the vacuum dielectric constant and equals 8.854 10^{-12} J^{-1} C^2 m^{-1} and ε_r the relative dielectric constant of the oxide/electrolyte interface; n is the number of metal ions per unit volume; q is the metal cation charge; V_{ox} is the potential drop across an oxide layer; a is the distance between metal cations in the oxide; k_B is Boltzmann's constant; and T is the temperature. The applicability of a given oxide growth theory to a system under investigation depends on the relationship between the actual oxide thickness (d_{ox}) and the parameters X_o and X_1. Elsewhere, it was explained that $X_o > X_1$ [53]. This is a very important observation because the determination or even estimation of X_o for ultra-thin metallic oxides residing on metallic surfaces is often impossible because their values of ε remain unknown. However, the value of X_1 can be estimated, as shown elsewhere for surface oxides on Rh electrodes [53]. The potential drop across an oxide layer (V_{ox}) depends on the applied oxide growth potential and is of the order of 0.2-1.0 V. Figure 2.5A presents a series of X_1 values for $0.3 \le V_{ox} \le 1.0$ V with an interval of $\Delta V_{ox} = 0.1$ V and for T = 278, 293, 313, and

333 K. The results demonstrate that under such conditions X_1 adopts values in the 7.2-29 nm range. Because these thickness values correspond to some tens of MLs of PtO and because the thickness of oxide layers formed in the course of research does not exceed 2 MLs, we may conclude that in our case $d_{ox} << X_1$ (and also $d_{ox} << X_o$ because $X_o > X_1$). The very initial oxide growth in the sub-monolayer and monolayer range is limited by the interfacial place exchange. Once the oxide thickness has reached a certain limiting thickness, strong electric field establishes across the oxide and stimulate the escape of metal cations from the metal into the oxide. The oxide growth through the interfacial place exchange gives rise to a logarithmic growth law ($q_{ox} \sim \log t_p$), while the growth through the metal cation escape gives rise to an inverse-logarithmic growth law ($q_{ox}^{-1} \sim \log t_p$).

In general, the amount of oxide can be expressed in several ways, such as oxide thickness (d_{ox}), oxide mass (m_{ox}), number of oxide monolayers (n_{ox}), oxide charge (Q_{ox}) or oxide charge density (q_{ox}). Because in electrochemistry the amount of oxide is typically expressed as Q_{ox} or q_{ox}, it is practical to convert the critical oxide thickness X_1 into critical oxide charge density ($q_{crit,1}$). The conversion of X_1 to $q_{crit,1}$ is accomplished by using 440 μC cm^{-2} of 1 ML of PtO and its thickness as d_{1ML} = 3.444 Å [6]. Figure 2.5B presents the values of $q_{crit,1}$ as a function of V_{ox} and T, and demonstrates that under such conditions $q_{crit,1}$ adopts values in the 4.6-18 mC cm^{-2} range.

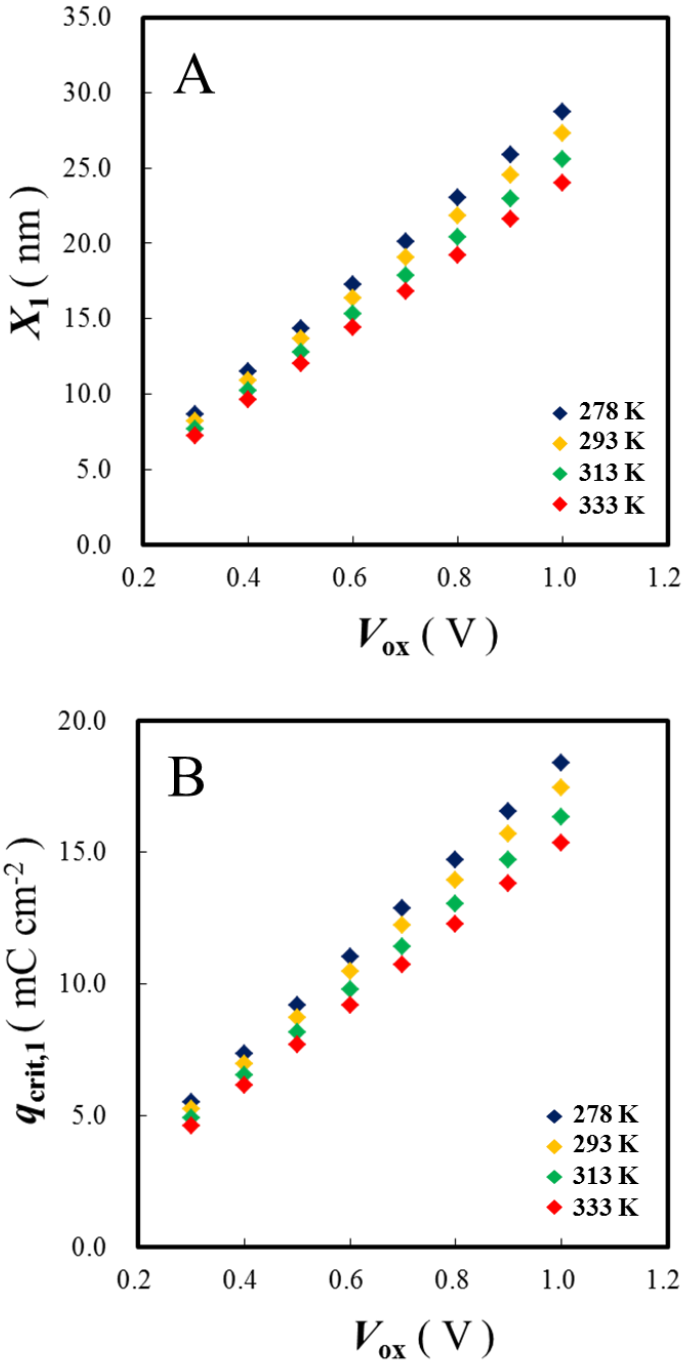

Figure 2.5. Series of X_1 (A) and $q_{crit,\,1}$ (B) values for $0.3 \leq V_{ox} \leq 1.0$ V with an interval of ΔV_{ox} = 0.1 V and for T = 278, 293, 313, and 333 K.

2.3.3 Elementary Steps Involved in the Platinum Surface Oxide Growth

Platinum oxide growth by potentiostatic polarization can be studied over a wide range of E_p, t_p and T values and such acquired data can be theoretically treated using different oxide growth mechanisms and associated kinetic equations. The main steps involved in the formation of Pt surface oxide, whose thickness does not exceed 2 equivalent MLs of PtO, were discussed elsewhere [31] and are summarized in the Introduction. However, that model was an over-simplification and did not take into account the possible interactions of hydronium cations, anions, and water molecules with the Pt surface.

Figure 2.6 presents a more detailed visualization of the process as a function of the applied potential and contains eight graphs, each for a different applied potential. Figure 2.6A: $E_{pzc} < E < E_{PtO/Pt}$, where E_{pzc} refers to the potential of zero charge and in the case of aqueous H_2SO_4 solution is close to the onset of UPD H; $E_{Pt/PtO}$ refers to the onset potential of PtO formation on Pt_{surf}. In this potential range, the Pt surface charge is positive ($q_{Pt} > 0$) and the surface attracts H_2O molecules through physisorption (surface dipole-water dipole interactions) and anions through chemisorption (specific adsorption); the surface coverage of O_{chem} adatoms is zero ($\theta_O = 0$). Figure 2.6B: $E_{Pt/PtO} < E < E_{pl\text{-}exch}$, where $E_{pl\text{-}exch}$ refers to the onset potential of the interfacial place exchange. In this potential range, some initially physisorbed water molecules (H_2O_{phys}) undergo discharge (Equation 2.5) with the formation of O_{chem} as a stable surface compound and the departure of two hydrated protons ($H^+(aq)$); the process is accompanied by charge density redistribution between O_{chem} and Pt_{surf}, and reductive desorption of anions (Equation 2.6).

$$Pt(s) + H_2O_{phys} \rightarrow Pt^{\delta+} - O_{chem}{}^{\delta-} + 2\,H^+(aq) + 2\,e^- \qquad (2.5)$$

$$Pt(s) + H_2O_{phys} \rightarrow Pt^{\delta+} - O_{chem}{}^{\delta-} + 2\,H^+(aq) + 2\,e^- \qquad (2.6)$$

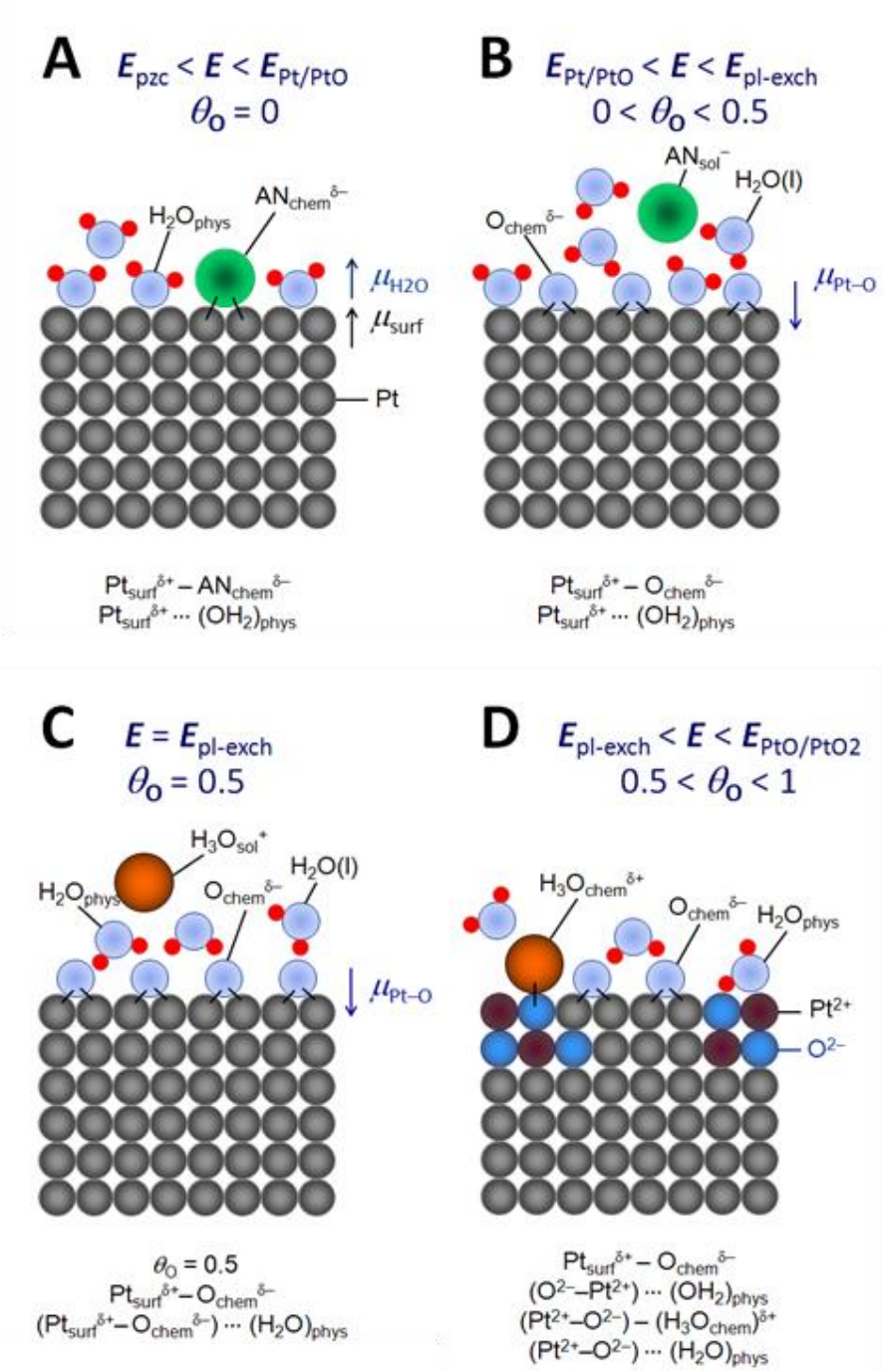
A
$E_{pzc} < E < E_{Pt/PtO}$
$\theta_O = 0$
H_2O_{phys}
$AN_{chem}^{\delta-}$
μ_{H2O}
μ_{surf}
Pt
$Pt_{surf}^{\delta+} - AN_{chem}^{\delta-}$
$Pt_{surf}^{\delta+} \cdots (OH_2)_{phys}$
B
$E_{Pt/PtO} < E < E_{pl\text{-}exch}$
$0 < \theta_O < 0.5$
AN_{sol}^{-}
$H_2O(l)$
$O_{chem}^{\delta-}$
μ_{Pt-O}
$Pt_{surf}^{\delta+} - O_{chem}^{\delta-}$
$Pt_{surf}^{\delta+} \cdots (OH_2)_{phys}$
C
$E = E_{pl\text{-}exch}$
$\theta_O = 0.5$
$H_3O_{sol}^{+}$
H_2O_{phys}
$H_2O(l)$
$O_{chem}^{\delta-}$
μ_{Pt-O}
$\theta_O = 0.5$
$Pt_{surf}^{\delta+} - O_{chem}^{\delta-}$
$(Pt_{surf}^{\delta+} - O_{chem}^{\delta-}) \cdots (H_2O)_{phys}$
D
$E_{pl\text{-}exch} < E < E_{PtO/PtO2}$
$0.5 < \theta_O < 1$
$H_3O_{chem}^{\delta+}$
$O_{chem}^{\delta-}$
H_2O_{phys}
Pt^{2+}
O^{2-}
$Pt_{surf}^{\delta+} - O_{chem}^{\delta-}$
$(O^{2-}-Pt^{2+}) \cdots (OH_2)_{phys}$
$(Pt^{2+}-O^{2-}) - (H_3O_{chem})^{\delta+}$
$(Pt^{2+}-O^{2-}) \cdots (H_2O)_{phys}$

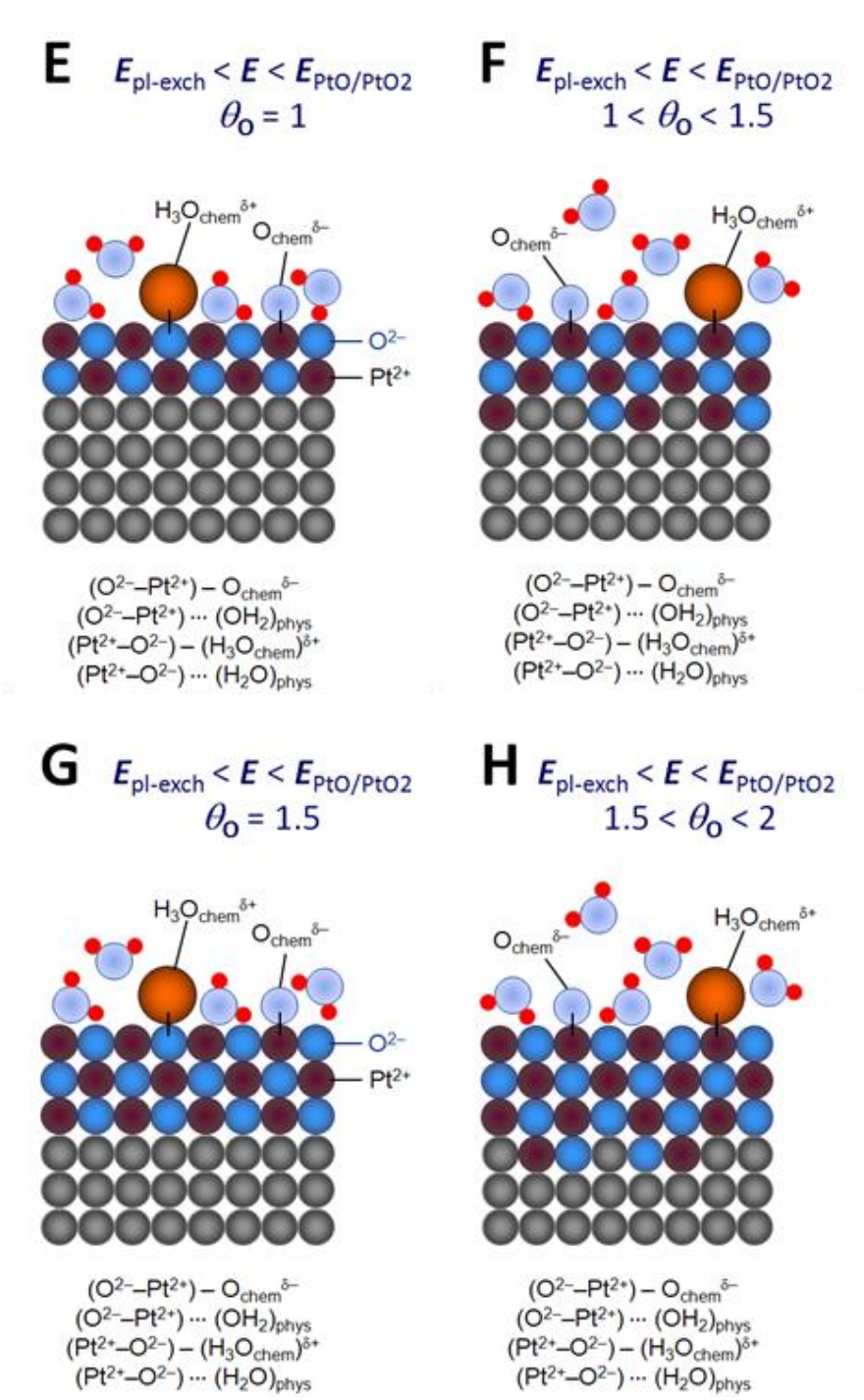

Figure 2.6. Detailed visualization of the process as a function of the applied potential and contains eight graphs, each for a different applied potential. A; $E_{pzc} < E < E_{PtO/Pt}$, $\theta_O = 0$ B; $E_{Pt/PtO} < E < E_{pl\text{-}exch}$, $0 < \theta_O < 0.5$, C; $E = E_{pl\text{-}exch,}$ $\theta_O = 0.5$, D; $E_{pl\text{-}exch} < E < E_{PtO/PtO2}$, $0.5 < \theta_O < 1$, E; $E_{pl\text{-}exch} < E < E_{PtO/PtO2}$, $\theta_O = 1$, F; $E_{pl\text{-}exch} < E < E_{PtO/PtO2,}$ $1 < \theta_O < 1.5$, G; $E_{pl\text{-}exch} < E < E_{PtO/PtO2,}$ $\theta_O = 1.5$, and H; $E_{pl\text{-}exch} < E < E_{PtO/PtO2}$, $1.5 < \theta_O < 2$

The formation of $Pt^{\delta-}$–$O_{chem}{}^{\delta+}$ surface species locally modifies the surface potential and, consequently, the surface dipole moment. Because $0 < \theta_O < 0.5$, there are some unoccupied Pt surface atoms that attract H_2O molecules through physisorption. Figure 2.6C: $E = E_{pl\text{-}exch}$ is the critical potential at which $\theta_O = 0.5$ in the case of Pt(100) electrode surface, as depicted in the drawing. In the case of Pt(100) and $\theta_O = 0.5$ half of the surface is occupied by O_{chem} adatoms and no interfacial place exchange is observed. The development of O_{chem} gives rise to physisorptive interactions between $Pt^{\delta-}$–$O_{chem}{}^{\delta+}$ surface dipoles and H_2O dipoles. As θ_O gradually exceed the value of 0.5, the interfacial place exchange sets in giving rise to the development of chess-board-like lattice whose thickness gradually increases. It is important to add that in the case of other low-Miller index Pt surface (e.g. Pt(111) or Pt(110)) the interfacial place exchange is expected to set in at other O coverage values than 0.5 (these values remain unknown as there are no data for surface oxide growth on Pt(hkl) electrodes). Figure 2.6D: $E_{pl\text{-}exch} < E < E_{PtO/PtO2}$, where $E_{PtO/PtO2}$ refers to the onset potential of PtO_2 formation on the surface of PtO and $0.5 < \theta_O < 1$. In this potential range, the interfacial place exchange between Pt_{surf} and O_{chem} takes place (Equation 2.2) and is accompanied by the completion of charge density redistribution between Pt_{surf} and O_{chem}, and the development of a quasi-3D lattice comprising Pt^{2+} and O^{2-}.

$$Pt_{surf}{}^{\delta+} - O_{chem}{}^{\delta-} \xrightarrow{\text{interfacial place-exchange}} \left(Pt^{2+} - O^{2-}\right)_{\text{quasi-3D lattice}} \qquad (2.2)$$

Although the electronic properties of oxide layers on Pt remain unknown, they are most likely metallic-like because the oxide layer is too thin to give rise to semi-conducting properties. The quasi-3D surface lattice gives rise to physisorptive interactions between H_2O molecules and the $(Pt^{2+}$–$O^{2-})_{quasi\text{-}3D}$ species either through the H or O end of the water molecules. In addition, the O^{2-} species within the $(Pt^{2+}$–$O^{2-})_{quasi\text{-}3D}$ lattice forms a chemical bond with H_3O^+ cations initially present in the double layer; it is accompanied by interfacial charge density redistribution Figure

2.6E: $E_{\text{pl-exch}} < E < E_{\text{PtO/PtO2}}$ and $\theta_O = 1$. At this potential, the Pt surface is covered with 2 MLs of PtO comprising Pt^{2+} and O^{2-} that has a chess-board-like structure. The Pt^{2+} outer-most species can both form a chemical bond with $O_{chem}^{\delta-}$ and attract H_2O molecules through physisorptive interactions. The O^{2-} surface species can form a chemical bond with H_3O^+ and a physical bond with the H end of water molecules. Figure 2.6F: $E_{\text{pl-exch}} < E < E_{\text{PtO/PtO2}}$ and $1 < \theta_O < 1.5$. The thickness of the PtO layer increases but is less than 3 MLs of PtO. The interactions between the $(Pt^{2+}–O^{2-})_{\text{quasi-3D}}$ species and the electrolyte components are similar to those shown in Figure 2.6D. Figure 2.6G: $E_{\text{pl-exch}} < E < E_{\text{PtO/PtO2}}$ and $\theta_O = 1.5$. At this potential, the Pt surface is covered with 3 MLs of PtO comprising Pt^{2+} and O^{2-} that has a chess-board-like structure. The interactions between the $(Pt^{2+}–O^{2-})_{\text{quasi-3D}}$ species and the electrolyte components are similar to those shown in Figure 2.6D. Figure 2.6H: $E_{\text{pl-exch}} < E < E_{\text{PtO/PtO2}}$ and $1.5 < \theta_O < 2$. The thickness of the PtO layer increases but is less than 4 MLs. The interactions between the $(Pt^{2+}–O^{2-})_{\text{quasi-3D}}$ species and the electrolyte components are similar to those shown in Figure 2.6D. Although the structures presented in Figure 2.6E through Figure 2.6H give rise to similar interactions between the $(Pt^{2+}–O^{2-})_{\text{quasi-3D}}$ species and the electrolyte components, the progressively increasing thickness of PtO modifies its electronic properties and possibly the strength of these interfacial interactions. The structure of surface PtO in relation to its thickness is of great importance to the science and technology of PEMFCs because the stability of nanostructures Pt electrocatalysts impacts their performance and voltage.

2.3.4 Kinetics of Platinum Surface Oxide Growth through the Interfacial Place-Exchange Mechanism

Conway et al. [32] treated the interfacial place-exchange theoretically and derived an equation demonstrating that there is a logarithmic relation between q_{ox} and t_p ($q_{ox} \sim \log t_p$). Figure 2.7A based on Conway et al. model presents a schematic diagram of partially oxidized and partially place-exchanged Pt oxide layer (it corresponds to Figure2.6D but is simplified in order not to obscure the diagram); it also shows the interfacial potential distribution with the following components: φ_M and φ_S refer to the inner metal and inner solution (electrolyte) potentials; $\Delta\phi$ is the surface potential prior to the formation of O-containing surface species; χ_o is the surface potential due to development of $Pt^{\delta+}$–$O^{\delta-}$ dipole ($\chi_o = 0$ in the case of $\theta_O = 0$); χ_t is the time-dependent surface potential due to the place-exchanged Pt^{2+}–O^{2-} ($\chi_t = 0$ in the absence of place exchange); and $\Delta\chi_t = \chi_o - \chi_t$ is the time-dependent surface potential due to the co-existence of the $Pt^{\delta+}$–$O^{\delta-}$ surface dipole and the place-exchanged Pt^{2+}–O^{2-} quasi-3D lattice; both χ_t and $\Delta\chi_t$ are time-dependent because as the polarization time increases the surface oxidation progresses and the amounts of $Pt^{\delta+}$–$O^{\delta-}$ and Pt^{2+}–O^{2-} change giving rise to a modification of $\Delta\chi_t$. Conway et al. [32] proposed that the rate (v) of interfacial place-exchange is given by the following equation:

$$v = \frac{1}{F}\frac{dq_{ox}}{dt} = k\exp\left[-\frac{(\Delta\phi - \Delta\chi_t)2\mu_{PtO}\,\beta\,N_A}{d\,R\,T}\right] \tag{2.7}$$

where d is the monolayer oxide thickness (in m); k is the rate constant (in s^{-1}); β is the symmetry factor (it is assumed to be 0.5); N_A is the Avogadro number; F is the Faraday constant; R is the gas constant; T is the temperature; and μ_{PtO} is the dipole moment of PtO_{surf}. As stated above,

when the interfacial place-exchange proceeds the magnitude of $\Delta\chi_t$ changes and its value can be related to q_{ox} and μ_{PtO} using the following Helmholtz equation [32, 54]:

$$\Delta\chi_t = \chi_o - \chi_t = \chi_o - N_A\left(\frac{q_{ox}}{F\ \varepsilon_o\ \varepsilon_r}\right)\mu_{PtO} \tag{2.8}$$

At this stage of the discussion it is very important to add that the original equation of Conwy et al. [32] did not include ε_r. This is an important omission because the electric permittivity of the metal/oxide/electrolyte interface cannot be assumed the same as that of vacuum. Substitution of Equation 2.8 into Equation 2.7 yields the following formula for the rate of place-exchange:

$$v = \frac{1}{F}\frac{dq_{ox}}{dt} = k\exp\left[-\frac{\left(\Delta\phi - \chi_o + N_A\dfrac{q_{ox}}{F\ \varepsilon_o\ \varepsilon_r}\mu_{PtO}\right)2\mu_{PtO}\ \beta\ N_A}{d\ R\ T}\right] \tag{2.9}$$

Conway et al. assumed that χ_o has a constant value [32]. In reality, χ_o is the initial surface potential due to existence of the $Pt^{\delta+}$–$O^{\delta-}$ surface dipole, thus prior to the onset of the interfacial place exchange and the development of $(Pt^{2+}–O^{2-})_{quasi\text{-}3D}$ lattice. Consequently, the onset and progression of the interfacial place-exchange modifies the value of surface potential.

Figure 2.7 presents a revised diagram of partially oxidized and partially place-exchanged Pt oxide layer with two types of surface dipoles, namely one prior to the place-exchange and the other after the place-exchange. The charge density associated with the un-exchanged PtO is $q_{ox,1}$ and the charge density associated with the place-exchanged PtO is $q_{ox,2}$ ($q_{ox} = q_{ox,1} + q_{ox,2}$). Once the place-exchange has commenced (it can happen only when $\theta_O = 0.5$, thus when $q_{ox,1} \geq 220$ μC cm^{-2}), while at the same time the surface oxide keeps on growing, the O_{chem} "consumed" in the

place-exchange is reformed by the discharge of a water molecule. The amount of O can be given as $\theta_O = \theta_{O,1} + \theta_{O,2}$, where $\theta_{O,1}$ and $\theta_{O,2}$ correspond to $q_{ox,1}$ and $q_{ox,2}$, respectively. Thus, here it is proposed that once q_{ox} exceeds the value of 220 μC cm^{-2}, the surface coverage of "un-exchanged" PtO has a constant steady-state value of $\theta_{O,1}$ =0.5. As expected, the values of q_{ox} and $q_{ox,2}$ increase with time (here t_p) and also as E_p is raised. This reasoning leads to the following equation for the rate of interfacial place-exchange (it is an extended version of the formula proposed by Conway et al.):

$$v = \frac{1}{F}\frac{dq_{ox}}{dt} = k \exp\left[-\frac{\left(\Delta\phi - N_A \frac{q_1}{F\ \varepsilon_o\ \varepsilon_r}\mu_{PtO} + N_A \frac{q_2}{F\ \varepsilon_o\ \varepsilon_r}\mu_{PtO} \right) 2\mu_{PtO}\ \beta\ N_A}{d\ R\ T} \right] \qquad (2.10)$$

As explained elsewhere [32], $\Delta\phi$ in Equations 2.7, 2.9 and 2.10 refers to the absolute value of $\Delta\phi$ that establishes across the interface (it is related to the applied E_p). Integration of Equation 2.10 gives the following formula:

$$q_{ox} = \frac{1}{C_1} ln\left(k\ F\ C_o\ C_1\ D_1\ t_p\right) = \frac{1}{C_1} ln\left(k\ F\ C_o\ C_1\ D_1\right) + \frac{1}{C_1} ln\ t_p \qquad (2.11)$$

where C_o, C_1 and D_1 are constants that are given by the following formulae:

$$C_o = \exp\left(-\frac{2\mu_{PtO}\ \beta\ N_A\ \Delta\phi}{d\ R\ T} \right) \qquad (2.12)$$

$$C_1 = \left(\frac{2 N_A^{\,2}\, \mu_{PtO}^{\,2}\, \beta}{d\, R\, T\, F\, \varepsilon_o\, \varepsilon_r} \right) \tag{2.13}$$

$$D_1 = \exp\left(C_1\, q_{ox,1}\right) = \exp\left(\frac{2 N_A^{\,2}\, \mu_{PtO}^{\,2} \beta}{d\, R\, T\, F\, \varepsilon_o\, \varepsilon_r}\, q_{ox,1} \right) \tag{2.14}$$

According to Equation 2.11 there is a logarithmic relationship between q_{ox} and t_p (or a linear relationship between q_{ox} and ln t_p); its slope ($S_{pl\text{-}exch}$) and y-intercept ($I_{pl\text{-}exch}$) are given by the following formulae:

$$S_{pl-exch} = \frac{1}{C_1} = \frac{d\, R\, T\, F\, \varepsilon_o\, \varepsilon_r}{2 N_A^{\,2}\, \mu_{PtO}^{\,2}\, \beta} \tag{2.15}$$

$$I_{pl-exch} = \frac{1}{C_1} \ln\left(k\, F\, C_o\, C_1\, D_1\right) \tag{2.16}$$

An examination of Equation 2.15 demonstrates that experimental evaluation of $S_{pl\text{-}exch}$ could be employed to determine μ_{PtO}, provided that ε_r is known. On the other hand, the value of I cannot be easily used to determine other physical parameters of the Pt/PtO interface because Equation 2.16 contains several variable whose values care unknown.

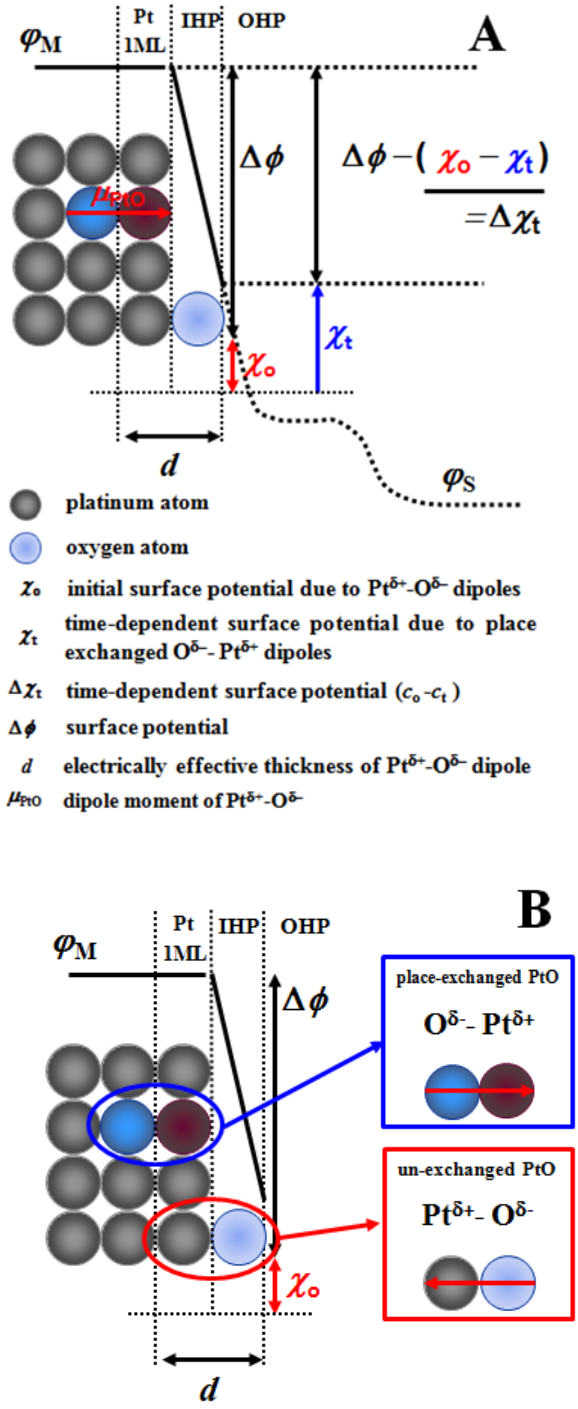

Figure 2.7. Schematic diagram of partially oxidized and partially place-exchanged Pt oxide layer (A) and revised diagram of partially oxidized and partially place-exchanged Pt oxide layer with two types of surface dipoles (B)

2.3.5 Kinetics of Platinum Surface Oxide Growth through the Metal Cation Escape Mechanism

Mott and Cabrera [34, 35] developed a theory for very thin oxides on metals whose thickness is less than X_1, (Equation 2.4) and predicted that there should be an inverse-logarithmic relation between q_{ox}^{-1} and t_p ($q_{ox}^{-1} \sim \log t_p$). In their treatment, the electric filed across the very thin oxide is so strong that the velocity of metal cation is not proportional to its electric filed (it is not a rate-determining step) and triggers an escape of metal cations from the metal into the oxide at the inner metal/oxide interface; it is the rate-determining step. This process which without the strong electric field is very unlikely to take place becomes feasible because the strong electric field lowers the activation energy barrier, as shown elsewhere [53]. The rate of escape of metal cations (here Pt^{2+}) from the metal into the oxide is expressed by the following formula [34, 35]:

$$\frac{\mathrm{d}d_{ox}}{\mathrm{d}t_p} = N\,\Omega\,\nu \exp\left(\frac{-H}{k_B\,T}\right)\exp\left(\frac{q\,a'V_{ox}}{d_{ox}\,k_B\,T}\right) \tag{2.17}$$

where N is the surface density of atoms; Ω is the volume of oxide per metal atom; ν is the vibration frequency of the surface (of the order of 10^{-12} s^{-1}); $H = H_i + U$, H_i is the enthalpy of solution of the cation in the oxide; U is the activation energy barrier for the metal cation diffusion in the oxide; V_{ox}/d_{ox} is the electric field across the oxide; a' is the distance between the metal cation and the top of the activation energy barrier ($a' = 1.72$) [6]; q is the metal cation charge; and k_B is Boltzmann constant. Integration of Equation 2.17 leads to the following relationship between $1/d$ and $\ln t_p$:

$$\frac{1}{d_{ox}} = \frac{1}{d_1}\ln\left(\frac{d_1\,u}{d_L^2}\right) + \frac{1}{d_1}\ln t_p \tag{2.18}$$

where $d_1 = qa'V/k_BT$; $u = N\Omega\nu\exp(-H/k_BT)$; and d_L is the oxide limiting thickness [34]. The meaning of d_L is such that the thickness of oxide growing according to the Mott-Cabrera mechanism cannot be greater than d_L. The slope ($S_{M\text{-}C}$) and intercept ($I_{M\text{-}C}$) of $1/d_{ox}$ versus ln t_p plots are given by the following formulae:

$$S_{M\text{-}C} = \frac{k_B T}{q\, a' V_{ox}} \tag{2.19}$$

$$I_{M\text{-}C} = \frac{1}{d_1} \ln\left(\frac{d_1\, u}{d_L^2}\right) \tag{2.20}$$

An analysis of Equation 2.19 demonstrates that experimental evaluation of $S_{M\text{-}C}$ facilitates the determination of V_{ox}. Because the oxide thickness is known, it is possible to evaluate the value of the electric field ($E_{ox} = V_{ox}/d_{ox}$). On the other hand, the value of $I_{M\text{-}C}$ cannot be used to determine other physical parameters of the PtO layer because Equation 2.20 contains several variables (e.g. Ω, u, d_L) whose values remain unknown. As we will discuss it in a subsequent section, experimental values of q_{ox} can be readily converted to values of d_{ox}.

2.3.6 Oxide Formation as a Function of Polarization Time: Plots of q_{ox} and q_{ox}^{-1} versus log t_p

The broad range of experimental conditions ($1.10 \le E_p \le 1.50$ V, $1.0 \times 10^0 \le t_p \le 1.0 \times 10^4$ s, and $278 \le T \le 333$ K) at which the growth of PtO was studied generates a comprehensive set of q_{ox} values that can be treated within the framework of the interfacial place-exchange and metal cation escape theories. Figure 2.8A through2.8D present q_{ox} versus log t_p plots for $1.10 \le$

$E_p \leq 1.50$ V and for T = 278, 293, 313, and 333 K, respectively. As expected, the values of q_{ox} increase with rising E_p and/or T. The q_{ox} versus log t_p plots are linear (R^2 = 0.991 ± 0.008) for $220 < q_{ox} < 440$ μC cm^{-2}, thus for $0.5 < \theta_O < 1$ (or for 2 ML of PtO, assuming that the oxide adopts a chess-board-like structure on Pt(100), as depicted in Figure 2.6E). When q_{ox} exceeds the value of 440 μC cm^{-2}, the q_{ox} versus log t_p plots shows a non-linear behavior that is observed for $1.30 \leq E_p \leq 1.50$ V [6].

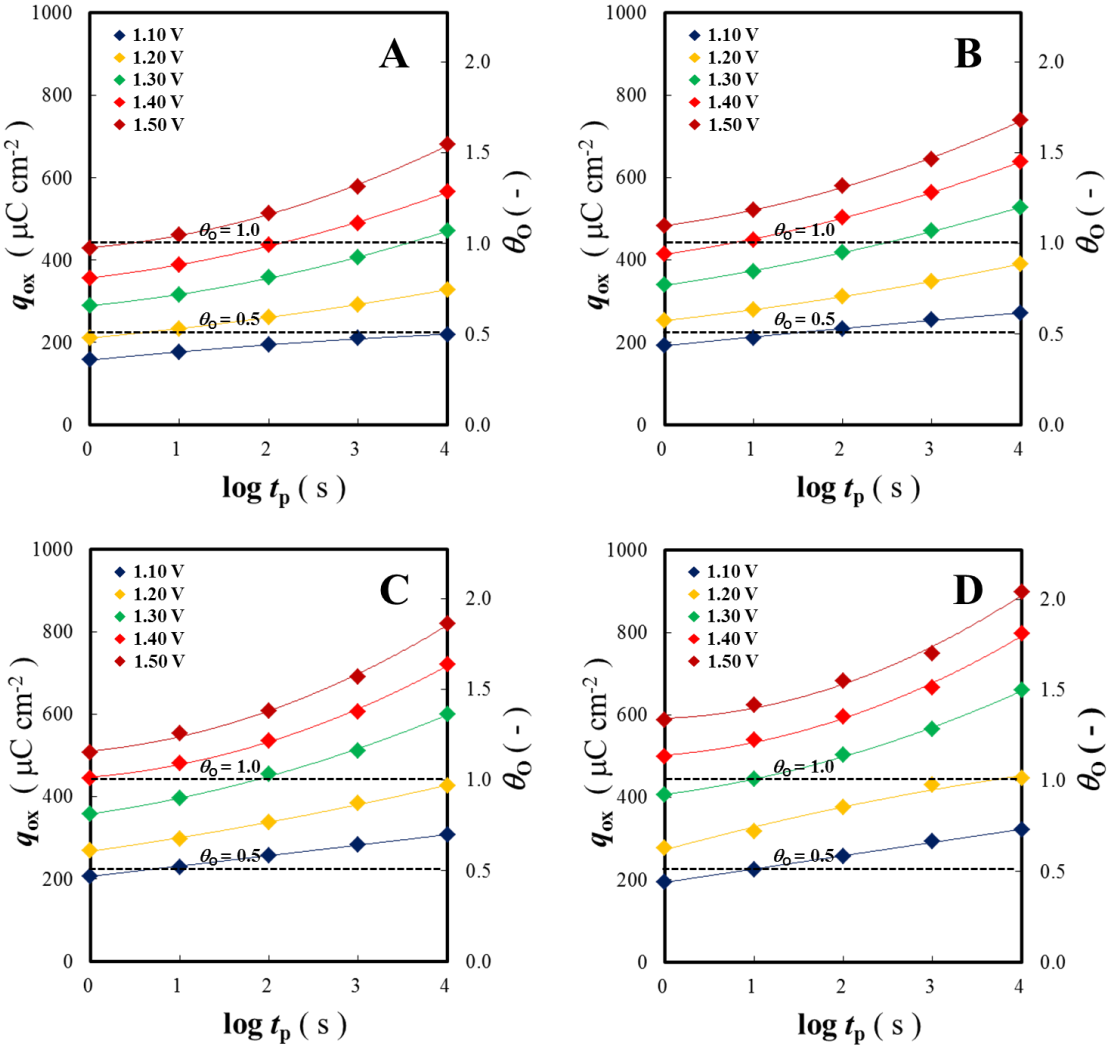

Figure 2.8. q_{ox} versus log t_p plots for $1.10 \leq E_p \leq 1.50$ V and for T = 278 (A), 293 (B), 313 (C), and 333 (D) K

Figure 2.9A through 2.9D present q_{ox}^{-1} versus log t_p plots for $1.10 \leq E_p \leq 1.50$ V and for T = 278, 293, 313, and 333 K, respectively. The results show that these plots are linear for q_{ox} > 440 μC cm^{-2} ($R^2 = 0.995 \pm 0.004$). Observation of linear q_{ox} versus log t_p and q_{ox}^{-1} versus log t_p plots points to the applicability of the kinetic laws presented in Equations 2.11 and 2.18. In addition, the results show that the oxide growth mechanism and the kinetic law change when q_{ox} reaches the value of 440 μC cm^{-2}, thus when $\theta_O = 1$. We applied the two kinetic laws in order to determine $\mu_{PtO} / \sqrt{\varepsilon_r}$ (dipole moment of PtO_{surf} divided by square route of relative dielectric constant of the oxide/electrolyte interface) and V_{ox} (potential drop across an oxide layer).

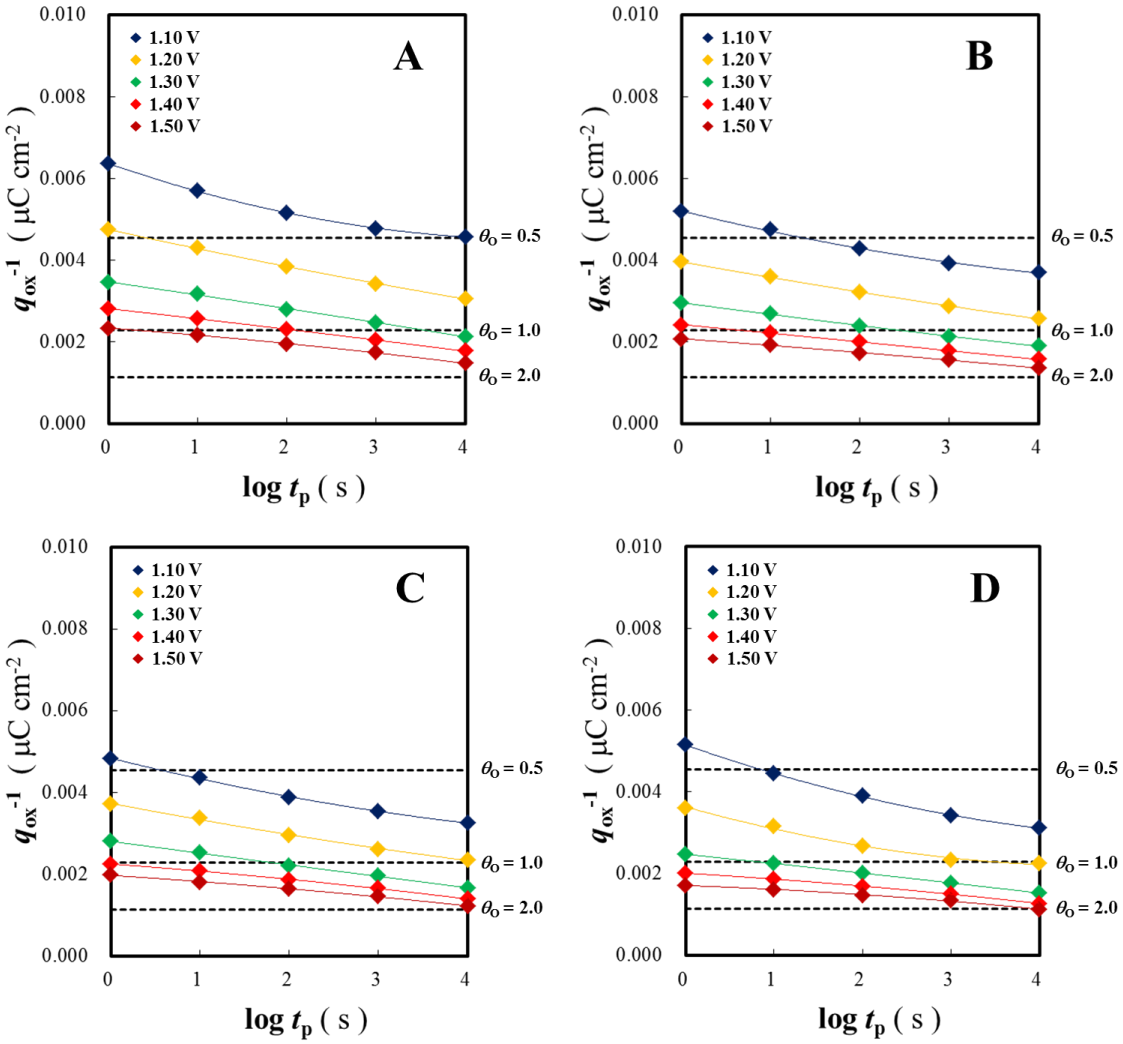

Figure 2.9. q_{ox}^{-1} versus log t_p plots for $1.10 \leq E_p \leq 1.50$ V and for T = 278 (A), 293 (B), 313 (C), and 333 (D) K

The results presented in Figure 2.10A (blue and red diamonds for E_p = 1.10 and 1.20 V, respectively) present the values of $\mu_{PtO} / \sqrt{\varepsilon_r}$ (each point is an average value for the entire oxide surface) and reveal that they are in the 1.0-1.5 D range. However, the determination of μ_{PtO} is not possible because there are no experimental data for ε_r of Pt surface oxide or the entire Pt/PtO/electrolyte interface. In Figure 2.10B, we present a plot of μ_{PtO} for E_p =1.20 V, T = 293 K and several assumed values of ε_r in the 1-30 range. As expected, they reveal a significant increase in the magnitude of μ_{PtO} with rising ε_r. The results presented in Figure 2.10A also show that for E_p = const the magnitude of $\mu_{PtO} / \sqrt{\varepsilon_r}$ decreases with an extension of E_p. This is expected because as the oxide growth continues and the place exchange commences and progresses, the place-exchanged PtO structure reduces $\Delta\chi_t$ (Equation 2.8), which translates into a reduction of μ_{PtO} through depolarization effects. The results presented in Table 2.1 demonstrate that depending on T, thus on the oxide thickness, V_{ox} is in the 0.37-1.03 V range, which translates into the strength of electric field (E_{ox}) that is consistently in the 1.00-1.90 $\times$ 10^9 V m^{-1} range. Elsewhere [51,52], we reported values of surface dipole moments for Pd and Au surface oxides. The observation that the kinetic equation developed by Conway et al. [32] neglects ε_r, suggests that in our previous papers we reported $\mu_{PtO} / \sqrt{\varepsilon_r}$ and not the values of μ_{oxide}. On the other hand the values of E_{ox} are in good agreement with the predictions of Mott and Cabrera [34,35], who stipulated that a field of the order of 10^9-10^{10} V m^{-1} is required to drive the escape of metal cations from the metal into the oxide.

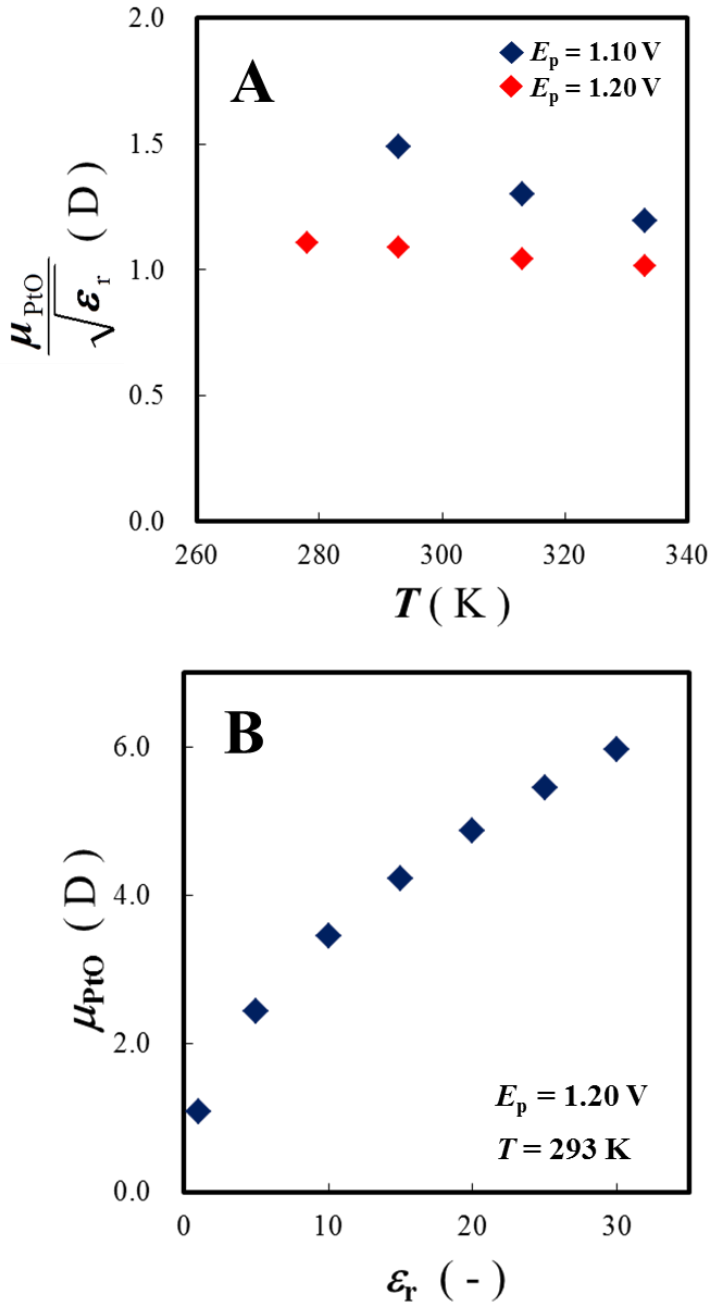

Figure 2.10. The values of $\mu_{PtO}/\varepsilon_r^{1/2}$ at $278 \leq T \leq 333$ K and E_p = 1.10 and 1.20 V (blue and red diamonds respectively). Figure 2.10B shows plots of μ_{PtO} for E_p =1.20 V, T = 293 K and several assume values of ε_r in the 1-30 range.

Table 2-1. Summary of kinetics parameters of the oxide growth derived from the application of Mott-Cabrera theory

T [K]	V_{ox} [V]	d_{ox} [nm]	E_{ox} [$\times 10^{-9}$ V m^{-1}]
278	0.372-0.580	0.226-0.532	1.00-1.72
293	0.496-0.732	0.266-0.578	1.20-1.94
313	0.497-0.756	0.280-0.642	1.06-1.90
333	0.632-1.034	0.318-0.704	1.22-1.55

Although the value of ε_r for PtO residing on the surface of Pt and in direct contact with an electric double layer is unknown, it is interesting to assess the magnitude of dipole-dipole interactions as a function of their separation. The potential energy of two identical and parallel dipoles ($V_{p(d-d)}$) separated by a distance r is given by the following equation:

$$V_{p(d-d)} = \frac{\mu^2}{4\varepsilon_o\ \varepsilon_r\ r^3} \tag{2.21}$$

Although the value of ε_r is unknown, we may analyze the value of $\varepsilon_r V_{p(d-d)}$ as a function of r, assuming it equals 1, 2, 3, and 4 diameters of Pt atom (D_{Pt} = 278 pm). A very simple analysis of Equation 2.21 reveals that as r increases from $1D_{Pt}$ to $4D_{Pt}$ with an interval of $1D_{Pt}$, the potential energy of repulsive interactions decreases by a factor of 8, 27, and 64, respectively. Clearly, the closest approach ($r = D_{Pt}$) of two identical and parallel dipoles creates such strong repulsive interactions that they adopt spontaneously an anti-parallel arrangement. In the case of O_{chem} residing on Pt_{surf} (the $Pt^{\delta+}$–$O^{\delta-}$ surface dipole) these repulsive interactions give rise to the interfacial place exchange whose existence was proven experimentally [31]. This discussion calls for a detailed modelling of the PtO/Pt/electrolyte interphase, but such a theoretical analysis is

outside the scope of our expertise. However, we hope that it will stimulate the interest of theoreticians working in this area.

2.3.7 Influence of Anion on the Interfacial place exchange

Anions are important components of the electric double layer and affect its interfacial structure and electronic properties. They are known to chemisorb (specifically adsorb) in the potential range of double layer charging and their surface coverage abruptly decreases to zero as surface oxide formation commences [55]. Figure 2.11 presents experimentally determined values of θ_O as a function of log t_p for $1.10 \leq E_p \leq 1.50$ V and $T = 293$ K in two aqueous electrolytes, namely CF_3SO_3H (blue diamonds) and H_2SO_4 (red diamonds). The results reveal that for $1.10 \leq E_p \leq 1.20$ V and $1.0 \times 10^0 \leq t_p \leq 1.0 \times 10^4$ s, the values of θ_O are practically the same within the experimental uncertainty. Because under these conditions the oxide growth is limited by the interfacial place-exchange, the results suggest that either these two anions have the same effect on the oxide growth or the anion nature has no perceivable impact on the oxide growth kinetics. On the other hand, the results demonstrate that for $1.30 \leq E_p \leq 1.50$ V and $1.0 \times 10^2 \leq t_p \leq 1.0 \times 10^4$ s the values of θ_O are slightly but consistently higher in CF_3SO_3H than in H_2SO_4. In addition, the respective difference rises with increasing t_p. These results are surprising and even seem counterintuitive because if the anion were to impact the oxide growth behavior, then one would expect their effect to be operational in the low potential range, thus in the potential range at which the anion desorbs while the oxide growth commences. The results presented here, which to the best of our knowledge constitute the first comparative analysis of the Pt surface oxide growth in two different electrolytes, reveal a new qualitative behavior suggesting that although the anion is

desorbed, it still impacts the oxide growth kinetics by indirectly affecting the electric field within the double layer and also possibly within the surface oxide.

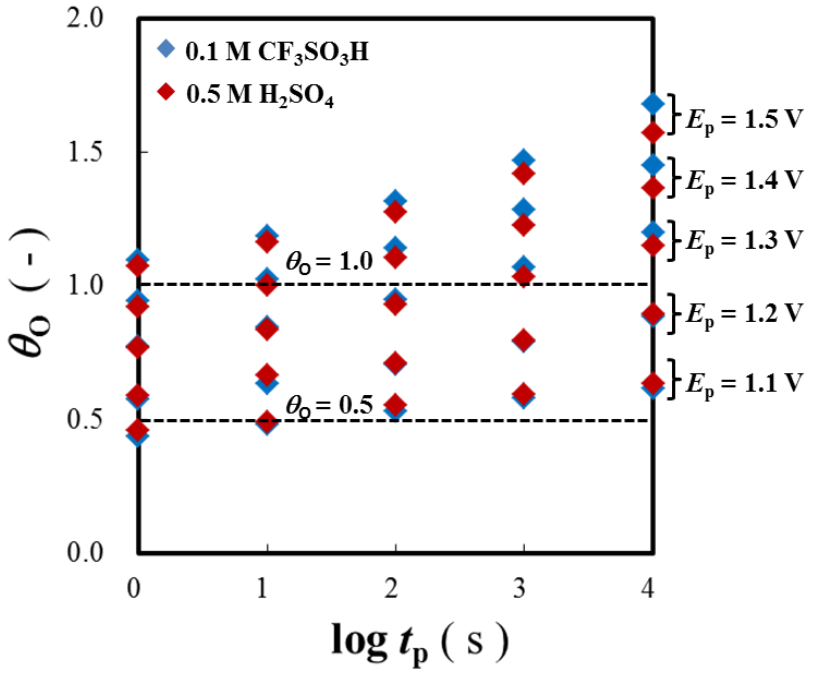

Figure 2.11. Experimentally determined values of θ_O as a function of log t_p for $1.10 \leq E_p \leq 1.50$ V and T = 293 K in in 0.1 M aqueous CF_3SO_3H (blue diamonds) and 0.5 M aqueous H_2SO_4 (red diamonds).

2.4 Conclusions

Because CF_3SO_3H is the smallest fluorinated sulfonic acid that mimics the basic anion-platinum interactions occurring in membrane electrode assemblies of fuel cells, the surface oxide on polycrystalline Pt electrode was studied in 0.1 M aqueous CF_3SO_3H at $1.10 \leq E_p \leq 1.50$ V for $1.0 \times 10^0 \leq t_p \leq 1.0 \times 10^4$ s and at $278 \leq T \leq 333$ K. The amount of surface oxide was determined by recording CV oxide-reduction profiles followed by their integration that yielded the oxide charge density (q_{ox}) values. The results were compared to those obtained in aqueous H_2SO_4 solution with the objective of identifying and quantifying the influence of the anion nature on the process. The critical thicknesses (X_1), which determines the applicability of oxide growth theories, is determined to be $7.2 \leq X_1 \leq 29$ nm, depending on E_p and T. It is related to the experimental values of d_{ox} (q_{ox} is converted to d_{ox}). Because for the entire range of E_p, t_p and T values $d_{ox} < X_1$, the Pt surface oxide growth is expected to follow the interfacial place-exchange (Conway et al. [32]) or the metal cation escape mechanism (Mott and Cabrera). The mechanism of surface oxide growth on Pt electrodes is revised and expanded by taking into account the possible interactions of hydronium cations, anions, and water molecules with the Pt surface prior to and during various stages of its electro-oxidation. The kinetic equation describing the rate of interfacial place exchange originating from repulsive interactions between $Pt^{\delta+}$–$O^{\delta-}$ surface dipoles is modified and expanded by taking into time-dependent variation of the surface potential. In addition, the relative dielectric constant of the metal/oxide/electrolyte interface is included in the kinetic equation (it was neglected in the original treatment of Conway et al. [32]). The experimental values of q_{ox} for given E_p = const and T = const are plotted as q_{ox} versus log t_p or as q_{ox}^{-1} versus log t_p, with the objective of identifying the applicability of logarithmic (Equation 2.11) and inverse-logarithmic (Equation 2.18) oxide growth kinetics. The logarithmic law is applicable in the

case of $0.5 \leq \theta_O \leq 1.0$ indicating that the interfacial place exchange between the surface Pt atoms (Pt_{surf}) and the chemisorbed O atoms (O_{chem}) is the rate determining step. The inverse-logarithmic law is applicable in the case of $1.0 \leq \theta_O \leq 2.0$ suggesting that the escape of metal cation (Pt^{2+}) from the metal into the oxide is the rate determining step. The anion present in the electrolyte interacts with the Pt electrode prior to the onset of oxide formation through chemisorption (specific adsorption) and desorbs as the oxide formation commences. Thus, it is expected to impact the oxide growth behavior especially in the very initial stages of its formation. A comparison of the results obtained in the CF_3SO_3H and H_2SO_4 solutions demonstrates that the values of q_{ox} are practically the same for $0.5 \leq \theta_O \leq 1.0$ suggesting that either both anions have the same interactions with the platinum electrode or that the anions have no impact on the oxide growth behavior in this θ_O range. On the other hand, the values of q_{ox} for $1.0 \leq \theta_O \leq 2.0$ are higher for the CF_3SO_3H solution than for the H_2SO_4 solution. These unexpected results suggest that the desorbed anion impacts the oxide growth kinetics by indirectly affecting the electric field within the double layer and within the surface oxide.

2.5 References

(1) A. Ohma, T. Mashio, K. Sato, H. Iden, Y. Ono, K. Sakai, K. Akizuki, S. Takaichi, and K. Shinohara, Electrochim. Acta **56**, 10832 (2011).

(2) D. Papageorgopoulos, 2013 Fuel Cells Annual Merit Review (U.S. Department of Energy, Arlington, Virginia, 2013).

(3) A. Kongkanand and J. M. Ziegelbauer, J. Phys. Chem. C **116**, 3684 (2012).

(4) S. Sugawara, Y. Suzuki, S. Kocha and K. Shinohara, Electrochemistry, **79**, 404 (2011).

(5) Y. Liu, M. Mathias, J. Zhang, Electrochem. Solid-State Lett. **13**, B1 (2010).

(6) M. Alsabet, M. Grden, and G. Jerkiewicz, J. Electroanal. Chem. **589**, 120 (2006).

(7) N. M. Markovic, H. A. Gasteiger, B. N. Grgur, and P. N. Ross, J. Electroanal. Chem. **467**, 157 (1999).

(8) N. P. Subramanian, T. A. Greszler, J. Zhang, W. Gu, and R. Makharia, J. Electrochem. Soc. **159**, B531 (2012).

(9) K. Kodama, R. Jinnouchi, T. Suzuki, T. Hatanaka, and Y. Morimoto, Electrochim. Acta **78**, 592 (2012).

(10) I. E. L. Stephens, A. S. Bondarenko, F. J. Perez-Alonso, F. Calle-Vallejo, L. Bech, T. P. Johansson, A. K. Jepsen, R. Frydendal, B. P. Knudsen, J. Rossmeisl, and I. Chorkendorf, J. Am. Chem. Soc. **133**, 5485 (2011).

(11) R. M. Darling, and J. P. Meyers, J. Electrochem. Soc. **150**, A1523 (2003).

(12) R. M. Darling, and J. P. Meyers, J. Electrochem. Soc. **152**, A242 (2005).

(13) A. A. Franco, and M. Tembely, J. Electrochem. Soc. **157**, B712 (2007).

(14) L. Tang, B. Han, K. Persson, C. Friesen, T. He, K. Sieradzki, and G. Cede, J. Am. Chem. Soc. **132**, 596 (2010).

(15) M. Uchimura, and S. Kocha, ECS Trans. **11**, 1215 (2007).

(16) X. Wang, R. Kumar, and D. J. Myers, Electrochem. Solid-State Lett. **9**, A225 (2006).

(17) R. Jinnouchi, E. Toyoda, T. Hatanaka, and Y. Morimoto, J. Phys. Chem. C **114**, 17557 (2010).

(18) L.Xing, M. A. Hossain, M. Tian, D. Beauchemin, K. T. Adjemian, and G. Jerkiewicz, Electrocatalysis **5**, 96 (2014).

(19) A. Topalov, I. Katsounaros, M. Auinger, S. Cherevko, J. C. Meier, S. Klemm, and K. J. J. Mayrhofer, Angew. Chem. Int. Ed. **51**, 12613 (2012).

(20) Y. Sugawara, T. Okayasu, A. P. Yadav, and A. Nishikata, J. Electrochem. Soc. **159**, F779 (2012).

(21) D. Gilroy, and B. E. Conway, Can. J. Chem. **46**, 875 (1968).

(22) K. J. Vetter, and J. W. Schultze, J. Electroanal. Chem. **34**, 141 (1972).

(23) B. V. Tilak, B. E. Conway, and H. Angerstein-Kozlowska, J. Electroanal. Chem. **48**, 1 (1973).

(24) H. Angerstein-Kozlowska, B. E. Conway, and W. B. A. Sharp, J. Electroanal. Chem. **43**, 9 (1973).

(25) G. Jerkiewicz, G. Tremiliosi-Filho, and B. E. Conway, J. Electroanal. Chem. **334**, 359 (1992).

(26) A. Sun, J. Franc, and D. D. Macdonald, J. Electrochem. Soc. **153**, B260 (2006).

(27) H. Imai, K. Izumi, M. Matsumoto, Y. Kubo, and K. Kato, J. Am. Chem. Soc. **131**, 6293 (2009).

(28) L. R. Merte, F. Behafarid, D. J. Miller, D. Friebel, S. Cho, F. Mbuga, D. Sokaras, R. Alonso-Mori, T. Weng, D. Nordlund, A. Nilsson, and B. R. Cuenya, ACS Catal. **2**, 2371 (2012).

(29) V. I. Birss, M. Chang, and J. Segal, J. Electroanal. Chem. **355**, 181 (1993).

(30) D. A. Harrington, J. Electroanal. Chem. **420**, 101 (1997).

(31) G. Jerkiewicz, G. Vatankhah, J. Lessard, M. Soriaga, and Y.-S. Park, Electrochim. Acta **49**, 1451 (2004).

(32) B. E. Conway, B. Barnett, H. Angerstein-Kozlowska, and B. V. Tilak, J. Chem. Phys. **93**, 8361 (1990).

(33) G. Vatankhah, J. Lessard, G. Jerkiewicz, A. Zolfaghari, and B. E. Conway, Electrochim. Acta **46**, 1613 (2003).

(34) N. Cabrera, and N. F. Mott, Rep. Prog. Phys. **12**, 163 (1948).

(35) N. F. Mott, J. Chim. Phys. **44**, 172 (1949).

(36) A. Ohma, K. Fushinobu, and K. Okazaki, Electrochim. Acta **55**, 8829 (2010).

(37) A. Kabasawa, H. Uchida, and M. Watanabe, Electrochem. Solid-State Lett. **11**, B190 (2008).

(38) R. Subbaraman, D. Strmcnik, A. P. Paulikas, V. R. Stamenkovic, and N. M. Markovic, ChemPhysChem. **11**, 2825 (2010).

(39) R. Subbaraman, D. Strmcnik, V. Stamenkovic, and N. M. Markovic, J. Phys. Chem. C **114**, 8414 (2010).

(40) A. M. Gomez-Marin, A. Berna, and J. M. Feliu, J. Phys. Chem. C **114**, 20130 (2010).

(41) H. Angerstein-Kozlowska, B. E. Conway, B. Barnett, and J. Mozota, J. Electroanal. Chem. **100**, 417 (1979).

(42) B. E. Conway, Prog. Surf. Sci. **49**, 331 (1995).

(43) M. Teliska, V. Murthi, S. Mukerjee, and D. E. Ramaker, J. Phys. Chem. C **111**, 9267 (2007).

(44) P. Zelenay, M. A. Habib, and J. O. Bockris, J. Electrochem. Soc. **131**, 2464 (1984).

(45) G. Jerkiewicz, M. Alsabet, M. Grden, H. Varela, and G. Tremiliosi-Filho, J. Electroanal. Chem. **625**, 172 (2009).

(46) D. Chen, Q. Tao, L.W. Liao, S.X. Liu, Y.X. Chen, and S. Ye, Electrocatalysis **2**, 207 (2011).

(47) B. E. Conway, H. Angerstein-Kozlowska, W. A. Sharp, and E. E. Criddle, Anal. Chem. **45**, 1331 (1973).

(48) G. Tremiliosi-Filho, G. Jerkiewicz, and B. E. Conway, Langmuir **8**, 658 (1992).

(49) A. Zolfaghari, and G. Jerkiewicz, J. Electroanal. Chem. **467**, 177 (1999).

(50) A. Zolfaghari, M. Chayer, and G. Jerkiewicz, J. Electrochem. Soc. **144**, 3034 (1997).

(51) G. Tremiliosi-Filho, L. H. Dall'Antonia, and G. Jerkiewicz, J. Electroanal. Chem. **578**, 1 (2005).

(52) L. H. D. Antonia, G. Tremiliosi-Filho, and G. Jerkiewicz, J. Electroanal. Chem. **502**, 72 (2001).

(53) G. Jerkiewicz, and J. J. Borodzinski, Langmuir **9**, 2202 (1993).

(54) B. E. Conway, Prog. Surf. Sci. **16**, 1 (1984).

(55) M. Gamboa-Aldeco, E. Herrero, P. Zelenay, and A. Wieckowski, J. Electroanal. Chem. **348**, 451 (1993).

Chapter 3

Thermodynamics of the Under-Potential Deposition of Hydrogen on Polycrystalline Platinum in Aqueous Trifluoromethanesulfonic Acid

3.1 Introduction

Polymer electrolyte membrane fuel cells (PEMFCs) are promising primary power sources for personal vehicles. There remain important technological issues that need to be addressed prior to the commercialization of fuel cell electric vehicles (FCEVs), such as cost reduction, increase of power density, and improvement of durability; the cost reduction is the most challenging issue. The membrane electrode assembly (MEA) in PEMFCs is composed of a polymer electrolyte membrane acting as a proton conductor, catalyst layers (CLs) as electrodes (anode, cathode), and gas diffusion layers (GDL). CLs are among the most expensive components of PEMFCs due to the use of precious platinum (Pt) [1,2]; thus, they offer a great opportunity for cost reduction. The CLs consist of Pt nano-particles (Pt-NPs) residing on carbon support and covered with ionomer (e.g. Nafion®); they function as electrodes for oxygen reduction reaction (ORR) and hydrogen oxidation reaction (HOR). Due to the importance of Nafion®, which plays the role of electrolyte and separator, it is of great importance to understand the Pt-electrolyte interfacial behavior because it affects the effectiveness of Pt utilization.

The electro-adsorption of H, often referred to as under-potential deposition of H (UPD H), on noble metal electrodes is one of the most extensively studied interfacial electrochemical processes [3-15]. The electro-adsorption of under-potential deposited H (H_{UPD}) takes place at

potentials positive with respect to the thermodynamic reversible potential of the hydrogen evolution reaction (HER) and is known to occur only on Pt-group metals [9]. In acidic aqueous media, H_{UPD} on the Pt surface is generated by the discharge of hydronium cation according to the following reaction (Equation 3.1):

$$Pt + H_3O^+(aq) + e^- \rightarrow Pt-H_{UPD} + H_2O \quad (3.1)$$

The number of electrons transferred in the process is 1, thus $H_3O^+(aq)$ undergoes complete discharge. However, upon the $Pt-H_{UPD}$ bond formation the charge density might be "asymmetrical" (charge density shift) giving rise to a dipole-like nature of the bond. Thermodynamic analysis of UPD H on polycrystalline and monocrystalline Pt electrodes was examined by several researchers [3-4,10-15].

Thermodynamic parameters, such as Gibbs energy, enthalpy, entropy of electro-adsorption, and the substrate-hydrogen bond energy were determined by employing electrochemical adsorption isotherms. The general electro-adsorption isotherm is given by Equation 3.2 [7]:

$$\frac{\theta_{H_{UPD}}}{1-\theta_{H_{UPD}}} = a_{H_3O^+} \exp\left(\frac{-E_{SHE}\,F}{R\,T}\right)\exp\left(\frac{-\Delta_{ec-ads}G°(H_{UPD})}{R\,T}\right) \quad (3.2)$$

where $\theta_{H_{UPD}}$ is the surface coverage of H_{UPD} on the Pt surface; $a_{H_3O^+}$ is the activity of H_3O^+; E_{SHE} is the electrode potential measured versus the standard hydrogen electrode (SHE); $\Delta_{ec-ads}G°(H_{UPD})$ is the standard Gibbs energy of elector-adsorption; F is the Faraday constant;

R is the gas constant; and *T* is temperature. The electro-adsorption and electro-desorption of H_{UPD} on the Pt surface is reversible at any given potential and the number of H_{UPD} on Pt surface does not exceed a monolayer coverage.

Recently Huang et al. [15] investigated for the first time the thermodynamics of H_{UPD} electro-adsorption on carbon-supported Pt-NPs with Nafion® ionomer in actual CLs [15]. The outcome is of great importance for the fuel cell technology because it demonstrates the applicability of "research laboratory" experimental and theoretical approaches to actual technological systems and reports difference in the thermodynamics parameters of UPD H for Pt/C and Pt alloy/C electrocatalysts in actual CLs. However, the use of CLs poses several unavoidable limitations, the main being the occurrence of HER and HOR that generate large cathodic and anodic feature in cyclic-voltammetry profiles making the analysis of UPD H difficult. Thus, the simplest possible electrochemical setup is ideal for the examination of UPD H and the determination of thermodynamic state functions of the process in relation to the electrode nature and the electrolyte composition.

Trifluoromethanesulfonic acid (CF_3SO_3H) is the smallest fluorinated sulfonic acid and can serve as a suitable molecular model mimicking the Nafion® ionomer in CLs. It was demonstrated that the strength of anion adsorption on the Pt surface in CF_3SO_3H is weaker than that in H_2SO_4; the anion (sulfonic acid group) originating from the Nafion® ionomer interacts weakly with the Pt surface [16-19]. Thus, CF_3SO_3H is an ideal compound to examine the influence of the Pt-anion interactions on the interfacial behavior of Pt in the potential ranges of UPD H and oxide formation and reduction [20-21].

In this chapter, we report on the influence of temperature on UPD H on polycrystalline Pt in aqueous CF_3SO_3H solution examined using cyclic-voltammetry. We employ the general electrochemical adsorption isotherm to determine the Gibbs energy ($\Delta_{ec-ads}G°(H_{UPD})$), enthalpy ($\Delta_{ec-ads}H°(H_{UPD})$), entropy ($\Delta_{ec-ads}S°(H_{UPD})$) of H_{UPD} electro-adsorption, and the Pt–H_{UPD} surface bond energy ($E_{Pt-H_{UPD}}$). We also report on the nature of lateral interactions between the H_{UPD} adatoms. The data obtained in the aqueous CF_3SO_3H solution are compared to analogous results obtained in H_2SO_4 and $HClO_4$ aqueous solutions with the objective of identifying and quantifying the influence of the anion nature on thermodynamics of the process. To the best of our knowledge, this is the first thermodynamic analysis of UPD H on polycrystalline Pt in an aqueous CF_3SO_3H solution.

3.2 Experimental

3.2.1 Electrode Preparation

The polycrystalline Pt working electrode (WE) was prepared from ultra-high purity wire (99.999% in purity, and 0.5 mm in diameter). The details of the procedure employed are described elsewhere [22]. The electrode was degreased in acetone under reflux followed by rinsing with ultra-high purity ethanol. Then, it was cleaned in concentrated H_2SO_4 for 24 hours and rinsed several times (at least ten times) with ultra-high purity water (MilliPore, Milli-Q3; $\rho \geq$ 18.2 MΩ cm). The counter electrode was a Pt mesh (99.999% in purity) connected to Pt wire (99.999% in purity, and 0.5 mm in diameter) that was sealed in a glass tube. The reference electrode was Pt/Pt black placed in the same electrolyte but in a separate compartment through

which H_2 (p_{H2} = 1 atm) was passed. It served as a reversible hydrogen electrode (RHE). The RHE compartment was electrolytically connected to the WE compartment by means of a Luggin capillary. All potentials measured experimentally and referred to in this paper are expressed with respect to RHE.

3.2.2 Electrolyte and Electrochemical Cell

Cyclic-voltammetry profiles for H_{UPD} electro-adsorption on Pt electrode were acquired in the 278–333 K temperature range (T = 278, 293, 313 and 333 K) at a potential scan rate of s = 50 mV s^{-1}. The charge associated with UPD H ($Q_{\mathrm{UPD\,H}}$) was determined by integrating the anodic cyclic-voltammetry (CV) profile in the 0.05–0.40 V range, allowing for the double layer charging. By using the anodic component of the CV profile, we were able to eliminate any uncertainty due to the onset of HER that is visible in the cathodic component of CV profile [6]. The electrochemically active surface area (A_{ecsa}) of the Pt electrode was determined by dividing $Q_{\mathrm{UPD\,H}}$ by the charge density required to form a monolayer of H_{UPD}, thus by $q_{1\mathrm{ML\,H_{UPD}}}$ = 220 μC cm^{-2} [24]. The value of $\theta_{\mathrm{H_{UPD}}}$ at a given potential was determined by dividing the charge density associated with electro-adsorption of H_{UPD} ($q_{\mathrm{UPD\,H}}$) by $q_{1\mathrm{ML\,H_{UPD}}}$ ($\theta_{\mathrm{H_{UPD}}} = q_{\mathrm{UPD\,H}} / q_{1\mathrm{ML\,H_{UPD}}}$). A standard, all-glass two-compartment electrochemical cell was employed in all measurements [25]. It was immersed in a water bath, the temperature of which was monitored and controlled to within 1 K. The electrolyte level in the cell was maintained below the water level in the bath to provide uniform temperature distribution. A Bio Logic Model SP-150 potentiostat controlled with proprietary software was used to conduct the CV

3.3 Results and Discussion

3.3.1 Temperature Dependence of UPD H in Different Electrolytes

Figure 3.1 presents three CV profiles for the Pt polycrystalline electrode in 0.1 M aqueous CF_3SO_3H (blue line), 0.5 M aqueous H_2SO_4 (red line), and 0.1 M aqueous $HClO_4$ (green line) obtained at s = 50 mV s^{-1} and T = 293 K. In the 0.05–0.40 V range, the CV transients reveal the usual features corresponding to the electro-adsorption and electro-desorption of H_{UPD}; they are symmetric with respect to the potential axis indicating that UPD H is reversible in the sense that at a given potential the H_{UPD} coverage is constant; it can be increased or decreased only by modifying the potential and holding the potential at a fixed value does not alter the coverage of H_{UPD}. The electro-adsorption of H_{UPD} in the CF_3SO_3H solution starts a potential that is about 40 mV higher than that in the H_2SO_4 solution, but about 20 mV lower than that in the $HClO_4$ solution. The CV peaks in the CF_3SO_3H and $HClO_4$ solutions have lower current density (j) values (are slightly less pronounced) than in the H_2SO_4 solution; these variances are attributed to different strengths of anion interactions with Pt

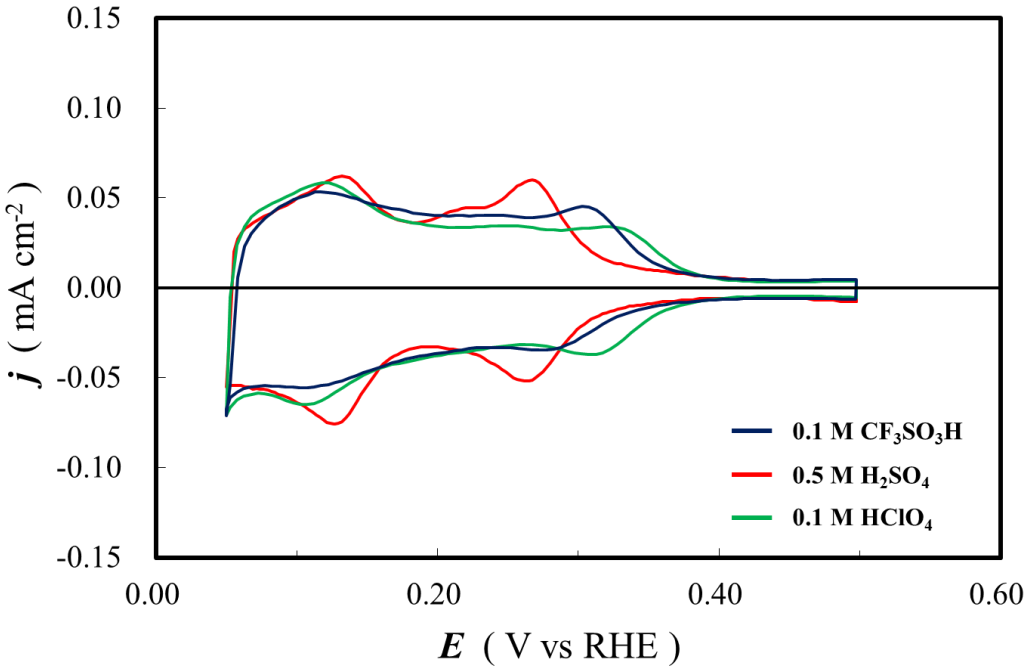

Figure 3.1. CV profiles for the Pt polycrystalline electrode in 0.1 M aqueous CF_3SO_3H (blue line), 0.5 M aqueous H_2SO_4 (red line), and 0.1 M aqueous $HClO_4$ (green line) obtained at s = 50 mV s^{-1} and T = 293 K.

Figure 3.2 presents three graphs: **A** for CF_3SO_3OH; **B** for H_2SO_4; and **C** for $HClO_4$. Each graphs contains four CV profiles corresponding to electro-adsorption and electro-desorption of H_{UPD} at a different temperature, namely T = 278, 293, 313, and 333K. The CV profiles reveal that the peaks shift towards lower potentials as T is raised; the magnitude of the shift is ca. 20 mV for the overall temperature rise of 55 K. There are no other CV features that could be assigned to the temperature rise. Apart from the shift, the profiles are symmetric with respect to the potential axis; the peak potentials of H_{UPD} adsorption in each electrolyte are almost consistent with the peak potentials of H_{UPD} desorption. It is indicated that the experimental setup remains clean as T is raised.

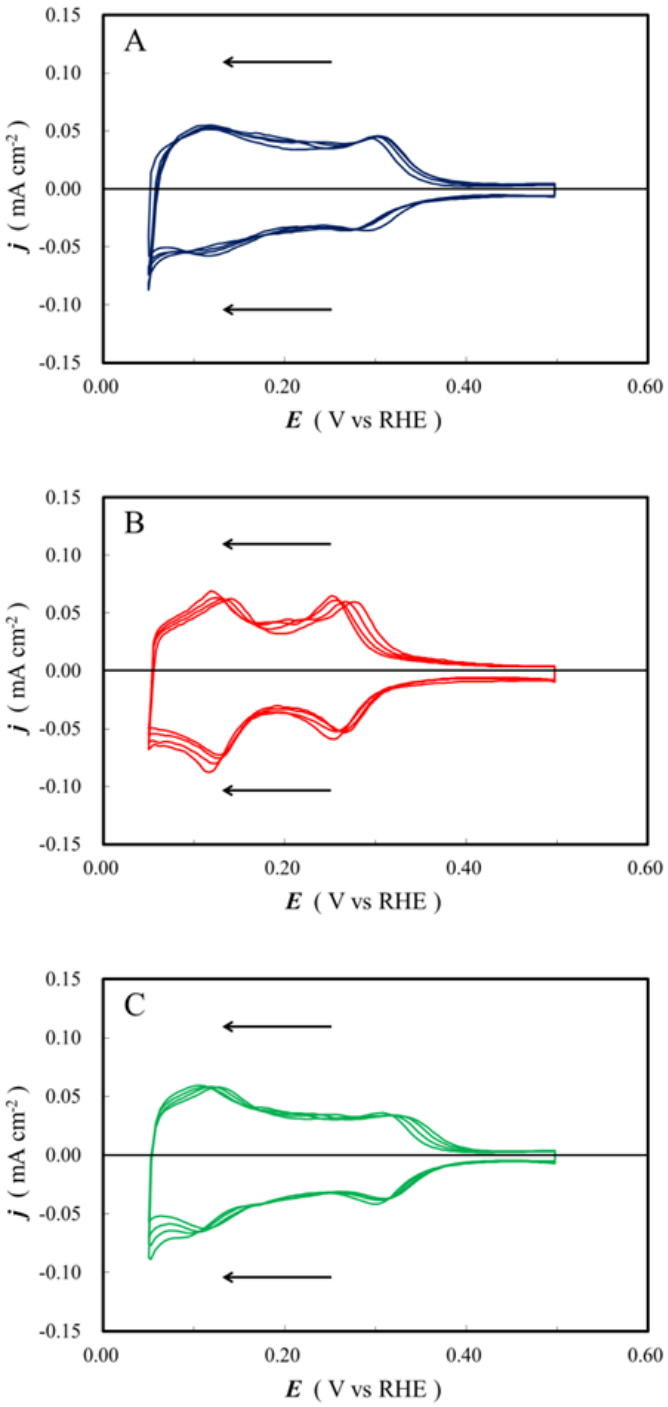

Figure 3.2. Four CV profiles corresponding to electro-adsorption and electro-desorption of H_{UPD} at a different temperature, namely T = 278, 293, 313, and 333K in CF_3SO_3H (graph A), in H_2SO_4 (graph B); and $HClO_4$ (graph C).

3.3.2 Analysis of Thermodynamics of UPD H in Different Electrolytes

The determination of the values of thermodynamic parameters for UPD H, $\Delta_{ec-ads}G°(H_{UPD})$ as a function of $\theta_{H_{UPD}}$ and *T*, and the determination of $\Delta_{ec-ads}H°(H_{UPD})$ and $\Delta_{ec-ads}S°(H_{UPD})$ in relation to $\theta_{H_{UPD}}$, is required for the subsequent evaluation of the energy of later interactions ($\omega_{H_{UPD}}$) and the Pt–H_{UPD} surface bond energy ($E_{Pt-H_{UPD}}$) [9]. In the case of *T* = const, any variation of $\Delta_{ec-ads}G°(H_{UPD})$ with $\theta_{H_{UPD}}$ points to the existence of lateral interactions that can be either attractive ($\omega_{H_{UPD}} < 0$) or repulsive ($\omega_{H_{UPD}} > 0$) in nature. In addition, the relationship between $\Delta_{ec-ads}G°(H_{UPD})$ and $\theta_{H_{UPD}}$ (for *T* = const) allows us to assess whether UPD H follows any of the main electro-adsorption isotherms (i.e. Langmuir, Frumkin, Temkin) [9]. Because experimental data were acquired in three different electrolytes, the set of data allows us to assess whether the electrolyte nature has any major impact on the thermodynamics of UPD H.

Elsewhere [6-9], it was explained that the *general electrochemical isotherm* may be presented using either Equation 3.2 or the following formula:

$$\frac{\theta_{H_{UPD}}}{1-\theta_{H_{UPD}}} = \sqrt{f_{H_2}}\ \exp\left(\frac{-E_{RHE}\,F}{R\,T}\right)\exp\left(\frac{-\Delta_{ec-ads}G°(H_{UPD})}{R\,T}\right) \qquad (3.3)$$

where f_{H_2} is the fugacity of H_2(g) in the reference compartment and E_{RHE} is the potential measured with respect to a reversible hydrogen electrode (RHE). There is a slight yet very important difference between Equations 3.2 and 3.3. Specifically, the potential scales are different and Equation 3.2 contains the activity of hydrated proton, while Equation 3.3 contains

the fugacity of H_2(g) [9]. Both formulae may be applied to determine $\Delta_{ec-ads}G°(H_{UPD})$ but the application of Equation 3.3 is more straightforward provided that RHE is employed [7]. It should be noted that the value of $\Delta_{ec-ads}G°(H_{UPD})$ for a given $\theta_{H_{UPD}}$ ($\theta_{H_{UPD}}$ is related to *E*) at *T* = const includes the energy of lateral interactions, thus $\Delta_{ec-ads}G°(H_{UPD})_{\theta_{H_{UPD}}=0} \neq \Delta_{ec-ads}G°(H_{UPD})_{\theta_{H_{UPD}}\neq 0}$.

We applied Equation 3.3 in order to determine $\Delta_{ec-ads}G°(H_{UPD})$ for the four temperatures employed in the course of research and for several values of $\theta_{H_{UPD}}$ in the 0.10–0.90 range with an interval of 0.05. We do not report $\Delta_{ec-ads}G°(H_{UPD})$ values for $\theta_{H_{UPD}}$ < 0.10 and for $\theta_{H_{UPD}}$ > 0.90 because of large experimental uncertainties (the determination of *Q* corresponding to $\theta_{H_{UPD}}$ = 0.05 or 0.95 carries a significant uncertainty because the value of *Q* is small compared to the value of charge associated with double layer charging).

Figure 3.3 shows $\Delta_{ec-ads}G°(H_{UPD})$ versus $\theta_{H_{UPD}}$ plots for *T* = 278, 293, 313, and 333 K for CF_3SO_3H (graph A), H_2SO_4 (graph B), and $HClO_4$ (graph C). The results reveal very similar trends that may be summarized as follows: (i) in all cases $\Delta_{ec-ads}G°(H_{UPD})$ increases towards less-negative values with increase in $\theta_{H_{UPD}}$ irrespective of the temperature; (ii) in all cases $\Delta_{ec-ads}G°(H_{UPD})$ adopts values from –13 to –27 kJ mol^{-1}; (iii) $\Delta_{ec-ads}G°(H_{UPD})$ changes approximately linearly in the $0.3 \leq \theta_{H_{UPD}} \leq 0.7$ range suggesting that the process follows a Temkin electro-adsorption isotherm; (iv) $\Delta_{ec-ads}G°(H_{UPD})$ adopts less-negative values as $\theta_{H_{UPD}}$ increases, thus the lateral interactions between H_{UPD} adatoms are repulsive in nature ($\omega(H_{UPD}) > 0$); and (v) the three $\Delta_{ec-ads}G°(H_{UPD})$ versus $\theta_{H_{UPD}}$ plots reveal a cross-over point that is $\theta_{H_{UPD}}$ =

0.70 for CF_3SO_3H, $\theta_{H_{UPD}}$ = 0.80 for H_2SO_4, and $\theta_{H_{UPD}}$ = 0.85 for $HClO_4$; application of Equation 3.3 indicates that the cross-over point refer to pairs of *E* and *T* values that yield exactly the same values of $\theta_{H_{UPD}}$ and $\Delta_{ec-ads}G°(H_{UPD})$.

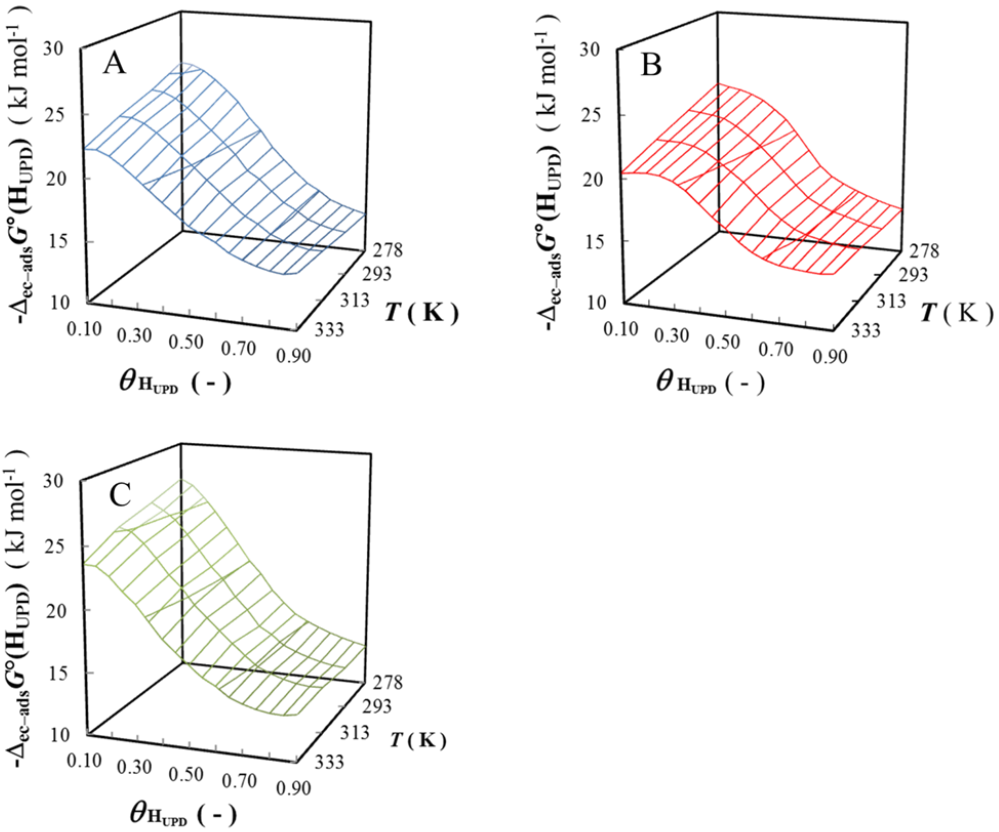

Figure 3.3. $\Delta_{ec-ads}G°(H_{UPD})$ versus $\theta_{H_{UPD}}$ plots for T = 278, 293, 313, and 333 K in CF_3SO_3H (graph A), H_2SO_4 (graph B), and $HClO_4$ (graph C).

Here, we report for the first time the values of $\Delta_{ec-ads}G°(H_{UPD})$ for CF_3SO_3OH and $HClO_4$, and reproduce $\Delta_{ec-ads}G°(H_{UPD})$ values for H_2SO_4 for the purpose of comparative analysis [11]. A comparison of the new and past results demonstrates that the anion nature has a very small impact on the values of $\Delta_{ec-ads}G°(H_{UPD})$. This behavior is not entirely unexpected because the electro-adsorption of H_{UPD} and anions occur in two different potential ranges: UPD H at $E < E_{pzc}$ (E_{pzc} stands for the potential of zero charge) and the anion electro-adsorption at $E > E_{pzc}$. Because UPD H and anion electro-adsorption can overlap over a very narrow potential range (this is limited to small coverages of H_{UPD} and anion), the anion nature might affect the values of $\Delta_{ec-ads}G°(H_{UPD})$ [9,11,26]. Indeed, this behavior is observed in Figure 3.3 but over a narrow range of $\theta_{H_{UPD}}$, and as the applied potential becomes gradually lower and as $\theta_{H_{UPD}}$ increases, the anion has no direct influence on UPD H and $\Delta_{ec-ads}G°(H_{UPD})$ adopts practically the same values with increasing for the three electrolyte.

Because the experimental results suggest that the process might follow a Temkin electro-adsorption isotherm, we can use Equation 3.4 to determine the energy of later interactions from the linear region of the $\Delta_{ec-ads}G°(H_{UPD})$ versus $\theta_{H_{UPD}}$ relationships [27-29].

$$\omega(H_{UPD}) = \left(\frac{\partial \Delta_{ec-ads}G°(H_{UPD})}{\partial \theta_{H_{UPD}}} \right)_{T=\text{const}} \tag{3.4}$$

In order to analyze linearity of the respective $\Delta_{ec-ads}G°(H_{UPD})$ versus $\theta_{H_{UPD}}$ relationships, we determined the values of the coefficient of determination of (R^2) for the linear regions of the $\Delta_{ec-ads}G°(H_{UPD})$ versus $\theta_{H_{UPD}}$ plots, and for three range of $\theta_{H_{UPD}}$, namely $0.3 \leq \theta_{H_{UPD}} \leq 0.7$,

$0.3 \leq \theta_{H_{UPD}} \leq 0.6$, and $0.3 \leq \theta_{H_{UPD}} \leq 0.5$. Table 3.1 presents the R^2 values for the three electrolytes in which the electro-adsorption of H_{UPD} was studied. The values of R^2 for $0.3 \leq \theta_{H_{UPD}} \leq 0.6$ are the highest; thus, it is reasonable to say that in this $\theta_{H_{UPD}}$ range the value of $\omega(H_{UPD})$ is constant. It is interesting to observe that the values of R^2 does not fall below 0.97 even for the $0.3 \leq \theta_{H_{UPD}} \leq 0.7$ range.

Table 3.1. R^2 values for $\Delta_{ec-ads}G°(H_{UPD})$ versus $\theta_{H_{UPD}}$ for range selective $\theta_{H_{UPD}}$ ranges ($0.3 \leq \theta_{H_{UPD}} \leq 0.7$; $0.3 \leq \theta_{H_{UPD}} \leq 0.6$; and $0.3 \leq \theta_{H_{UPD}} \leq 0.5$) in different electrolytes.

$\theta_{H_{UPD}}$ range	0.1 M CF_3SO_3H	0.5 M H_2SO_4	0.1 M $HClO_4$
$0.3 \leq \theta_{H_{UPD}} \leq 0.7$	0.992 ± 0.004	0.988 ± 0.005	0.984 ± 0.008
$0.3 \leq \theta_{H_{UPD}} \leq 0.6$	0.995 ± 0.005	0.994 ± 0.004	0.991 ± 0.006
$0.3 \leq \theta_{H_{UPD}} \leq 0.5$	0.972± 0.028	0.989 ± 0.008	0.995 ± 0.003

Figure 3.4 presents mean value of $\omega(H_{UPD})$ as a function of T for electro-adsorption of H_{UPD} on polycrystalline Pt electrode in CF_3SO_3H (blue diamonds), H_2SO_4 (red diamonds), and $HClO_4$ (green diamonds). The respective error bar shows maximum and minimum value of $\omega(H_{UPD})$ obtained through the analysis of different $\theta_{H_{UPD}}$ ranges ($0.3 \leq \theta_{H_{UPD}} \leq 0.7$; $0.3 \leq \theta_{H_{UPD}} \leq 0.6$; and $0.3 \leq \theta_{H_{UPD}} \leq 0.5$). The relationship between the mean value of $\omega(H_{UPD})$ and T is linear in the case of CF_3SO_3H and $HClO_4$ ($R^2 > 0.900$) and non-linear in the case of H_2SO_4 ($R^2 < 0.900$).

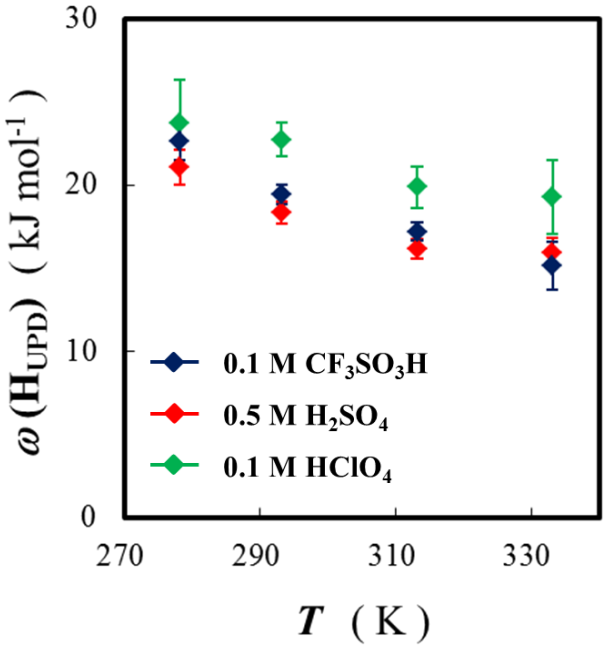

Figure 3.4. Mean value of $\omega(\mathrm{H_{UPD}})$ plotted as a function of *T* for electro-adsorption of UPD H on polycrystalline Pt electrode in CF_3SO_3H (blue diamonds), H_2SO_4 (red diamonds), and $HClO_4$ (green diamonds).

The variation of $\Delta_{ec-ads}G°(H_{UPD})$ with T at a constant H_{UPD} coverage allows the determination of $\Delta_{ec-ads}S°(H_{UPD})$ according to the following formula:

$$\Delta_{ec-ads}S°(H_{UPD}) = -\left(\frac{\partial \Delta_{ec-ads}G°(H_{UPD})}{\partial T}\right)_{\theta_{H_{UPD}} = const} \quad (3.6)$$

The relationships between $\Delta_{ec-ads}G°(H_{UPD})$ and T (Figure 3.3) are linear over the $0.10 \leq \theta_{H_{UPD}} \leq 0.90$ range suggesting that $\Delta_{ec-ads}S°(H_{UPD})$ does not change with T under these experimental conditions. Figure 3.5 presents $\Delta_{ec-ads}S°(H_{UPD})$ versus $\theta_{H_{UPD}}$ plots for the three electrolytes and reveals that $\Delta_{ec-ads}S°(H_{UPD})$ strongly depends on the H_{UPD} coverage and adopts values from –59 to +20 J mol^{-1} K^{-1}. Interestingly, the value of $\theta_{H_{UPD}}$ at which $\Delta_{ec-ads}S°(H_{UPD}) = 0$ corresponds to the above-discussed cross-over point in the $\Delta_{ec-ads}G°(H_{UPD})$ versus $\theta_{H_{UPD}}$ plots. It is an important observation to report, although at present we do not have any specific explanation for it.

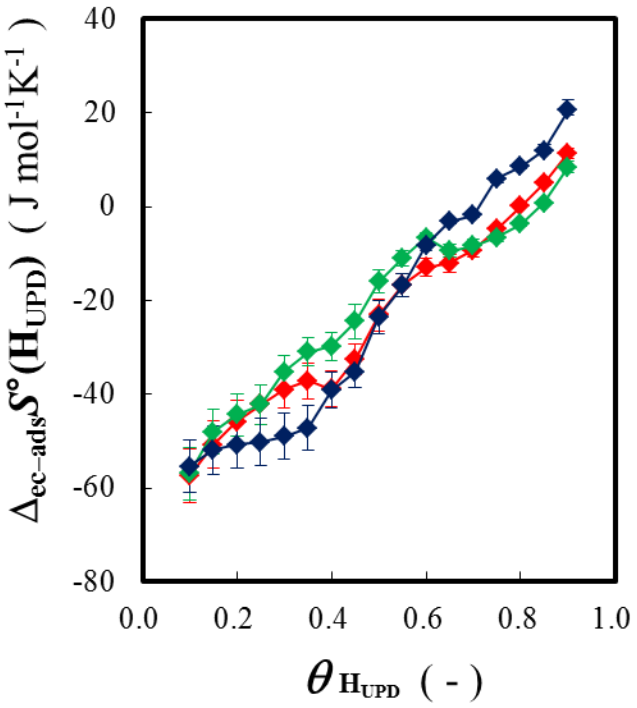

Figure 3.5 $\Delta_{ec-ads}S°(H_{UPD})$ versus $\theta_{H_{UPD}}$ plots for CF_3SO_3H (blue diamonds), H_2SO_4 (red diamonds) and $HClO_4$ (green diamonds).

The knowledge of $\Delta_{ec-ads}G°(H_{UPD})$ and $\Delta_{ec-ads}S°(H_{UPD})$ leads to the subsequent determination of the values of $\Delta_{ec-ads}H°(H_{UPD})$ and a function of $\theta_{H_{UPD}}$ and T (Equation 3.7). The results presented in Figure 3.6 for CF_3SO_3H, H_2SO_4, and $HClO_4$ demonstrate that $\Delta_{ec-ads}H°(H_{UPD})$ adopts values from –8 to –43 kJ mol^{-1} and becomes progressively less-negative as $\theta_{H_{UPD}}$ rises. In addition, the values of $\Delta_{ec-ads}H°(H_{UPD})$ do not depend on T. The latter behavior is expected because the H_{UPD} adatoms experience lateral repulsions.

$$\Delta_{ec-ads}H°(H_{UPD})_{\theta_{H_{UPD}}=const} = \Delta_{ec-ads}G°(H_{UPD})_{\theta_{H_{UPD}}=const} + T\,\Delta_{ec-ads}S°(H_{UPD})_{\theta_{H_{UPD}}=const} \quad (3.7)$$

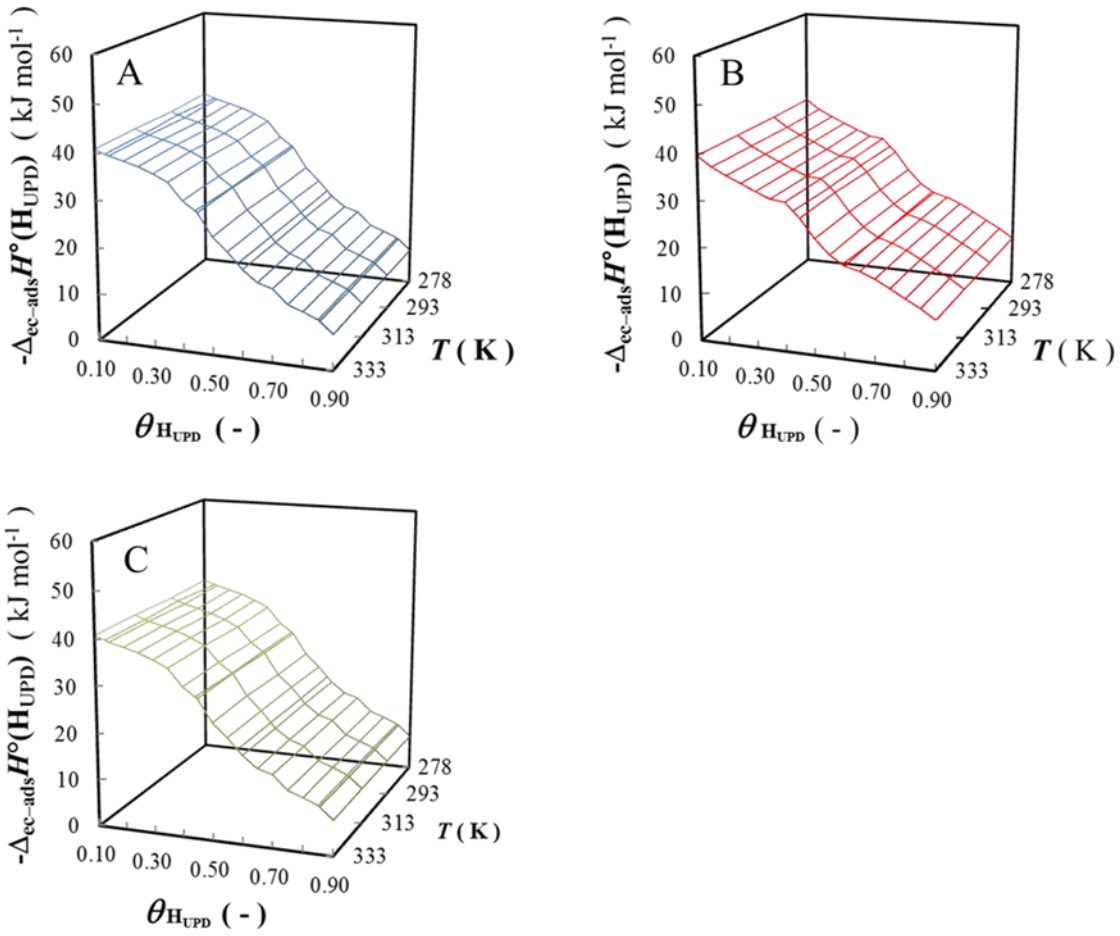

Figure 3.6. $\Delta_{ec-ads}H°(\mathrm{H_{UPD}})$ versus $\theta_{\mathrm{H_{UPD}}}$ plots for T = 278, 293, 313, and 333 K in CF_3SO_3H (graph A), H_2SO_4 (graph B), and $HClO_4$ (graph C).

It is important to compare the absolute values of $\Delta_{ec-ads}H°(\mathrm{H_{UPD}})$ and $T\,\Delta_{ec-ads}S°(\mathrm{H_{UPD}})$ in order to determine whether the process is under enthalpy or entropy control. Figure 3.7 presents plots of $|\Delta_{ec-ads}H°(\mathrm{H_{UPD}})|$ and $|T\,\Delta_{ec-ads}S°(\mathrm{H_{UPD}})|$ as a function of $\theta_{\mathrm{H_{UPD}}}$ and shows that over the entire range of $\mathrm{H_{UPD}}$ coverage $|\Delta_{ec-ads}H°(\mathrm{H_{UPD}})| > |T\,\Delta_{ec-ads}S°(\mathrm{H_{UPD}})|$ indicating that UPD H on polycrystalline on Pt in CF_3SO_3OH is always under enthalpy control. Because $\Delta_{ec-ads}G°(\mathrm{H_{UPD}})$, $\Delta_{ec-ads}S°(\mathrm{H_{UPD}})$, and $\Delta_{ec-ads}H°(\mathrm{H_{UPD}})$ adopt very similar values in the three electrolytes and reveal very similar behaviors as a function

of $\theta_{H_{UPD}}$, it is reasonable to state that UPD H on polycrystalline Pt is also enthalpy-driven in H_2SO_4 and $HClO_4$.

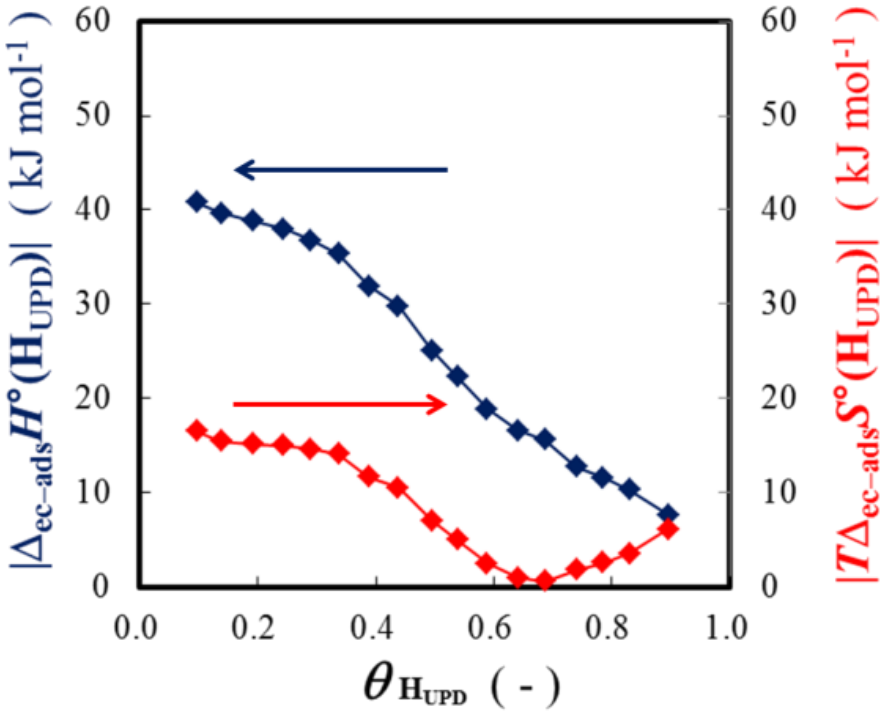

Figure 3.7. Plots of $|\Delta_{ec-ads}H°(H_{UPD})|$ and $|T\,\Delta_{ec-ads}S°(H_{UPD})|$ as a function of $\theta_{H_{UPD}}$ in CF_3SO_3H.

Knowledge of $\Delta_{ec-ads}H°(H_{UPD})$ leads to the subsequent determination of the Pt–H_{UPD} surface bond energy ($E_{Pt-H_{UPD}}$) and its analysis as a function of $\theta_{H_{UPD}}$ in the three electrolytes (Equation 3.8):

$$E_{Pt-H_{UPD}} = \frac{1}{2}D_{H_2} - \Delta_{ec-ads}H°(H_{UPD}) \qquad (3.8)$$

where D_{H_2} is the dissociation energy of H_2(g) and D_{H_2} = 436 kJ mol^{-1} [7]. The results shown in Figure 3.8 demonstrate that the values of $E_{Pt-H_{UPD}}$ vary from +225 to +261 kJ mol^{-1} depending on $\theta_{H_{UPD}}$ and are practically unaffected by the nature of electrolyte. These values are very similar to those reported for Pt(111), Pt(poly), Rh(poly), and Pt nanoparticles in various aqueous media and support the notion proposed years ago that on a thermodynamic basis H_{UPD} is equivalent to H_{chem} [8-15].

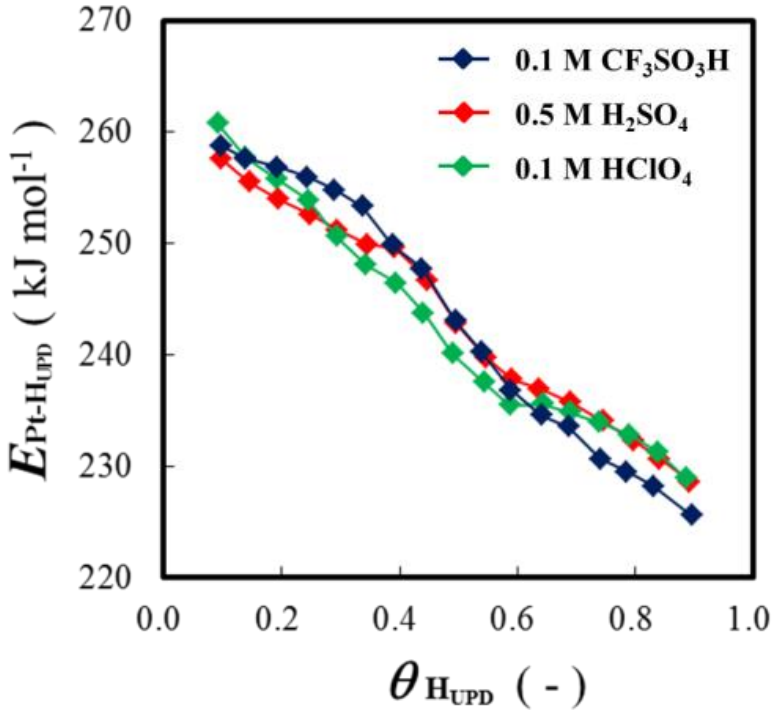

Figure 3.8. $E_{Pt-H_{UPD}}$ versus $\theta_{H_{UPD}}$ plots for CF_3SO_3H (blue diamonds), H_2SO_4 (red diamonds) and $HClO_4$ (green diamonds).

3.3.3 Role of the Anion in the Under-Potential Deposition of H

Anions that are constituents of aqueous electrolytes are known to interact with electrode surfaces; the strength of anion-electrode interactions and the anion coverage depend on the applied potential and the anion nature. The literature dealing with the subject is vast and its review is outside the scope of this contribution [30,31]. Nevertheless, it is important to discuss the anion adsorption and desorption in relation to the behavior of Pt electrodes in the potential range of UPD H.

Elsewhere, it was shown that in the case of polycrystalline and single-crystal Pt electrodes in aqueous H_2SO_4 and $HClO_4$ solutions the onset potential of anion adsorption is in the vicinity of E_{pzc} [32,33]. At $E > E_{pzc}$ the surface charge is positive ($\sigma > 0$) and drives the electro-adsorption of anions; the process is accompanied by charge transfer, thus the anion adsorption is an anodic process. At $E < E_{pzc}$ the surface charge is negative ($\sigma < 0$) and the anion adsorption cannot take place. The onset potential of UPD H is also within the vicinity of E_{pzc} but the process requires that the surface charge be negative because the discharge of hydrated H^+ is a cathodic process. Because UPD H is a reduction process that requires $E < E_{pzc}$ and because the electro-adsorption of anion is an oxidation process that requires $E > E_{pzc}$, these two processes are expected to have little or no impact on each other. However, the anion present in the electrolyte remains in the electric double layer (in the outer Helmholtz layer) and can interact with the electrode surface through long-range electrostatic interactions even if $E < E_{pzc}$. Consequently, the anion can have a certain (even if small) impact on UPD H. The results presented in this contribution reveal a small but not negligible influence the anion nature on UPD H in the potential range at which $\theta_{H_{UPD}}$ is small. This influence is visible in the $\Delta_{ec-ads}G°(H_{UPD})$ versus $\theta_{H_{UPD}}$ plots for small values of $\theta_{H_{UPD}}$ (Figure 3.3). Because the variation of $\Delta_{ec-ads}G°(H_{UPD})$

with $\theta_{H_{UPD}}$ determines the nature and strength of lateral interactions between the H_{UPD} adatoms, the influence of anion is also visible in the $\omega(H_{UPD})$ versus $\theta_{H_{UPD}}$ profiles (Figure 3.4). Interestingly, the influence of anion is practically negligible in the $\Delta_{ec-ads}S°(H_{UPD})$ versus $\theta_{H_{UPD}}$ (Figure 3.5), $\Delta_{ec-ads}H°(H_{UPD})$ versus $\theta_{H_{UPD}}$ (Figure 3.6), and $E_{Pt-H_{UPD}}$ versus $\theta_{H_{UPD}}$ plots (Figure 3.8).

3.4 Conclusions

Trifluoromethanesulfonic acid (CF_3SO_3H) is the smallest fluorinated sulfonic acid and can serves as a suitable molecular model mimicking the interfacial behavior of Nafion® ionomer in fuel cell catalyst layers. The electro-adsorption of H_{UPD} on Pt polycrystalline in aqueous CF_3SO_3H solution was studied in the 278–333 K temperature range using cyclic-voltammetry with the objective of determining thermodynamic state functions governing the process, namely $\Delta_{ec-ads}G°(H_{UPD})$, $\Delta_{ec-ads}S°(H_{UPD})$,and $\Delta_{ec-ads}H°(H_{UPD})$. Cyclic-voltammetry profiles obtained in CF_3SO_3H revealed the usual features associated with the electro-adsorption of H_{UPD} as well as with the surface oxide formation and reduction. The application of general electrochemical adsorption isotherm allowed us to determine that $\Delta_{ec-ads}G°(H_{UPD})$ varies from –13 to –27 kJ mol^{-1}; $\Delta S^{\circ}_{ads}(H_{UPD})$ varies from –59 to +20 kJ mol^{-1} K^{-1} ; $\Delta H^{\circ}_{ads}(H_{UPD})$ varies from –8 to –43 kJ mol^{-1}. In addition, we determined the Pt–H_{UPD} surface bond energy ($E_{Pt-H_{UPD}}$) adopted values from 225 to 261 kJ mol^{-1}. The lateral interactions between the H_{UPD} adatoms were found to be repulsive in nature and the energy of lateral interactions ($\omega(H_{UPD})$) was determined to vary from +14 to +22 kJ mol^{-1}. The process of H_{UPD} electro-adsorption follows a Temkin electro-adsorption isotherm and the energy of lateral interactions is temperature-dependent. A comparison of the values of $\Delta_{ec-ads}S°(H_{UPD})$, $\Delta_{ec-ads}G°(H_{UPD})$, $\Delta_{ec-ads}H°(H_{UPD})$, $\omega(H_{UPD})$ and $E_{Pt-H_{UPD}}$ obtained in CF_3SO_3H with those obtained in H_2SO_4 and $HClO_4$ reveals that they are very similar indicating that the anion constituting the electrolyte has little impact on the process. The ability to analyze thermodynamics of UPD H in aqueous CF_3SO_3OH indicates that other surface electrochemical processes taking place at Pt electrodes can be successfully examined.

3.5 References

(1) D. Papageorgopoulos, 2013 Fuel Cells Annual Merit Review (U.S. Department of Energy, Arlington, Virginia, 2013)

(2) A. Ohma, T. Mashio, K. Sato, H. Iden, Y. Ono, K. Sakai, K. Akizuki, S. Takaichi, K. Shinohara, Electrochim. Acta **56**, 10832 (2011)

(3) M. W. Breiter, Trans. Faraday Soc. **60**, 1445 (1964)

(4) B. E. Conway, H. Angerstein-Kozlowska, W. B. A. Sharp, J. Chem. Soc. Faraday Trans. 1 **74**, 1373 (1978)

(5) G. Jerkiewicz, J. J. Borodzinski, W. Chrzanowski, B. E. Conway, J. Electrochem. Soc. **142**, 3755 (1995)

(6) G. Jerkiewicz, A. Zolfaghari, J. Electrochem. Soc. **143**, 1240 (1996)

(7) G. Jerkiewicz, A. Zolfaghari, J. Phys. Chem. **100**, 8454 (1996)

(8) G. Jerkiewicz, Prog. Surf. Sci. **57**, 137 (1998)

(9) G. Jerkiewicz, Electrocatalysis **1**, 179 (2010)

(10) A. Zolfaghari, G. Jerkiewicz, J. Electroanal. Chem. **467**, 177 (1999)

(11) A. Zolfaghari, M. Chayer, G. Jerkiewicz, J. Electrochem. Soc. **144**, 3034 (1997)

(12) N. Garcia-Araez, J. Phys. Chem. C **115**, 501 (2011)

(13) R. Gomez, J. M. Orts, B. Alvarez-Ruiz, J. M. Feliu, J. Phys. Chem. B **108**, 228 (2004)

(14) N. M. Markovic, T. J. Schmidt, B. N. Grgur, H. A. Gasteiger, R. J. Behm, P. N. Ross J. Phys. Chem. B **103**, 8568 (1999)

(15) Y. Huang, F. T. Wagner, J. Zhang, J. Jorne, J. Electrochem. Soc. **161**, F653 (2014)

(16) R. Subbaraman, D. Strmcnik, V. Stamenkovic, N. M. Markovic, J. Phys. Chem. C **114**, 8414 (2010).

(17) H. Hanawa, K. Kunimatsu, M. Watanabe, H. Uchida, J. Phys. Chem. C **116**, 21401 (2012)

(18) K. Kodama, R. Jinnnouchi, T. Suzuki, H. Murata, T. Hatanaka, Y. Morimoto, Electrochem. Com. **36**, 26 (2013)

(19) T. Masuda, F. Sonsudin, P. R. Singh, H. Naohara, K. Uosaki, J. Phys. Chem. C **117**, 15704 (2013)

(20) A. Ohma, K. Fushinobu, K. Okazaki, Electrochim. Acta **55**, 8829 (2010)

(21) G. Attard, A. Brew, K. Hunter, J. Sharman, E. Wright, Phys. Chem. Chem. Phys. **16**, 13689 (2014)

(22) M. Alsabet, M. Grden, G. Jerkiewicz, J. Electroanal. Chem., **589**, 120 (2006)

(23) B. E. Conway, H. Angerstein-Kozlowska, W. A. Sharp, E. E. Criddle, Anal. Chem. **45**, 1331 (1973)

(24) D. Chen, Q. Tao, L.W. Liao, S.X. Liu, Y.X. Chen, S. Ye, Electrocatalysis **2**, 207 (2011)

(25) H. Angerstein-Kozlowska, in Comprehensive Treatise of Electrochemistry, vol. 9, ch. 1, ed. by E. Yeager, J.O'.M. Bockris, B.E. Conway, S. Sarangapani (Plenum, New York, 1984), p. 15

(26) M. Osawa, M. Tsushima, H. Mogami, G. Samjeske, Y. Akira, J. Phys. Chem. C **112**, 4248 (2008)

(27) W. Schmickler *Interfacial Electrochemistry*, (Oxford University Press, New York, 1996)

(28) C. H. Hamann, A. Hamnett, W. Vilstich, *Electrochemistry*, (Wiley-VCH, 2007)

(29) R. Greef, R. Peat, L. M. Peter, D. Pletcher, J. Robinson, *Instrumental Methods in Electrochemistry*, (Ellis Horwood Ltd, United Kingdom, 1985)

(30) E.K. Krauskopf, A. Wieckowski, in Adsorption of Molecules at Metal Electrodes, ed. by J. Lipkowski, P.N. Ross, (VCH, New York, 1992), p. 119

(31) Y. Shingaya, M. Ito, in Interfacial Electrochemistry, ed. by A. Wieckowski, (Marcel Dekker, New York, 1999), p 287

(32) M.E. Gamboa-Aldeco, E. Herrero, P.S. Zelenay, A. Wieckowski, J. Electroanal. Chem. **348**, 451 (1993)

(33) A. Kolics, A. Wieckowski, J. Phys. Chem. B **105**, 2588 (2001)

Chapter 4

Influence of Electrolyte on Composition and pH on Platinum Electrochemical and Chemical Dissolution in Acidic Media

4.1 Introduction

Polymer electrolyte membrane fuel cells (PEMFCs) are promising sources of electrical power for zero emission vehicles (ZEVs). Although there have been many intense efforts involved in the development of PEMFCs over the past ten years, further cost reduction and improvement of performance and durability are key issues that need to be addressed in order to achieve mass production of affordable fuel cell electric vehicles (FCEVs). Catalyst layers (CLs), which are one of the main components of fuel cells, comprise Pt nano-particles (Pt-NPs) that are covered with ionomer (e.g. Nafion®) and reside on a carbon support; the Pt-NPs are the electrocatalysts at which the hydrogen oxidation reaction (HOR) and oxygen reduction reaction (ORR) occur. In order to make FCEVs part of our daily life, it is essential to reduce the Pt loading without sacrificing their performance and durability [1,2]. Decrease in the size of Pt-NPs is one of the approaches that can lead to a reduction in Pt loading, but at the same time it increases the particles' surface Gibbs energy and reduces their stability, resulting in their gradual degradation [3-7]. Consequently, Pt-NPs are more prone to electro-dissolution than bulk materials and their degradation during the operation of PEMFCs is a very important scientific and technological issue that requires attention.

During accelerating, decelerating, idling, start-up, and shut-down (repetitive accelerating, and decelerating is often referred to as load cycling) automotive fuel cells operate at relatively high potentials, at which the Pt surface undergoes partial or complete electro-oxidation [9-12]. The Pt surface oxide influences the lifetime of Pt-NPs; the surface oxide can function as a protective (passive) layer on metallic Pt [3,13-15] or can facilitate Pt (electro-)dissolution, if the Pt oxide is thermodynamically less stable than metallic Pt. Such a behavior could be related to the surface oxide structure, which exposes to the electrolyte the place-exchanged Pt^{2+} surface species [5,6,13,16-19]. Because the composition and structure of Pt surface oxides affect the rate of their (electro-)dissolution, it is important to analyze the process in relation to polarization conditions and electrolyte composition and pH.

The very initial stage of Pt oxide growth involves the discharge of H_2O molecule and leads to the formation of electro-adsorbed O (chemisorbed O, O_{chem}) and the departure of two hydrated protons:

$$Pt(s) + H_2O(l) \xrightarrow{O\,electro-adsorption} Pt^{\delta+} - O^{\delta-}{}_{chem} + 2\,H^+(aq) + 2e^- \qquad (4.1)$$

In the case of polycrystalline Pt, the process commences at 0.85 V and as the potential reaches ca. 1.15 V, about half a monolayer of O_{chem} forms [20]. As the Pt surface oxide growth progresses and the amount of O_{chem} increases, a quasi-three-dimensional lattice comprising Pt^{2+} and O^{2-} surface species develops via an interfacial place-exchange mechanism according to the following reaction [20,21].

$$Pt_{surf}{}^{\delta+} - O^{\delta-}{}_{chem} \xrightarrow{interfacial\ place\ exchange} \left(Pt^{2+} - O^{2-}\right)_{quasi-3D\,lattice} \qquad (4.2)$$

The process and the structure that develops are very important because they modify the electronic nature of Pt and O surface species; the place-exchanged PtO and the electronic structure of the two species affect the rate at which PtO can undergo (electro-)dissolution.

Several studies deal with Pt electro-dissolution in relation to various experimental parameters, such as the upper and lower potential limit (E_U and E_L, respectively) [13,15,17-19,22], the potential scan rate (s) [13,19,24], temperature (T) [13,24], presence of gaseous species [16,25,26], the electrolyte composition and pH [27], and types of Pt materials [28].

E_U and E_L are possibly the two most important experimental parameters the impact of which needs to be examined in order to understand the mechanistic and kinetic aspects of Pt electro-dissolution during the operation of FCEVs. Several groups reported that Pt electro-dissolution becomes more pronounced when E_U is raised from 1.10 to 1.20 V (for E_L = const) [13,15,17,22]. This observation serves as evidence that Pt electro-dissolution is facilitated by the interfacial place-exchange, which exposes oxidized Pt atoms (place-exchanged Pt^{2+}) at the surface (Equation 4.2). It was also reported that the Pt electro-dissolution is affected by E_L (for E_U = const), which in some instances might be low enough to drive electrodeposition of previously electro-dissolved Pt [13,15,17,22].

The anion constituting an acidic electrolyte can influence Pt electro-dissolution through its interaction with the Pt surface and also by affecting the equilibrium constant of the dissolved Pt^{z+} complex compound. In CLs, Nafion® acts both as a solid electrolyte and a separator; due to its direct contact with Pt-NPs, it can impact Pt electro-dissolution. The environment experienced by Pt-NPs being in direct contact with the Nafion® ionomer is different from that encountered in conventional acidic media: the proton concentration is high and the anion (here sulfonic group)

adsorbed on the Pt surface is immobile due to its polymeric nature (or has very little mobility); its interactions with Pt is reported to be weak [29-32]. Although numerous papers report on Pt electro-dissolution in conventional acidic media (e.g. aqueous H_2SO_4 and $HClO_4$ solutions), the knowledge of the influence of electrolyte nature on the process is very limited. Trifluoromethanesulfonic acid (CF_3SO_3H, abbreviated as TFMSA) is the smallest fluorinated sulfonic acid and can serve as a suitable molecular model that mimics the Nafion® ionomer in CLs [33-35]. The strength of anion interaction with the Pt surface in CF_3SO_3H is weaker than that in H_2SO_4 [36-39]. Because Pt electro-dissolution occurs in the potential range in which the anion can adsorb, the process should be examined in aqueous CF_3SO_3H solutions. In particular, in order to better understand its mechanism and kinetics, and the impact of electrolyte, it is necessary to study Pt electro-dissolution in electrolytes having different anions and pH concentrations [19].

In this chapter, we report on a study of Pt electro-dissolution upon potential cycling in aqueous CF_3SO_3H, H_2SO_4, and $HClO_4$ solutions. The process is examined in relation to the electrolyte nature and its concentration with the objective of determining whether the anion nature and the electrolyte pH have any impact on the process. The amount of electro-dissolved Pt present in the electrolytes is analyzed using inductively coupled plasma mass spectrometry.

4.2 Experimental

4.2.1 Electrode, Electrolyte, and Electrochemical Cell

The working (WE) and counter (CE) electrodes were made of Pt foil; each was spot-welded to a Pt wire that was sealed in a glass tube. The working and counter electrodes were degreased in acetone under reflux followed by rinsing with ultra-high purity ethanol. Then, they were cleaned in concentrated H_2SO_4 for 24 hours and rinsed several times (at least ten times) with ultra-high purity water (MilliPore, Milli-Q3; $\rho \geq 18.2$ MΩ cm). The geometric dimensions of WE and CE were 1.55 cm × 1.65 cm. The electrochemically active surface area (A_{ecsa}) of the WE electrode was determined from the charge of the under-potential deposition of H (UPD H) [40]. The electrode's roughness factor ($R' = A_{ecsa} / A_{geom}$) was found to be ca. 1.7. The reference electrode was Pt/Pt black placed in the same electrolyte but in a separate compartment through which H_2(g) (p_{H2} = 1 atm) pre-saturated with water vapor was passed. It served as a reversible hydrogen electrode (RHE). The RHE compartment was electrolytically connected to the WE compartment by means of a Luggin capillary. All potentials measured experimentally and referred to in this paper are expressed with respect to RHE. All electrochemical experiments were conducted in a three-compartment cell in order to avoid any influence of electro-dissolved Pt in the CE compartment [13]. The WE and CE were placed in two different compartments which were electrolytically connected by a means of Nafion® 211 membrane. A new Nafion membrane was used in each experiment.

High purity aqueous electrolyte was prepared from concentrated CF_3SO_3H (ReagentPlus, Sigma-Aldrich > 99 %), H_2SO_4 (Fluka, > 95 %), $HClO_4$ (Sigma-Aldrich, > 70 %) and ultra-high purity water (MilliPore, Milli-Q3; its resistivity was $\rho \geq 18.2$ MΩ cm). The concentrated acids

were used as received without any further purification. The glassware was cleaned using well-established and widely accepted procedures [41]. Ultra-high purity N_2(g) pre-saturated with water vapor was passed through electrolyte in the WE and CE compartments. The stability and reproducibility of CV profiles was carefully verified as a measure of the purity of the experimental setup including the electrolyte solution. All experiments were conducted at room temperature (T = 293 K).

4.2.2 Potential Cycling Experiments and Electrolyte Solution Collection for Analysis

After assembling the experimental setup, the WE and CE compartments were purged with ultra-high purity N_2(g) for ca. 30–60 minutes. The electrolyte solution in the WE compartment was agitated using a magnetic stirrer. The working electrode was cycled 10 times in the 0.05–1.40 V range at a potential scan rate of s = 50 mV s^{-1}. Then, an aliquot of ca. 1.0 mL of electrolyte was collected from the WE compartment; it served as a blank and refers to the 0^{th} potential cycle. Repetitive potential cycling was started immediately afterwards, while the electrolyte was continuously agitated using a magnetic stirrer. A square-wave potential program was used as shown Figure 4.1; the lower and upper potential limits were E_L = 0.60 V and E_U = 1.20 V, respectively; a scan rate of s = 7500 mV s^{-1} was employed to change the applied potential from E_L to E_U and vice versa (the scan rate was so fast that the potential profile can be considered to be practically square-shaped); the potential was held at E_L and E_U for a holding time of t = 3.00 s. An aliquot of ca. 1.0 mL of electrolyte was collected at the following potential cycles (n): 100^{th}, 500^{th}, 1000^{th}, 3000^{th}, and 5000^{th}. The electrolyte solution volume was maintained constant by adding ca. 1.0 mL of fresh electrolyte after collecting the electrolyte. The electrolyte samples were carefully weighed (their accurate mass and volume were required for quantitative analysis)

and carefully diluted five-fold prior to submission for inductively coupled plasma mass spectrometry measurements [13].

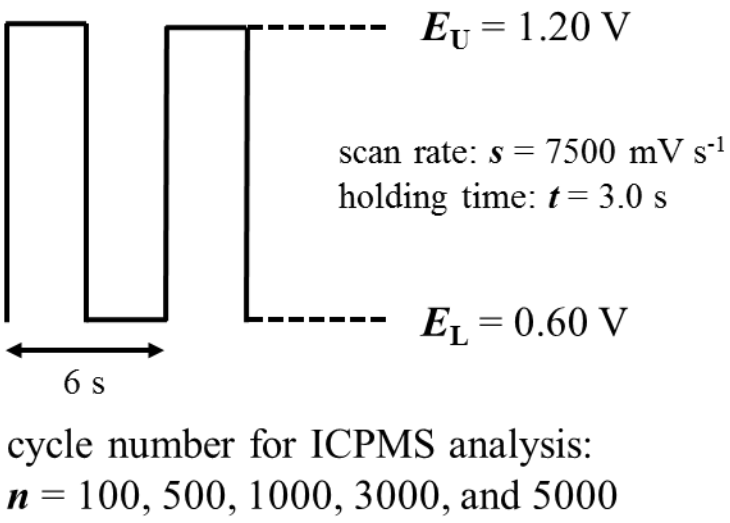

Figure 4.1. Schematic of potential cycling; upper potential limit E_U = 1.20 V; lower potential limit E_L = 0.60 V; upper potential limit E_U = 1.20 V; scan rate s = 7500 mV s^{-1}; hold time t = 3.00 s for each potential limit.

4.2.3 ICP-MS analysis

Inductively coupled plasma mass spectrometry (ICP-MS) analysis was performed using a Varian 820-MS instrument with a detection limit of 10 ppt for Pt, measured as ^{195}Pt, when performing flow injection. Continuous sample aspiration was not done to minimize corrosion of the instrument. Instead, 100 μL injections were made in 1 % (v/v) HNO_3 carrier using 100 μL injection loop (Ryeodyne Inc., Cotati, CA) mounted on a universal automatic actuator (Anachem Ltd, England). The standard solutions for ICP-MS measurements were prepared by dilution of Pt

stock solution (10000 μg/mL in 10% HCl, SCP Science) in five-fold diluted electrolyte solution and were measured in order to prepare a calibration curve. The range of Pt concentration of standard solution was 1–75 ppb. The sample introduction system was then flushed with the blank solution until the counts returned to the level comparable to that prior to measurements. The samples were then analyzed in the sequence of collection [13].

4.2.4 Determination of the PtO Surface Coverage

A surface oxide was grown on polycrystalline Pt electrode under potentiostatic conditions by applying a constant polarization potential of E_p = 1.20 V for a controlled polarization time in the $10^0 \leq t_p \leq 10^4$ s range. In each separate experiment, a surface oxide formed by potentiostatic polarization was subsequently reduced in a single negative-going CV transient at a potential scan rate of s = 50 mV s^{-1}. All CV oxide-reduction profiles show one feature, the so-called OC1 peak, which corresponds to the reduction of surface PtO to metallic Pt, as described elsewhere [42]. The oxide reduction CV profiles were integrated and the oxide charge density (q_{ox}) values were determined. The amount of PtO also expressed as O_{chem} coverage (θ_O) was determined by dividing q_{ox} by the charge density associated with the formation of one monolayer of O_{chem}, thus by $q_{ox,1ML}$ = 440 μC cm^{-2}.

4.3 Results and Discussion

4.3.1 Platinum Electro-dissolution in Aqueous CF_3SO_3H, H_2SO_4, and $HClO_4$ Solutions

Figure 4.2 presents two graphs for a polycrystalline Pt electrode in aqueous CF_3SO_3H (blue line), H_2SO_4 (red line), and $HClO_4$ (green line) solutions obtained at s = 50 mV s^{-1} and T = 293 K; the graphs A and B are for 0.1 and 0.5 M acid solutions, respectively. The CV transients reveal the usual features corresponding to the electro-adsorption and electro-desorption of under-potential deposited H (H_{UPD}) and the formation and reduction of Pt surface oxide; the shape of the CV profiles demonstrate that the system (electrodes, electrolyte, cell) is impurity-free.

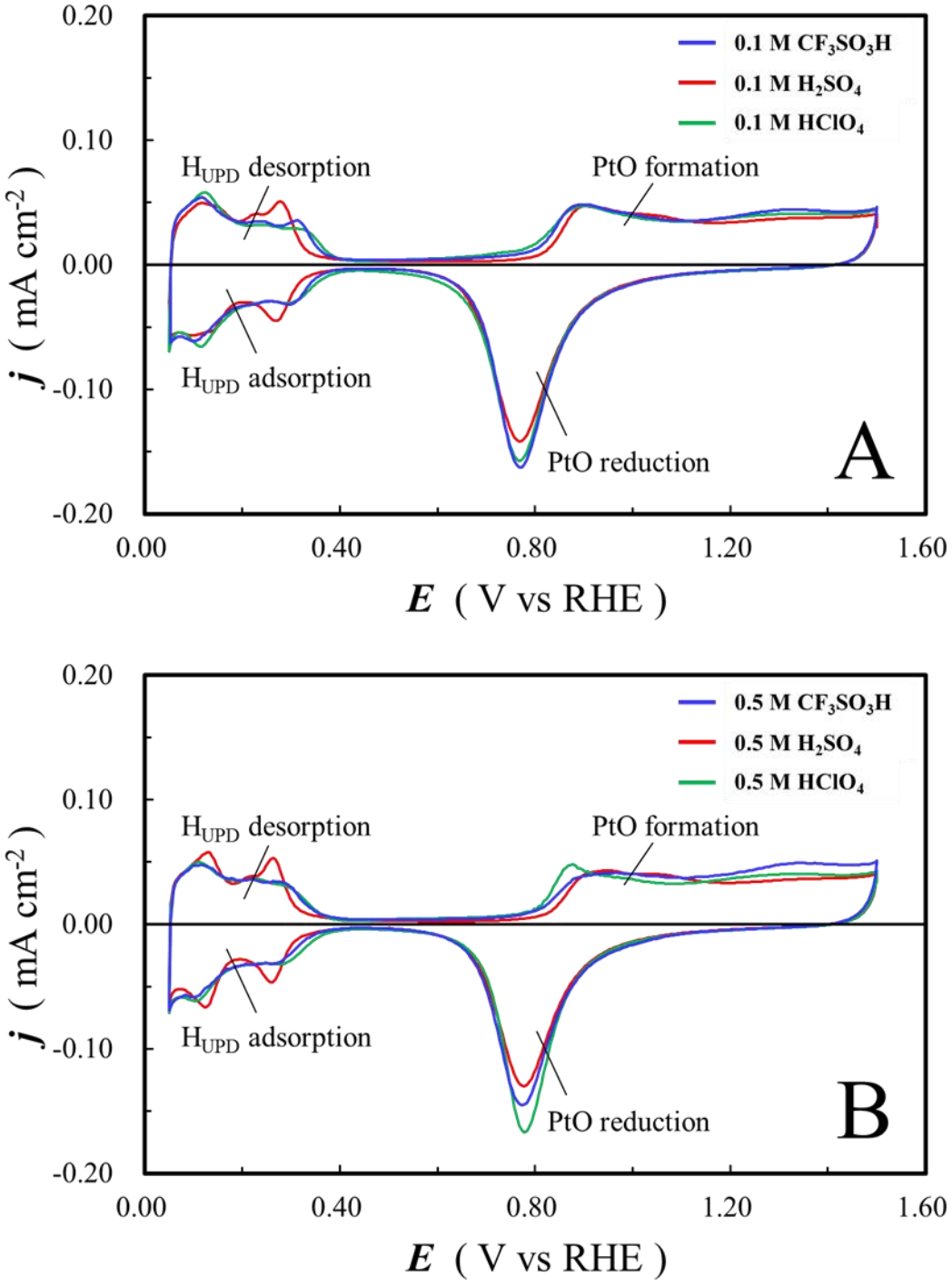

Figure 4.2. Two CV profiles for the polycrystalline Pt electrode in aqueous CF_3SO_3H (blue line), aqueous H_2SO_4 (red line), and aqueous $HClO_4$ (green line) obtained at s = 50 mV s^{-1} , and T = 293 K with different concentrations: A for 0.1 M solution; B for 0.5 M solution.

Repetitive potential cycling in the 0.60–1.20 V range involves PtO formation and reduction. The onset potential of H_{UPD} electro-adsorption in the H_2SO_4 solution is slightly lower than that in the CF_3SO_3H and $HClO_4$ solutions. The CV profiles obtained in the CF_3SO_3H and $HClO_4$ solutions are similar suggesting that the anions experience similar interactions with the Pt surface. In addition, the CV peaks for UPD H in the CF_3SO_3H and $HClO_4$ solutions have lower current density (j) values than those in the H_2SO_4 solution. These variances are attributed to different strengths of anion interactions with the Pt electrode; the strength of anion adsorption of HSO_4^{-1} or $SO_4^{2-}$is stronger than $CF_3SO_3^{-1}$ and ClO_4^{-1}.

Figure 4.3 presents the amount of electro-dissolved Pt (m_{Pt} in ng cm^{-2}) versus cycle number (n) plots for potential cycling in the 0.60–1.20 V range at s = 7500 mV s^{-1} and T = 293 K in aqueous CF_3SO_3H (blue symbols), H_2SO_4 (red symbols), and $HClO_4$ (green symbols) solutions having two different concentrations (c), namely c = 0.1 and 0.5 M. The error bars indicate maximum and minimum values of these experiments. The errors are attributed to (i) the determination of real surface area, (ii) the measurement of the weight of 1.0 mL electrolyte aliquots for ICP-MS, and (iii) the determination of electro-dissolved Pt by ICP-MS measurements. The amount of electro-dissolved Pt is cumulative and refers to the total amount in the electrolyte solutions. The results presented in Figure 4.3 can be summarized as follows: (i) in the case of 0.1 M solutions (open diamonds), the amount of electro-dissolved Pt is practically the same in the three electrolytes; (ii) in the case of 0.5 M solutions (filled diamonds), the amount of electro-dissolved Pt in H_2SO_4 solution has higher values than in the other two solutions; (iii) the amount of electro-dissolved Pt in the 0.5 M H_2SO_4 solution is ca. 4–5 times higher than that in the 0.1 M H_2SO_4 solution; (iv) the amount of electro-dissolved Pt in the 0.5 M CF_3SO_3H and $HClO_4$ solutions is ca. 3–4 times higher than that in 0.1 M CF_3SO_3H and $HClO_4$ solutions. Here, we report for the first time experimental data for Pt electro-dissolution in CF_3SO_3H solutions brought

about by potential cycling under conditions that mimic operating FCEVs. Our results show that for a given acid concentration, the amount of electro-dissolved Pt in the CF_3SO_3H solution is practically the same as that in the $HClO_4$ solution. In addition, the data show that the electrolyte concentration has a major impact on Pt electro-dissolution [19]. This behavior is expected because any variation in the electrolyte concentration leads to changes in both the anion and proton concentrations.

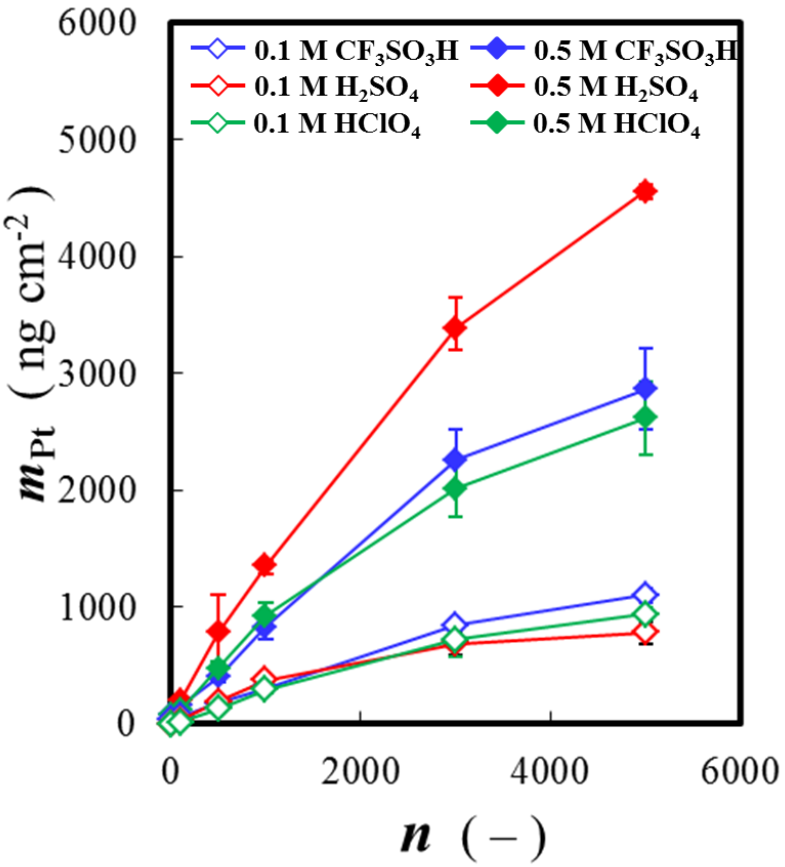

Figure 4.3. m_{Pt} versus n plots for potential cycling in the 0.60–1.20 V range at s = 7500 mV s^{-1} and T = 293 K in aqueous CF_3SO_3H (blue symbols), H_2SO_4 (red symbols), and $HClO_4$ (green

symbols) solutions having two different concentrations (c), namely c = 0.1 and 0.5 M. The error bars indicate maximum and minimum values of these experiments. .

4.3.2 Electro-dissolution in Aqueous $HClO_4$ Solution without and with H_2SO_4 Addition

$HClO_4$ is accepted to be a non-adsorbing or weakly adsorbing electrolyte and is often used in interfacial electrochemistry and electrocatalysis studies for a comparative analysis with a strongly adsorbing electrolyte (e.g. H_2SO_4). In this study, we examine Pt electro-dissolution in 0.1 and 0.5 M $HClO_4$ solutions without and with an addition of H_2SO_4 (the concentration of H_2SO_4 after the addition is 0.01 M) with the objective of examining the impact of the anion nature on the process. Figure 4.4 presents CV profiles for a polycrystalline Pt electrode in $HClO_4$ solutions without (green line) and with (red line) addition of H_2SO_4 obtained at s = 50 mV s^{-1} and T = 293 K; the graphs A and B refer to 0.1 and 0.5 M $HClO_4$ solutions, respectively. The CV profiles reveal that the addition of H_2SO_4 shifts the CV peaks associated with UPD H towards slightly less-positive potential values and makes them sharper. The same qualitative features are observed in both the 0.1 and 0.5 M $HClO_4$ solutions. Because UPD H and anion electro-adsorption can overlap over a very narrow potential range (this is limited to small coverages of H_{UPD} and anion), the CV feature in the low H_{UPD} coverage region is influenced by the anion. Because HSO_4^- and SO_4^{2-} are strongly adsorbing species, the potential shift and the increase in the peak sharpness can be attributed to the anion interaction with the Pt surface. One could argue that higher concentrations of H_2SO_4 could be employed to further examine the anion effect, but it is well-established that the anion coverage reaches saturation already at concentrations in the 0.001–0.01 M range [43].

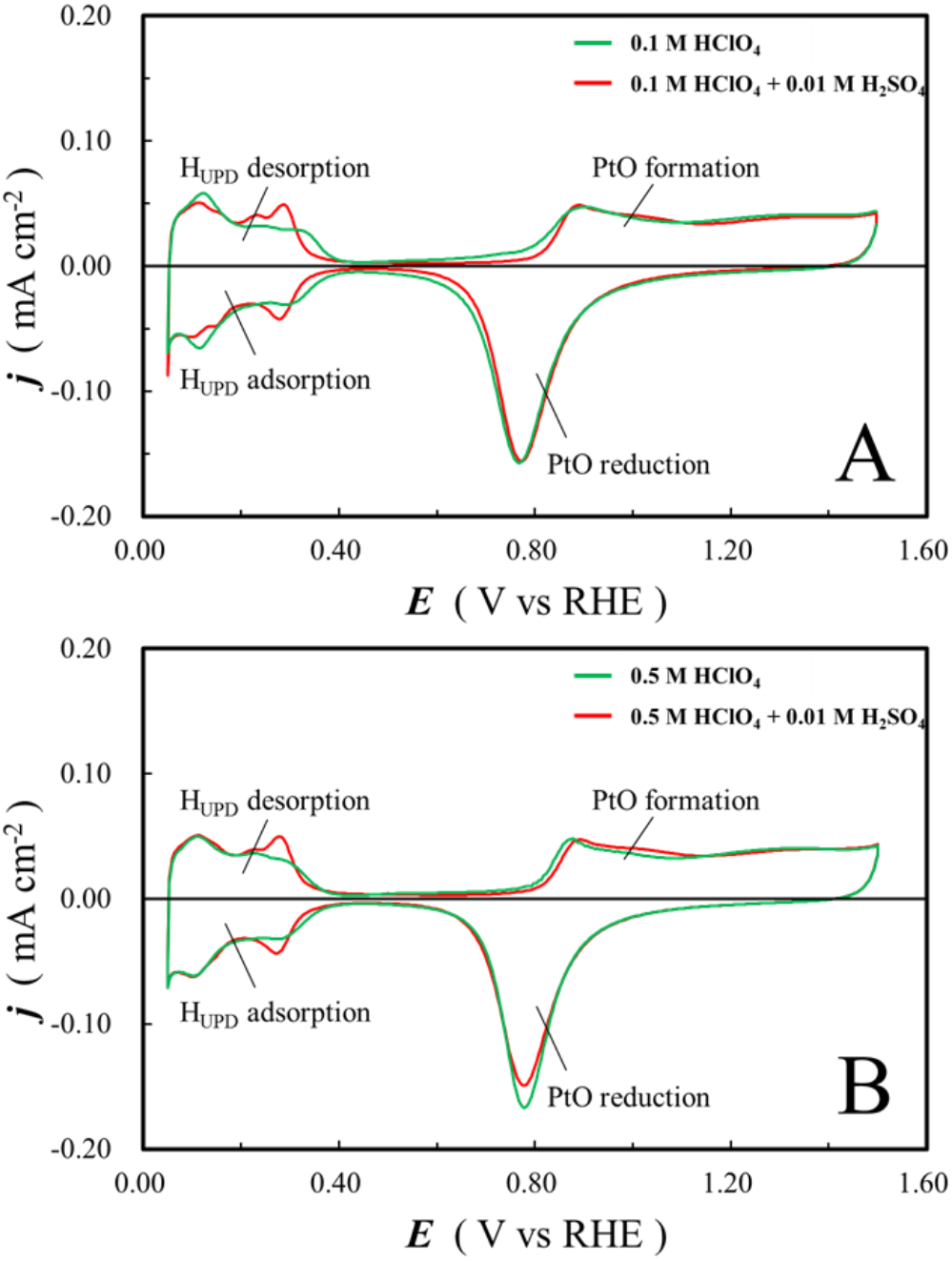

Figure 4.4. Two CV profiles for the polycrystalline Pt electrode in $HClO_4$ solution without (green line) or with (red line) 0.01 M H_2SO_4 solution, obtained at s = 50 mV s^{-1} and T = 293 K with different concentrations: A for 0.1 M $HClO_4$ solution; B for 0.5 M $HClO_4$ solution.

Figure 4.5 presents m_{Pt} versus n plots for potential cycling in the 0.60–1.20 V range at s = 7500 mV s^{-1} and T = 293 K in 0.1 and 0.5 M $HClO_4$ solution without (green symbols) and with (red symbols) the addition of H_2SO_4 (the concentration of H_2SO_4 after the addition is 0.01 M). The amount of electro-dissolved Pt is cumulative and refers to the total amount in the electrolyte solutions. The results demonstrate that the addition of H_2SO_4 does not alter the amount of electro-dissolved Pt. The same qualitative behavior is observed for both the 0.1 and 0.5 M $HClO_4$ solutions. Also, the amount of electro-dissolved Pt in the 0.5 M $HClO_4$ solution is higher than that in the 0.1 M $HClO_4$ solution irrespective of the presence of H_2SO_4. We wish to add that the proton activity in $HClO_4$ with H_2SO_4 is almost the same as that in the $HClO_4$ solution alone, because the concentration of H_2SO_4 is at least an order of magnitude smaller than the concentration of $HClO_4$. Thus, the addition of H_2SO_4 does not modify the overall proton activity (or modifies it only slightly) but replaces weakly adsorbing anions with strongly adsorbing ones. The results presented in Figure 4.5 lead to the conclusion that the anion has no or negligible impact on Pt electro-dissolution but the pH significantly affects the process.

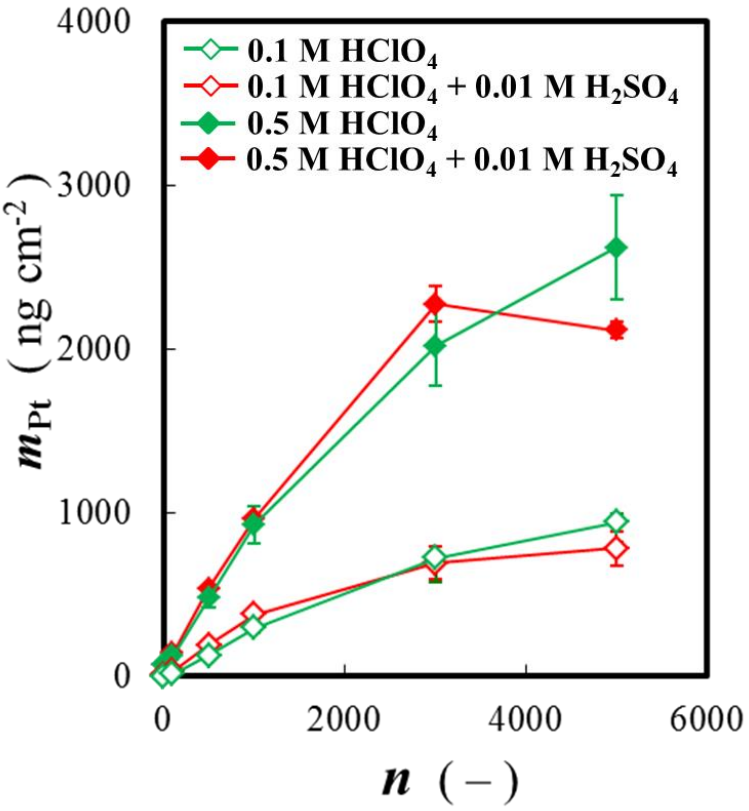

Figure 4.5. m_{Pt} versus n plots for potential cycling for 0.60–1.20 V at s = 7500 mV s^{-1} and T = 293 K in 0.1 and 0.5 M $HClO_4$ solution without (green symbols) and with (red symbols) the addition of H_2SO_4 (the concentration of H_2SO_4 after the addition is 0.01 M). The error bars indicate maximum and minimum values of these experiments.

We also examined the influence of anion nature on PtO formation, because the amount of PtO present on a Pt electrode can affect Pt electro-dissolution of the electro-dissolved Pt originate from Pt. Figure 4.6 presents q_{ox} versus log t_p plots for E_p = 1.20 V and T = 293 K in 0.1 and 0.5 M $HClO_4$ solutions without (green symbols) and with (red symbols) addition of H_2SO_4 (the concentration of H_2SO_4 after the addition is 0.01 M). As expected, the results demonstrate that

q_{ox} increases with a rise in t_p but the values of q_{ox} in the four electrolytes differ by only ca. 7–10% (this is close to the experimental uncertainty of q_{ox} determination) throughout the entire t_p range indicating that the anion nature and electrolyte concentration have little impact on the PtO development. The values of q_{ox} are consistently in the 250–440 μC cm^{-2} range, thus the O_{chem} coverage varies from 0.57 to 1.0. Above, it is explained that in the case of polycrystalline Pt the interfacial place-exchange commences when O_{chem} reaches the coverage of θ_O = 0.5 and the surface oxide is completely place-exchanged when θ_O = 1.0 (Equation 4.2). Thus, q_{ox} = 250 μC cm^{-2} corresponds to Pt oxide containing mainly un-exchanged O_{chem} and Pt_{surf} species, while q_{ox} = 440 μC cm^{-2} corresponds to an entirely place-exchanged surface oxide layer comprising Pt^{2+} and O^{2-} species. Because the values of q_{ox} obtained in the four electrolytes are practically the same (within the experimental uncertainty) and correspond to both an oxide layer prior to and after the place exchange, we can conclude that the anion nature and its concentration have practically no impact on the surface oxide growth on Pt. An analysis of the results presented in Figure 4.6 leads to the conclusion that the amount of electro-dissolved Pt does not depend on the anion nature, but depends on the acid concentration.

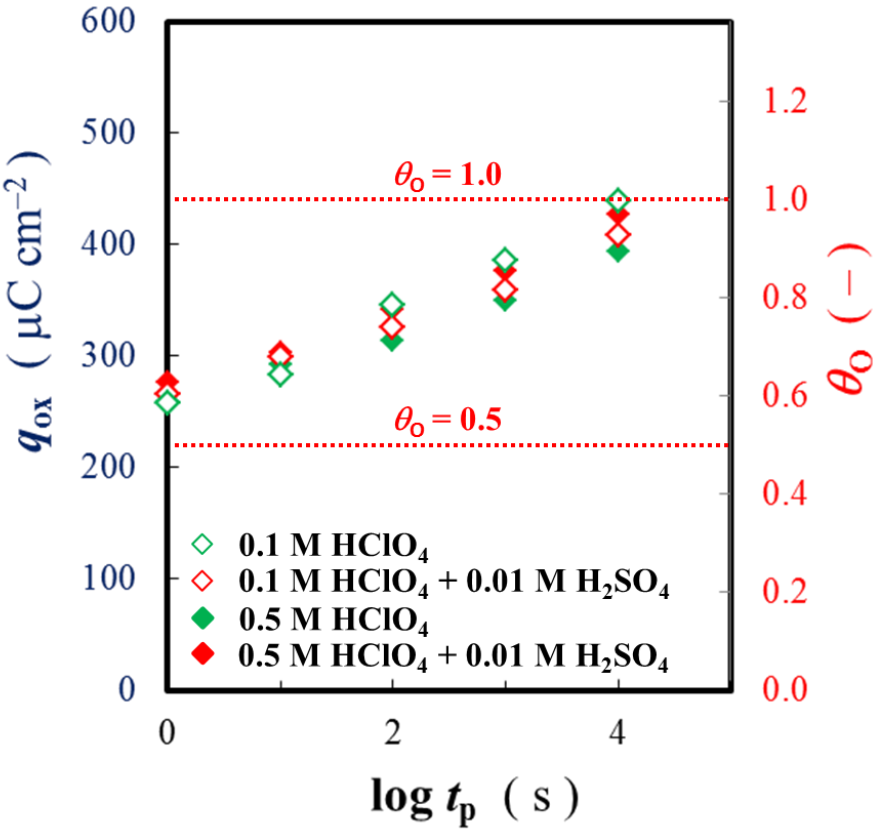

Figure 4.6. q_{ox} versus log t_p plots for E_p = 1.20 V and T = 293 K in 0.1 and 0.5 M $HClO_4$ solutions without and with addition of H_2SO_4 (the concentration of H_2SO_4 after the addition is 0.01 M).

4.3.3 Platinum Electro-dissolution in Aqueous $HClO_4$ Solutions of Different Concentrations

In an effort to understand the influence of pH on Pt electro-dissolution, we analyzed the process in $HClO_4$, thus in an electrolyte containing a non-adsorbing (or weekly adsorbing) anion. Figure 4.7 presents CV profiles for a Pt polycrystalline electrode obtained at s = 50 mV s^{-1} and T

= 293 K in aqueous $HClO_4$ solutions of different concentrations, namely c = 0.01 (blue line), 0.1 (red line), and 0.5 M (green line). As the electrolyte concentration increases, the CV features associated with the electro-adsorption of H_{UPD} shift towards less-positive potential values. On the other hand, the formation of PtO starts at almost the same potential but the PtO reduction peak shifts towards higher potentials.

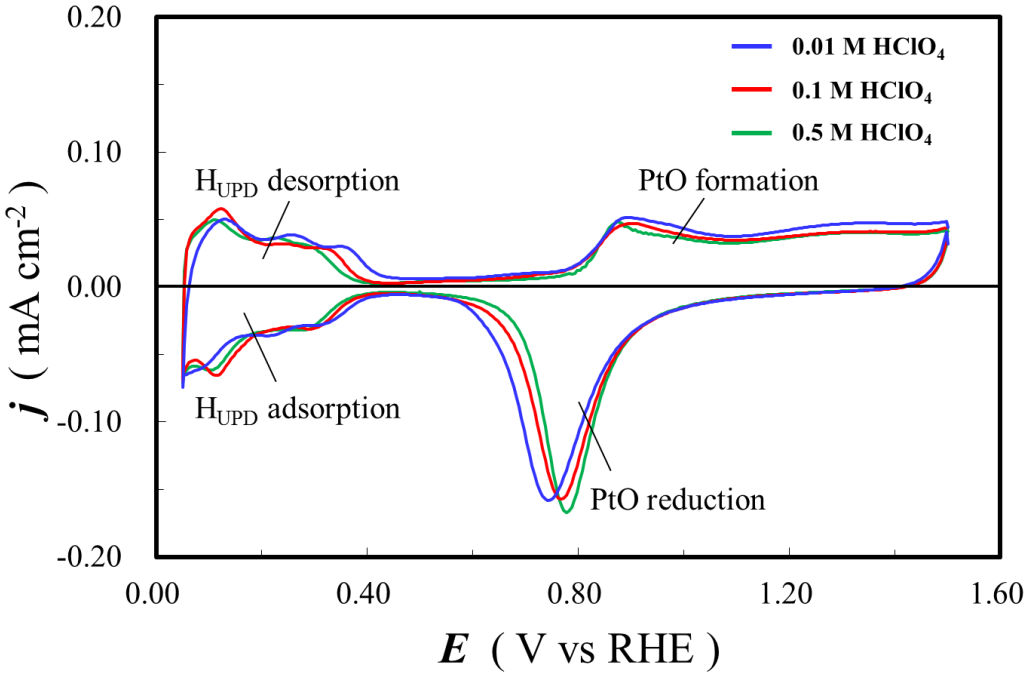

Figure 4.7. Two CV profiles for a Pt polycrystalline electrode obtained at s = 50 mV s^{-1} and T = 293 K in aqueous $HClO_4$ solutions of different concentrations, namely c = 0.01 (blue line), 0.1 (red line), and 0.5 M (green line).

Figure 4.8 presents m_{Pt} versus n plots for potential cycling in the 0.60–1.20 V range at s = 7500 mV s^{-1} and T = 293 K in c = 0.01 M (blue diamonds), 0.1 M (red diamonds), and 0.5 M (green diamonds) aqueous $HClO_4$ solutions. The amount of electro-dissolved Pt is cumulative

and refers to the total amount in the electrolyte solutions. The results demonstrate that the amount of electro-dissolved Pt increases by about two orders of magnitude with a fifty-fold rise in the $HClO_4$ concentration; for n = 5,000 cycles $m_{Pt} = 25 \pm 3$ ng cm^{-2} in 0.01 M $HClO_4$ solution; $m_{Pt} = 941 \pm 98$ ng cm^{-2} in 0.1 M $HClO_4$ solution; and $m_{Pt} = 2620 \pm 390$ ng cm^{-2} in 0.5 M $HClO_4$ solution. These important results clearly demonstrate that the activity of proton has a significantly impact on Pt electro-dissolution.

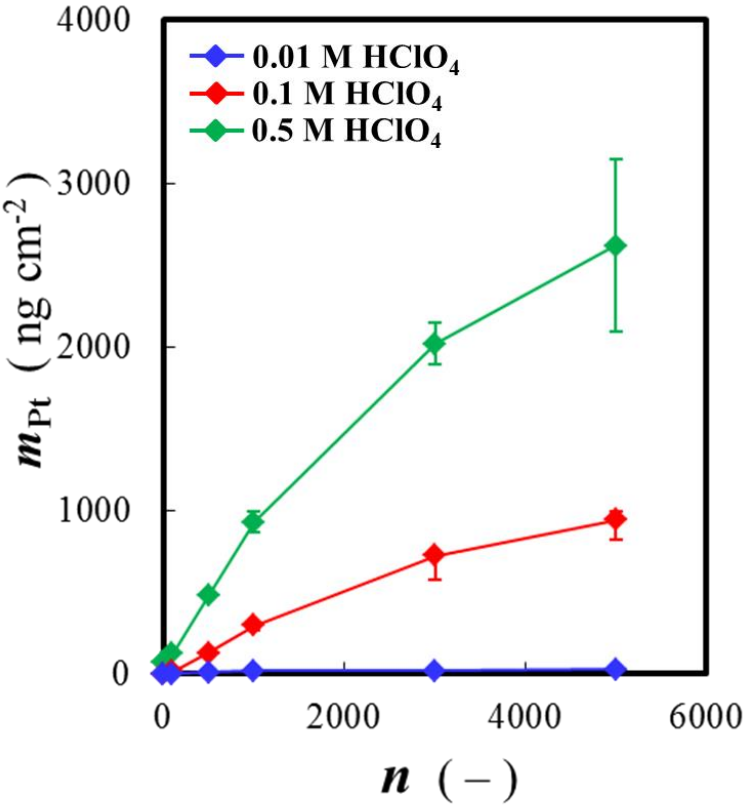

Figure 4.8. m_{Pt} versus n plots for potential cycling in the 0.60–1.20 V range at s = 7500 mV s^{-1} and T = 293 K in c = 0.01 M (blue diamonds), 0.1 M (red diamonds), and 0.5 M (green diamonds) aqueous $HClO_4$ solutions. The error bars indicate maximum and minimum values of these experiments.

We also analyzed the influence of $HClO_4$ concentration on the Pt surface oxide formation in order to determine whether the amount of electro-dissolved Pt correlates with the amount of Pt surface oxide. Figure 4.9 presents q_{ox} versus log t_p plots for Pt oxide growth at E_p = 1.20 V in aqueous $HClO_4$ solutions of three different concentrations, namely c = 0.01 M (blue diamonds), 0.1 M (red diamonds), and 0.5 M (green diamonds). As expected, for a given concentration of $HClO_4$ the values of q_{ox} increase with increasing t_p. In addition, for a given t_p the values of q_{ox} decrease with increasing $HClO_4$ concentration and the difference is in the 10–15% range. The decrease in the amount of PtO as the concentration of $HClO_4$ increases could be related to concurrently occurring chemical dissolution of anodically formed PtO; the process involves protons as reactants. Thus, the longest t_p and the lowest acid concentration generate the thickest Pt oxide layer. Because the anion nature and its concentration do not affect the oxide growth behavior, the difference is due to the change in proton concentration (pH change).

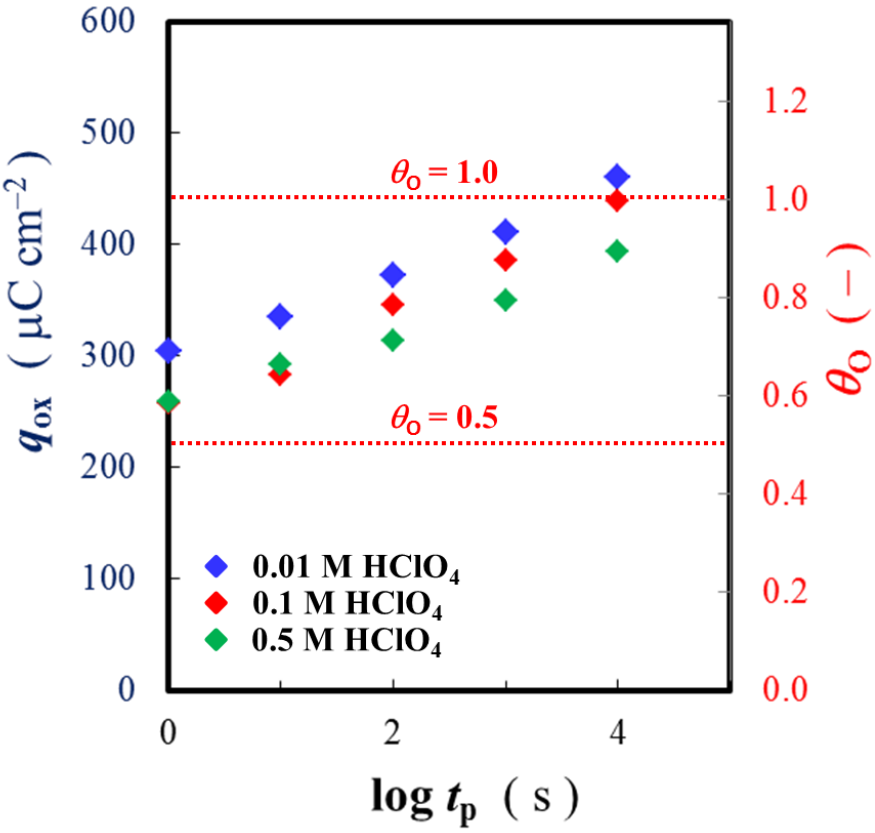

Figure 4.9. q_{ox} versus log t_p plots for Pt oxide growth at E_p = 1.20 V in aqueous $HClO_4$ solutions of three different concentrations, namely c = 0.01 M (blue diamonds), 0.1 M (red diamonds), and 0.5 M (green diamonds).

4.3.4 Mechanism of Platinum Electro-dissolution: Influence of the Electrolyte pH

Elsewhere [13], the following eleven possible mechanisms of electrochemical and chemical Pt dissolution were proposed (the feasibility of these reactions is discussed therein):

Anodic electro-dissolution

$$Pt(s) \longrightarrow Pt^{2+}(aq) + 2\,e^{-} \quad (4.3)$$

$$Pt(s) \longrightarrow Pt^{4+}(aq) + 4\,e^{-} \quad (4.4)$$

$$Pt^{\delta+} - O^{\delta-}{}_{chem} + 2\,H^{+}(aq) \longrightarrow Pt^{4+}(aq) + H_2O(l) + 2\,e^{-} \quad (4.5)$$

$$Pt^{2+} - O^{2-}{}_{quasi\text{-}3D\,lattice} + 2\,H^{+}(aq) \longrightarrow Pt^{4+}(aq) + H_2O(l) + 2\,e^{-} \quad (4.6)$$

Cathodic electro-dissolution

$$Pt^{\delta+} - O^{\delta-}{}_{chem} + 4\,H^{+}(aq) + 2e^{-} \longrightarrow Pt^{2+}(aq) + H_2O(l) + H_2(g) \quad (4.7)$$

$$Pt^{2+} - O^{2-}{}_{quasi\text{-}3D\,lattice} + 4\,H^{+}(aq) + 2\,e^{-} \longrightarrow Pt^{2+}(aq) + H_2O(l) + H_2(g) \quad (4.8)$$

$$Pt^{2+} - O^{2-}{}_{quasi\text{-}3D\,lattice} + 2\,H^{+}(aq) + 2e^{-} \longrightarrow Pt^{0}(aq) + H_2O(l) \quad (4.9)$$

$$PtO_2 + 4\,H^{+}(aq) + 2\,e^{-} \longrightarrow Pt^{2+}(aq) + 2\,H_2O(l) \quad (4.10)$$

Chemical dissolution

$$Pt^{\delta+} - O^{\delta-}{}_{chem} + 2\,H^{+}(aq) \longrightarrow Pt^{2+}(aq) + H_2O(l) \quad (4.11)$$

$$Pt^{2+} - O^{2-}{}_{quasi\text{-}3D\,lattice} + 2\,H^{+}(aq) \longrightarrow Pt^{2+}(aq) + H_2O(l) \quad (4.12)$$

$$PtO_2 + 4\,H^{+}(aq) \longrightarrow Pt^{4+}(aq) + 2\,H_2O(l) \quad (4.13)$$

Equations 4.3–4.4 present direct anodic electro-dissolution of metallic Pt without any participation of H^+; thus, according to these reactions the process does not depend on the electrolyte pH or the amount of Pt surface oxide. However, Equations 4.5–4.13 present electrochemical and chemical Pt dissolution reactions that involve both Pt oxides (PtO or PtO_2) and H^+ as reactants. Thus, according to these reactions the process can be dependent on the

electrolyte pH and the amount of Pt surface oxide. Elsewhere [15], it was demonstrated that the amount of electro-dissolved Pt upon potential cycling is higher than that formed upon potential holding. This behavior could be explained in terms of chemical dissolution of anodically formed Pt surface oxide according to Equations 4.5 and 4.6. Recent ion-exchange chromatography coupled to inductively coupled plasma mass spectrometry (IEC-ICP-MS) measurements reveal that cycling in the 0.60–1.20 V range gives rise to both Pt^{2+}(aq) and Pt^{4+}(aq) species [44], with at least 80% of electro-dissolved Pt being present as Pt^{2+} complexes. These results suggest that the reactions depicted in Equations 4.5–4.6 and 4.11–4.13 could be operational.

As described elsewhere [13], the upper potential limit (E_U) has a significant impact on the amount of electro-dissolved Pt and especially as it passes through the potential range in which the interfacial place-exchange is operational ($1.10 \leq E_U \leq 1.20$ V). Thus, in the case of cycling in the 0.60–1.20 V range with the potential measured versus RHE, 1.20 V on the RHE scale corresponds to 1.20 V on the SHE scale *only* if the activity of proton equals one ($a_{H^+} = 1.00$). However, if the activity of proton is one order of magnitude lower ($a_{H^+} = 0.10$), then the potential of 1.20 V on the RHE scale corresponds to 1.141 V on the SHE scale. Thus, a change in pH from 0 ($a_{H^+} = 1.00$) to 2 ($a_{H^+} = 0.01$) translates to a change of E_U from 1.20 to 1.082 V on the SHE scale. As explained elsewhere [13], a change of E_U from 1.10 V to 1.20 V increases the amount of electro-dissolved Pt by a factor of 3 for n = 1,000, a factor of 4 for n = 2,000, and a factor of 6 for n = 5,000.

Figure 4.10 presents three E (on the SHE scale) versus pH diagrams (Pourbaix diagrams) for Pt in acidic aqueous media at T = 298 K [45]; the graphs A, B, and C refer to the activities of Pt^{2+}(aq) ($a_{Pt^{2+}}$) and Pt^{4+}(aq) ($a_{Pt^{4+}}$) being 1.00, 1.00×10^{-6}, and 1.00×10^{-9}, respectively (the details of these three graphs are discussed in detail below).

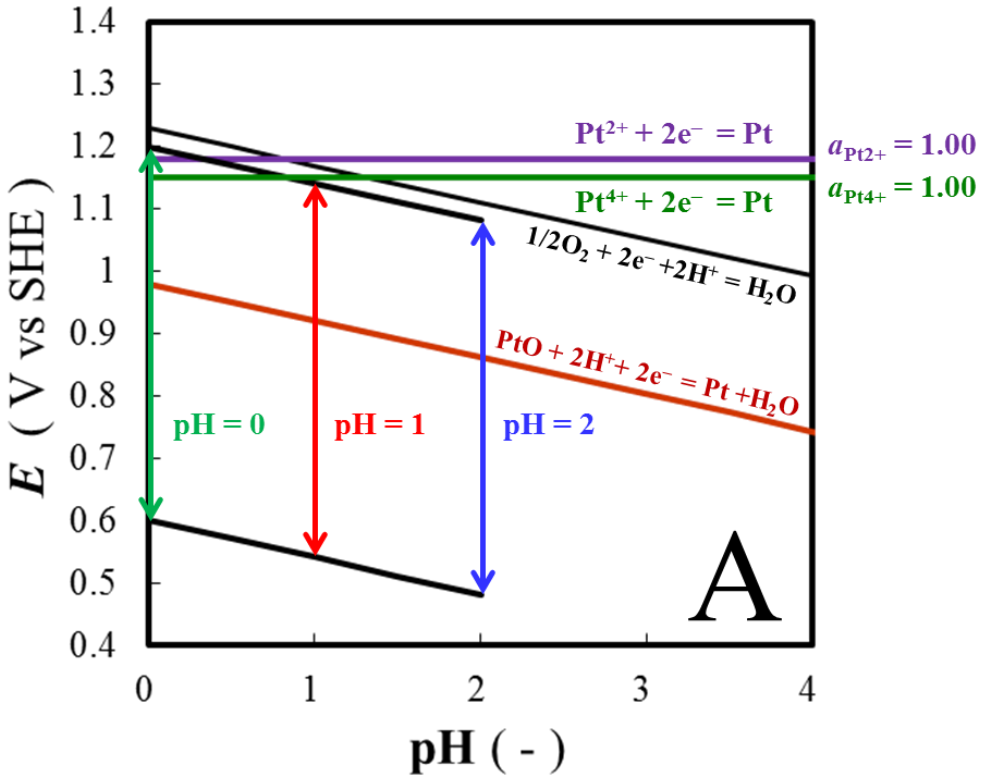
1.4
1.3
1.2
1.1
1
0.9
0.8
0.7
0.6
0.5
0.4
E (V vs SHE)
0
1
2
3
4
pH (-)
Pt2+ + 2e− = Pt
Pt4+ + 2e− = Pt
1/2O2 + 2e− +2H+ = H2O
PtO + 2H+ + 2e− = Pt +H2O
aPt2+ = 1.00
aPt4+ = 1.00
pH = 0
pH = 1
pH = 2
A

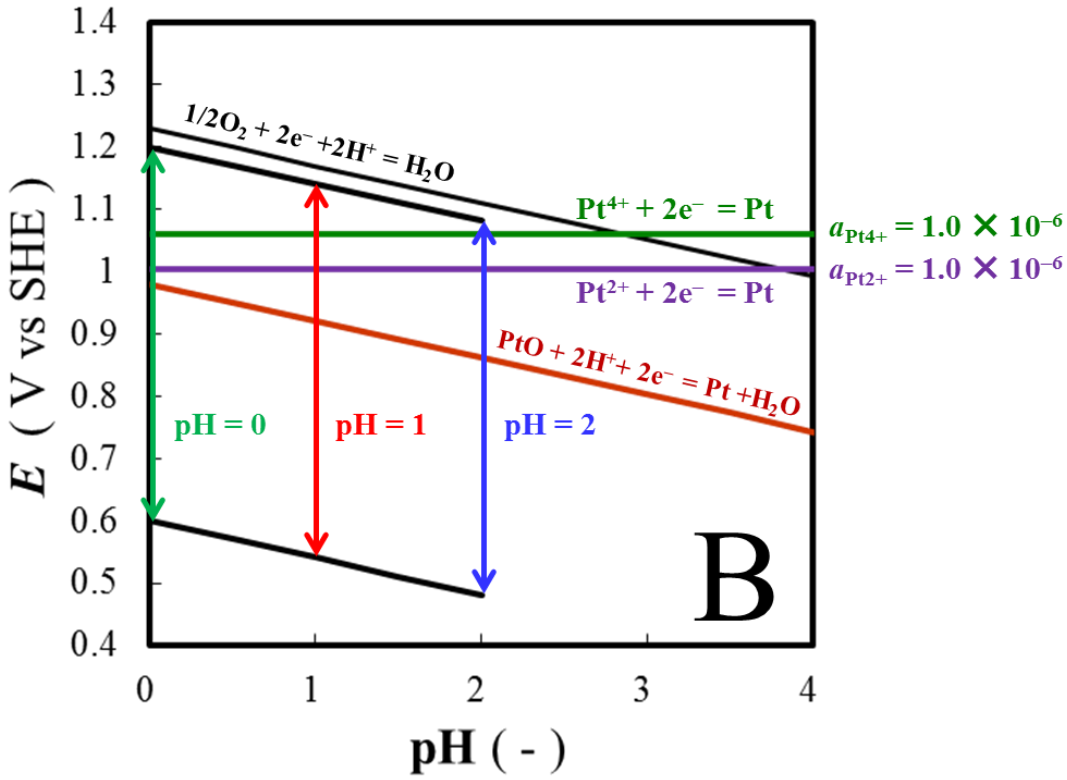
1.4
1.3
1.2
1.1
1
0.9
0.8
0.7
0.6
0.5
0.4
E (V vs SHE)
0
1
2
3
4
pH (-)
1/2O2 + 2e− +2H+ = H2O
Pt4+ + 2e− = Pt
Pt2+ + 2e− = Pt
PtO + 2H+ + 2e− = Pt +H2O
aPt4+ = 1.0 × 10−6
aPt2+ = 1.0 × 10−6
pH = 0
pH = 1
pH = 2
B

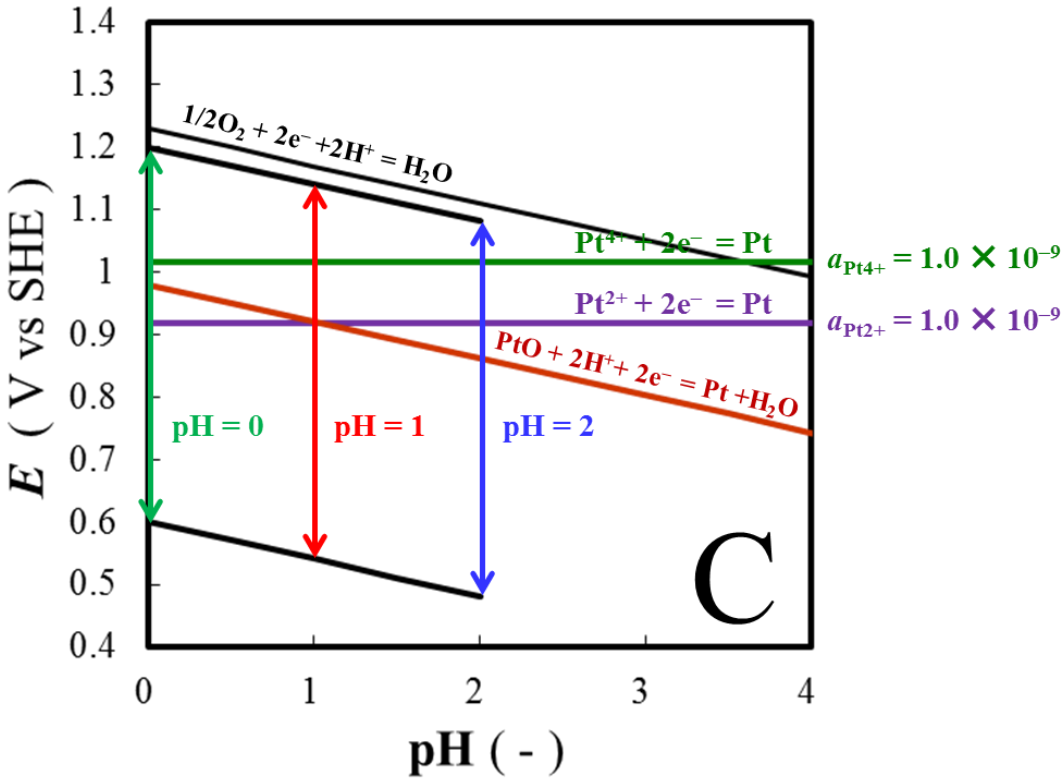

Figure 4.10. Three *E* (on the standard hydrogen electrode scale, SHE) versus pH diagrams (Pourbaix diagrams) for Pt in acidic aqueous media at T = 298 K [45]; the graphs A, B, and C refer to the activities of $Pt^{2+}(aq)$ ($a_{Pt^{2+}}$) and $Pt^{4+}(aq)$ ($a_{Pt^{4+}}$) being 1.00, 1.00×10^{-6}, and 1.00×10^{-9}, respectively

In each graph, the black solid sloping line represents the potential of the $½O_2(g) + 2H^+(aq) + 2e^- = H_2O(l)$ reaction. The solid brown line represents the potential of the following redox reaction as a function of pH:

$$PtO(s) + 2H^+ + 2e^- \rightarrow Pt(s) + H_2O(l) \qquad (4.14)$$

which is given by Equation 4.15:

$$E = E° - \frac{R\,T}{2\,F} \ln \frac{1}{a_{H^+}^2} = 0.980 - 0.0592\ pH \tag{4.15}$$

where $E°$ =0.980 V is the standard potential of this redox process; the value of E depends on the electrolyte pH. Equation 4.14 refers to the formation of bulk PtO, which can undergo subsequent chemical dissolution as discussed below [26]. The solid purple line represents the potential of the following redox reaction:

$$Pt^{2+}(aq) + 2e^- \rightarrow Pt(s) \tag{4.16}$$

which is given by Equation 4.17:

$$E = E° + \frac{R\,T}{2\,F} \ln a_{Pt^{2+}} = 1.188 + 0.0296 \log a_{Pt^{2+}} \tag{4.17}$$

where $E°$ = 1.188 V is the standard potential of this redox process (it refers to $a_{Pt^{2+}} = 1.00$); its value does not depend on the electrolyte pH and only on the activity (concentration) of the $Pt^{2+}(aq)$ cation. The thick solid green line represents the potential of the following redox reaction:

$$Pt^{4+}(aq) + 4e^- \rightarrow Pt(s) \tag{4.18}$$

which is given by Equation 4.19:

$$E = E^\circ + \frac{R\,T}{4\,F}\ln a_{Pt^{4+}} = 1.150 + 0.0148\log a_{Pt^{4+}} \quad (4.19)$$

where E° = 1.150 V is the standard potential of this redox process (it refers to $a_{Pt^{4+}} = 1.00$); its value does not depend on the electrolyte pH and only on the activity (concentration) of the Pt^{4+}(aq) cation. The molal concentrations of Pt^{2+}(aq) and Pt^{4+}(aq) generated through Pt electro-dissolution is typically in the 1.00 × 10^{-9}–10^{-6} mol kg^{-1} range [13]. Assuming that the mean activity coefficients of Pt^{2+} and Pt^{4+} are one ($\gamma_{\pm} = 1.00$; it is a reasonable assumption for a very diluted electrolyte), each ten-fold decrease in the Pt^{2+}(aq) concentration reduces E of the reaction depicted in Equation 4.16 by 0.0296 V and each ten-fold decrease in the Pt^{4+}(aq) concentration reduces E of the reaction depicted in Equation 4.18 by 0.0148 V. Thus, in the case of $a_{Pt^{2+}} = 1.00\times10^{-6}$ E = 1.010 V (graph B) and in the case of $a_{Pt^{2+}} = 1.00\times10^{-9}$ E = 0.922 V (graph C) on the SHE scale. In the case of $a_{Pt^{4+}} = 1.00\times10^{-6}$ E = 1.061 V (graph B) and in the case of $a_{Pt^{4+}} = 1.00\times10^{-9}$ E = 1.017 V on the SHE scale. The vertical green ($a_{H^+} = 1.00$), red ($a_{H^+} = 0.10$), and blue ($a_{H^+} = 0.010$) arrow-ended lines show the potential range of Pt cycling but on the SHE scale. The change in the values of E_L and E_U brought about by the modification of a_{H^+} place them relative to the potential of the three redox couples discussed above (Equations 4.14, 4.16, and 4.18). The graph A in Figure 4.10 refers to unrealistic conditions of $a_{Pt^{2+}} = 1.00$ and $a_{Pt^{4+}} = 1.00$. However, assuming that such concentrations of electro-dissolved Pt^{2+} and Pt^{4+} can be achieved and that $a_{H^+} = 1.00$, potential cycling up to 1.20 V would still generate Pt^{2+} and Pt^{4+} through direct anodic dissolution of metallic Pt. However, a decrease of E_U to 1.10 V would make these processes impossible. The graph B ($a_{Pt^{2+}} = 1.00\times10^{-6}$ and $a_{Pt^{4+}} = 1.00\times10^{-6}$) and

C ($a_{Pt^{2+}} = 1.00 \times 10^{-9}$ and $a_{Pt^{4+}} = 1.00 \times 10^{-9}$) in Figure 4.10 refer to realistic conditions encountered during Pt electro-dissolution experiments. The location of the brown, green, and purple lines representing the potentials of the reactions depicted in Equations 4.14, 4.16, and 4.18 with respect to the vertical, arrow-ended lines referring to the actual potential limits in cycling experiments reveal that all three reactions can actually take place. Thus, these three anodic processes can explain the formation of Pt^{2+}(aq) and Pt^{4+}(aq) through anodic electro-dissolution of Pt(s) or PtO(s). It is important to emphasize that the PtO species in Equation 4.14 is a bulk compound, while PtO in Equations 4.5–9, 4.11, and 4.12 is a surface species. The standard potential of the $PtO_{1ML,surf}/Pt_{surf}$ redox couple (Equation 4.20; $PtO_{1ML,surf}$ refers to one monolayer of PtO residing on Pt surface) has never been defined, although it is well-established and widely accepted that PtO formation on polycrystalline Pt commences at 0.85 V and the reduction of PtO residing on polycrystalline Pt also commences also at 0.85 V [20]. Consequently, we propose that the standard potential of this redox surface couple is $E°$ = 0.85 V.

$$PtO_{1ML,surf} + 2H^+ + 2e^- \rightarrow Pt_{surf} + H_2O(l) \qquad (4.20)$$

Because this process involves two electrons and two protons (as in Equation 4.14), its potential is expected to decrease 0.0592 V with an increase of pH by one. Consequently, potential cycling in the 0.60–1.20 V versus RHE range results in the formation of surface PtO that can undergo subsequent chemical dissolution. A similar analysis should be performed for the reactions shown in Equations 4.5, 4.6, and 4.10–13. However, at the present time the standard potentials of these reactions are unknown. Nevertheless, even without taking into consideration chemical dissolution of PtO, we can explain the formation of Pt^{2+}(aq) and Pt^{4+}(aq) species.

4.4 Conclusions

Electro-dissolution in polycrystalline Pt in aqueous CF_3SO_3H, H_2SO_4, and $HClO_4$ solutions having different concentrations was studied using potential cycling and holding in 0.60–1.20 V range, at scan rate s = 7500 mV s^{-1} and T = 293 K, which mimics the operating conditions of automotive fuel cells. The amount of electro-dissolved Pt was quantified by means of ICP-MS with flow injection of 100 μL aliquots. We report for the first time on the electro-dissolution of Pt in aqueous CF_3SO_3H solutions brought about by the potential cycling and holding. The results reveal that in the case of 0.1 M solutions of CF_3SO_3H, H_2SO_4, and $HClO_4$ the amount of electro-dissolved Pt is practically the same. The amount of dissolved Pt in the 0.5 M aqueous H_2SO_4 solution is larger than in the two other electrolytes. In addition, the results demonstrate that the electrolyte concentration has a major impact on Pt electro-dissolution. The influence of anion nature and pH on Pt electro-dissolution was also studied in $HClO_4$ solution without or with 0.01 M H_2SO_4 addition. The results lead to conclusion that the anion has negligible impact on Pt electrochemical and chemical dissolution but the pH significantly affects the process. An analysis of potential versus pH diagrams (Pourbaix diagrams) for acid solutions of different concentrations demonstrates that dissolved Pt (present as Pt^{2+} and Pt^{4+}) can form through anodic dissolution of metallic Pt, as well as through anodic electrochemical and chemical dissolution of PtO.

4.5 References

(1) A. Ohma, T. Mashio, K. Sato, H. Iden, Y. Ono, K. Sakai, K. Akizuki, S. Takaichi, K. Shinohara, Electrochim. Acta **56**, 10832 (2011)

(2) D. Papageorgopoulos, 2013 Fuel Cells Annual Merit Review (U.S. Department of Energy, Arlington, Virginia, 2013)

(3) R. M. Darling, J.P. Meyers, J. Electrochem. Soc. **150**, A1523 (2003)

(4) R. M. Darling, J.P. Meyers, J. Electrochem. Soc. **152**, A242 (2005)

(5) S. G. Rinaldo, J. Stumper, M. Eikerling, J. Phys. Chem. C **114**, 5773 (2010)

(6) S. G. Rinaldo, W. Lee, J. Stumper, M. Eikerling, Electrochem. Solid-State Lett. **14**, B47 (2011)

(7) R. K. Ahluwalia, S. Arisetty, X. Wang, X. Wang, R. Subbaraman, S. C. Ball, S. DeCrane, D. J. Myers, J. Electrochem. Soc. **160**, F447 (2013)

(8) A. Ohma, K. Shinohara, A. Iiyama, T. Yoshida, A. Daimaru, ECS Trans. **41**, 775 (2011)

(9) R. Shimoi, T. Aoyama, A. Iiyama, SAE Int. J. Engines **2**, 960 (2009)

(10) A. Kongkanand, J.M. Ziegelbauer, J. Phys. Chem. C **116**, 3684 (2012)

(11) Y. Liu, M. Mathias, J. Zhang, Electrochem. Solid-State Lett. 13, B1 (2010)

(12) L. Tang, B. Han, K. Persson, C. Friesen, T. He, K. Sieradzki, G. Ceder, J. Am. Chem. Soc. **132**, 596 (2010)

(13) L. Xing, M.A. Hossain, M. Tian, D. Beauchemin, K.T. Adjemian, G. Jerkiewicz, Electrocatalysis **5**, 96 (2014)

(14) M. Uchimura and S. Kocha, ECS Trans. **11**, 1215 (2007)

(15) X. Wang, R. Kumar, D. J. Myers, Electrochem. Solid-State Lett. **9**, A225 (2006)

(16) M. Matsumoto, T. Miyazaki, H. Imai, J. Phys. Chem. C. **115**, 11163 (2011)

(17) Y. Sugawara, T. Okayasu, A.P. Yadav, A. Nishikata, T. Tooru, J. Electrochem. Soc. **159**, F779 (2012)

(18) A. A. Topalov, I. Katsounaros, M. Auinger, S. Cherevko, J. C. Meier, S. O. Klemm, K. J. J. Mayrhofer, Angew. Chem. Int. Ed. **51**, 12613 (2012)

(19) A. A. Topalov, S. Cherevko, A. R. Zeradjanin, J. C. Meier, I. Katsounaros, K. J. J. Mayrhofer, Chem. Sci. **5**, 631 (2014)

(20) G. Jerkiewicz, G. Vatankhah, J. Lessard, M. Soriaga, Y. S. Park, Electrochim. Acta **49**, 1451 (2004)

(21) B. E. Conway, B. Barnett, H. Angerstein-Kozlowska, B. V. Tilak, J. Chem. Phys. **93**, 8361 (1990)

(22) F. Hiraoka, K. Matsuzawa, S. Mitsushima, Electrocatalysis **4**, 16 (2012)

(23) S. Mitsushima, S. Kawahara, K. Ota, N. Kamiya, J. Electrochem. Soc. **154**, B153 (2007)

(24) S. Cherevko, A. A. Topalov, A. R. Zeradjanin, G.P. Keeley, K. J. J. Mayrhofer, Electrocatalysis **5**, 235 (2014)

(25) A. A. Topalov, A. R. Zeradjanin, S. Cherevko, K. J. J. Mayrhofer, Electrochem. Commun. **40**, 49 (2013)

(26) S. Mitsushima, Y. Koizumi, S. Uzuka, K. Ota, Electrochim. Acta **54**, 455 (2008)

(27) A. P. Yadav, T. Okayasu, Y. Sugawara, A. Nishikata, T. Tsuru, J. Electrochem. Soc. **159**, C190 (2012)

(28) V. Komanicky, K. C. Chang, A. Menzel, N. M. Markovic, H. You, X. Wang, D. Myers, J. Electrochem. Soc. **153**, B446 (2006)

(29) R. Subbaraman, D. Strmcnik, V. Stamenkovic, N. M. Markovic, J. Phys. Chem. C **114**, 8414 (2010)

(30) H. Hanawa, K. Kunimatsu, M. Watanabe, H. Uchida, J. Phys. Chem. C **116**, 21401 (2012)

(31) K. Kodama, R. Jinnnouchi, T. Suzuki, H. Murata, T. Hatanaka, Y. Morimoto, Electrochem. Com. **36**, 26 (2013)

(32) T. Masuda, F. Sonsudin, P. R. Singh, H. Naohara, K. Uosaki, J. Phys. Chem. C **117**, 15704 (2013)

(33) A. Ohma, K. Fushinobu, K. Okazaki, Electrochim. Acta **55**, 8829 (2010)

(34) G. Attard, A. Brew, K. Hunter, J. Sharman, E. Wright, Phys. Chem. Chem. Phys. **16**, 13689 (2014)

(35) A. Ohma, T. Ichiya, K. Fushinobu, K. Okazaki, Surf. Sci. **604**, 965 (2010)

(36) M. Teliska, V. Murthi, S. Mukerjee, D. E. Ramaker, J. Phys. Chem. C **111**, 9267 (2007)

(37) A. Berna, J. M. Feliu, L. Gancs, S. Mukerjee, Electrochem. Commun. **10**, 1695 (2008)

(38) S. S. K-L. Hsueh, H. H. Chang, D-T. Chin, Electrochim. Acta **30**, 1137 (1985)

(39) K. Kodama, A. Shinohara, N. Hasegawa, K. Shinozaki, R. Jinnouchi, T. Suzuki, T. Hatanaka, Y. Morimoto, J. Electrochem. Soc. **161**, F649 (2014)

(40) D. Chen, Q. Tao, L.W. Liao, S. X. Liu, Y. X. Chen, S. Ye, Electrocatalysis **2**, 207 (2011)

(41) B. E. Conway, H. Angerstein-Kozlowska, W. A. Sharp, E. E. Criddle, Anal. Chem. **45**, 1331 (1973)

(42) M. Alsabet, M. Grden, G. Jerkiewicz, J. Electroanal. Chem. **589**, 120 (2006)

(43) A. Zolfaghari, M. Chayer, G. Jerkiewicz, J. Electrochem. Soc. **144**, 3034 (1997)

(44) L. Xing, G. Jerkiewicz, D. Beauchemin, Anal. Chim. Acta, **785**, 16 (2013).

(45) M. J. N. Pourbaix, J. Muylder, N. Zoubov, Platin. Met. Rev. **3**, 47 (1959)

Chapter 5

Conclusions

During the course of this thesis work, the electrochemical behavior of polycrystalline Pt electrodes in aqueous trifluoromethanesulfonic acid (CF_3SO_3H) solutions was studied. In the field of development of fuel cell electric vehicles (FCEVs), Pt nanoparticles (Pt-NPs) and Nafion® are the key and most expensive components of polymer electrolyte membrane fuel cells (PEMFCs). Their stability determines the power output and lifetime of PEMFCs. Trifluoromethanesulfonic acid is the smallest fluorinated sulfonic acid mimicking the ionomer of Nafion®, it is an ideal compound to examine the anion-platinum interactions, which can impact the degradation and performance of Pt-NPs through electro-oxidation and electro-dissolution processes. Very little information on electrochemical behavior of Pt polycrystalline electrode in CF_3SO_3H was previously available in the literature (fewer than ten papers). Thus, this PhD research project represents an original contribution and the volume of the results presented in the thesis demonstrates that experimental work with CF_3SO_3H can be effectively carried out although it was thought to be troublesome because the commercially available CF_3SO_3H is not as pure as commercial H_2SO_4 or $HClO_4$.

Platinum electro-oxidation in 0.1 M aqueous CF_3SO_3H solution was studied at various polarization potentials (E_p), polarization times (t_p), and temperatures (T). For a comparative analysis, similar experiments were performed in aqueous H_2SO_4 and $HClO_4$ solution. The critical thicknesses (X_1), which determines the applicability of oxide growth theories was determined and related to the actual oxide thickness (d_{ox}). This is accomplished for the first time for the Pt oxide system and the knowledge of X_1 (or d_{ox}) facilitates a theoretical analysis of the process. Because $X_1 > d_{ox}$ for the entire range of E_p, t_p, and T values, the formation of Pt surface oxide follows the

interfacial place-exchange (Conway et al. *J. Chem. Phys.* **93**, 8361 (1990).) or the metal cation escape mechanism (Mott and Cabrera, *Rep. Prog. Phys.* **12**, 163 (1948).). The mechanism of Pt electro-oxidation was revised and expanded by taking into account possible interactions of cations, anions and water molecules with the platinum surface. The kinetic equation describing the rate of interfacial place exchange originating from repulsive interactions between $Pt^{\delta+}$–$O^{\delta-}$ surface dipoles was modified and expanded by taking into time-dependent variation of the surface potential. The application of the interfacial place exchange and cation escape mechanisms results in the determination of the $Pt^{\delta+}$–$O^{\delta-}$ surface dipole moment (μ_{PtO}), as well as the potential drop (V_{ox}) and electric field (E_{ox}) within the oxide. Because comparative experiments were performed in aqueous CF_3SO_3H, H_2SO_4 and $HClO_4$ solution, it was possible to analyze the impact of the anion on the Pt surface oxide growth behaviour. It is found that the platinum-anion interactions affect the oxidation kinetics indirectly by influencing the electric field within the double layer and the surface oxide. At present, this effect is identified but there is no theoretical approach that would allow its quantification.

The electro-adsorption of under-potential deposited hydrogen (H_{UPD}) on polycrystalline Pt electrodes in CF_3SO_3H was investigated using cyclic voltammetry (CV) in over a broad *T* range with the objective of determining thermodynamic state functions governing the process, namely standard Gibbs energy ($\Delta_{ec-ads}G°(H_{UPD})$), entropy ($\Delta_{ec-ads}S°(H_{UPD})$), and enthalpy ($\Delta_{ec-ads}H°(H_{UPD})$). The CV profiles obtained in CF_3SO_3H revealed the usual features associated with the electro-adsorption of H_{UPD} as well as with the surface oxide formation and reduction. They indicated that the system (electrode, electrolyte, cell) was maintained impurity-free for extended periods of time. This was not a trivial matter because temperature-dependent studies involved very long experiments, which due to their longevity gradually might introduce contamination into the system. The application of the general electrochemical adsorption

isotherm allowed us to analyze for the first time the thermodynamics of UPD H and to determine that $\Delta_{ec-ads}G°(H_{UPD})$ varies from –13 to –27 kJ mol^{-1}; $\Delta S^{\circ}_{ads}(H_{UPD})$ varies from –59 to +20 kJ mol^{-1} K^{-1}; and $\Delta H^{\circ}_{ads}(H_{UPD})$ varies from –8 to –43 kJ mol^{-1}. We determined the Pt–H_{UPD} surface bond energy ($E_{Pt-H_{UPD}}$) adopted values from 225 to 261 kJ mol^{-1}. The lateral interactions between the H_{UPD} adatoms were found to be repulsive in nature and the energy of lateral interactions ($\omega(H_{UPD})$) was determined to vary from +14 to +22 kJ mol^{-1}. The process of H_{UPD} electro-adsorption was found to follow a Temkin electro-adsorption isotherm and the energy of lateral interactions was found to be temperature-dependent. A comparison of the values of $\Delta_{ec-ads}G°(H_{UPD})$, $\Delta_{ec-ads}S°(H_{UPD})$, $\Delta_{ec-ads}H°(H_{UPD})$, $\omega(H_{UPD})$ and $E_{Pt-H_{UPD}}$ obtained in CF_3SO_3H with those obtained in H_2SO_4 and $HClO_4$ reveals that they are very similar indicating that the anion constituting the electrolyte has little or no impact on the process.

Electrochemical and chemical dissolution in polycrystalline Pt in aqueous CF_3SO_3H, H_2SO_4, and $HClO_4$ solutions of different concentrations was studied using fast potential cycling and holding. The employment of aqueous H_2SO_4 and $HClO_4$ solutions facilitated a comparative analysis of the interfacial electrochemical behavior in CF_3SO_3H with the objective of identifying any anion-related effects. The amount of electro-dissolved Pt is quantified by means of inductively coupled plasma mass spectrometry (ICP-MS). We present for the first time analysis of Pt degradation in aqueous CF_3SO_3H solutions. In the case of 0.1 M CF_3SO_3H, H_2SO_4, and $HClO_4$ solutions, the amount of dissolved Pt is the same but in the case of 0.5 M solutions the amount of dissolved Pt in CF_3SO_3H and $HClO_4$ is the same but significantly lower than that in H_2SO_4. The influence of anion nature and electrolyte pH on the electrochemical and chemical Pt dissolution was studied in $HClO_4$ without or with 0.01 M H_2SO_4 addition. It is concluded that the anion nature has no or negligible impact on the process. On the other hand, an increase in the

electrolyte pH significantly enhances Pt dissolution. In order to better understand the dissolution of polycrystalline Pt brought about by potential cycling and holding, potential versus pH diagrams (Pourbaix diagrams) for the 0.1 and 0.5 M acid solutions was analyzed. In addition, a review of standard potentials of redox reactions involving Pt^0, Pt^{2+}, Pt^{4+} and PtO was done with the objective of identifying electrochemical and chemical processes that could degrade Pt. It was concluded that the dissolved Pt (present as Pt^{2+} and Pt^{4+}) can form through anodic dissolution of metallic Pt, as well as through anodic electrochemical and chemical dissolution of PtO.

The science and technology of Pt electrocatalyst is critical for further fuel cell development and their application in FCEVs. One of the key issues of the PEMFC technology is the influence of platinum-anion interactions on the electrocatalystic behavior and long-term performance of Pt electrodes. Understanding of these interactions and associated phenomena is vital for the reduction of Pt usage (loading) in fuel cells. We present a few examples which demonstrate how platinum-anion interactions taking place in a Nafion mimicking electrolytes can affect three most typical electrochemical reactions: H electro-adsorption, surface oxide formation, and dissolution. The electrochemical experiments in CF_3SO_3H solutions show similar electrochemical behavior to that in conventional acidic media (H_2SO_4 or $HClO_4$). Under some potential conditions, the anion nature influences Pt oxide formation, but does not affect UPD H or Pt electrochemical or chemical dissolution. The intriguing results for Pt electro-oxidation obtained in three different electrolytes will drive new experimental and theoretical research efforts, because the formation of PtO can affect not only the degradation of Pt electrocatalysts but also long-term performance of PEMFCs. We believe that CF_3SO_3H will be employed more frequently in the field of fuel cells and water electrolysis to simulate electrode-anion interactions in key electrochemical reactions (e.g. oxygen reduction reaction, oxygen evolution reaction, hydrogen oxidation reaction, hydrogen evolution reaction, and electrode electrochemical and

chemical dissolution). New knowledge gained through such research will be beneficial to researchers who are currently working on developing fuel cells and water electrolysers.

Chapter 6

Future Work

The volume of the work reported in the thesis, identifies and quantifies interfacial electrochemical phenomena of vital importance to fuel cells, and generates new questions that could result in new research projects. Because the research deals with a model system comprising bulk polycrystalline Pt and aqueous CF_3SO_3H solutions, similar experimental work should be carried out using Pt nanoparticles (Pt-NPs) of controlled geometry (e.g. spherical, cubic, octahedral, cuboctahedral) and size (e.g. in the 5–30 nm range). Research on the electro-oxidation and electrochemical and chemical dissolution of Pt-NPs would be of particular importance for the PEMFC science and technology. Similar research employing core-shell Pt-containing nanoparticles (e.g. Pt-Ni, Pt-Co) should also be conducted. Following this research, experimental work employing more complex conditions should be carried out. In particular, one would like to study the electro-oxidation and electrochemical and chemical dissolution of carbon-supported Pt-NPs with the objective of identifying and qualifying support-specific phenomena. The experimental electrochemical research should be conducted in conjunction with theoretical and modelling research. Because this is outside the scope of our expertise, such a research project could be conducted by a research group that specializes in modelling of fuel-cell phenomena. Because the amount of dissolved Pt has to be quantified and the nature of dissolved Pt has to be identified (nature of the complex compound and the ligand type), new analytical and inorganic chemistry approaches should be developed. In particular, one would like to employ a robust, high-throughput and inexpensive analytical technique that allows many samples to be examined. As regards the nature of dissolved Pt, although it is established that Pt is in the 2+ and 4+ oxidation states, the nature of the complex compounds remains unknown. Consequently,

inorganic chemistry research is needed and would greatly benefit the PEMFC science and technology.